12-2008

Laser Processing of Refractory Metal - Refractory Carbide Alloys

Deepak Rajput
University of Tennessee - Knoxville

To the Graduate Council:

I am submitting herewith a thesis written by Deepak Rajput entitled "Laser Processing of Refractory Metal - Refractory Carbide Alloys." I have examined the final electronic copy of this thesis for form and content and recommend that it be accepted in partial fulfillment of the requirements for the degree of Master of Science, with a major in Materials Science and Engineering.

William H. Hofmeister, Major Professor

We have read this thesis and recommend its acceptance:

Jacqueline Anne Johnson, Lloyd M. Davis, William H. Hofmeister

Accepted for the Council:
Carolyn R. Hodges

Vice Provost and Dean of the Graduate School

(Original signatures are on file with official student records.)

To the Graduate Council:

I am submitting herewith a thesis written by Deepak Rajput entitled "Laser Processing of Refractory Metal - Refractory Carbide Alloys." I have examined the final electronic copy of this thesis for form and content and recommend that it be accepted in partial fulfillment of the requirements for the degree of Master of Science, with a major in Materials Science & Engineering.

William H. Hofmeister, Major Professor

_____

We have read this thesis and
recommend its acceptance:

Dr. Jacqueline Anne Johnson

_____

Dr. Lloyd M. Davis

_____

Dr. William H. Hofmeister

_____

Accepted for the Council:

Carolyn R. Hodges

_____

Vice Provost and Dean of the Graduate School

(Original signatures are on file with official student records.)

LASER PROCESSING OF REFRACTORY METAL - REFRACTORY CARBIDE ALLOYS

A Thesis

Presented for the

Master of Science

Degree

The University of Tennessee, Knoxville

Deepak Rajput

December 2008

This thesis is dedicated to my parents

PREFACE

This thesis is based upon studies conducted during September 2006 to August 2008 at the Center for Laser Applications, Department of Materials Science and Engineering, The University of Tennessee Space Institute, Tullahoma, Tennessee.

I would like to express my sincere gratitude towards my major adviser Dr. William H. Hofmeister for his guidance and support in successfully carrying out this work. I earnestly thank Drs. Jacqueline Anne Johnson and Lloyd M. Davis who served on my master's thesis committee. I owe a deep sense of gratefulness to Dr. Lino Costa and Ms. Kathleen Lansford, who deserve a special recognition for their cooperation and unstinting support extended throughout my master's research at UTSI.

I sincerely acknowledge Mr. Alexander Terekhov and Mr. Doug Warnberg for their assistance in my experiments. I extend my gratitude towards Mr. Peter Sherrouse and Mr. Gary Payne for their help in making certain experimental set-ups. I am very thankful to Ms. Emily S. Moore and Ms. Brenda Brooks for their help in searching some archaic articles necessary for my research. I am highly thankful to the administrative staff of the Center for Laser Applications, Ms. Carole Thomas and Ms. Penny Oliver for their assistance with the supplies and other administrative works. I would also like to place my sincere gratitude towards Dr. Christian Parriger for his helpful suggestions and encouragement, and summer interns Mr. William Yue, Ms. Marybeth Parker and Ms. Larissa Wenren for their assistance in conducting experiments and laboratory tests.

I express my heartfelt thanks to my friends, Dr. Xiaoxuan Li, Dr. Yelena White, Dr. Abraham Meganathan, Matthew Parrish, Jaya Prakash Nanna, Ajay Katta, Subhashini Chitta, and Sangheum Kim for their valuable suggestions, support and encouragement.

Tullahoma, Tennessee Deepak Rajput

December 2008

ABSTRACT

The objective of the present study was to laser process a refractory metal – refractory carbide alloy based on W-Ti-C ternary system for severe service applications. The key concept was to cast a eutectic alloy of tungsten and titanium carbide/carbonitride straight from the melt through laser materials processing route. In the present study, a W-Ti-C ternary alloy has been laser processed into three-dimensional objects and surface protective coatings. Two novel fabrication systems were designed to build three-dimensional objects, namely tower nozzle solid freeform fabrication system and axis-symmetric laser powder deposition system. W-Ti-C alloy based protective coatings were deposited on graphite substrates, through laser melting of pre-placed powder mixture, to widen the use of carbon structural elements for high temperature applications. A method for depositing W-Ti-C alloy on steel using multi-intermediate layers strategy is discussed and the preliminary results are presented in this study.

TABLE OF CONTENTS

LIST OF TABLES

LIST OF FIGURES

LIST OF ABBREVIATIONS

SEM	Scanning Electron Microscope
EDS	Energy Dispersive Spectrometer
XRD	X-ray Diffraction
SFF	Solid Freeform Fabrication
ID	Internal Diameter
LISI	Laser Induced Surface Improvement
LENS	Laser Enhanced Net Shaping
Nd:YAG	Neodinium: Ytterium Aluminum Garnet
LP:YAG	Lamp Pumped: Ytterium Aluminum Garnet
LPD	Laser Powder Deposition
SLS	Selective Laser Sintering
EBM	Electron Beam Melting
3DP	3 Dimensional Printing
SCFH	Standard Cubic Feet per Hour
APS	Advanced Powder Solutions
VHN	Vickers Hardness Number
HAZ	Heat Affected Zone

CHAPTER 1

INTRODUCTION

Materials selection for severe service applications is always a challenge to the scientists especially in the aerospace industry, power plants, chemical plants, oil refineries and tools industry. It is due to the fact that mechanical strength of metals and alloys decreases with increasing temperature and the properties become much more time dependent. The major effects of high temperature on metals or alloys are reduction in strength, oxidation and intergranular penetration, recrystallisation and grain growth, grain boundary sliding, overaging of age-hardened alloys, dislocation climb and diffusion. With the advent of gas turbines in the 1940's the operating temperature exceeds 1000^{o}C and that requires materials with improved high temperature strength and oxidation resistance. To cope with these requirements, the materials scientists worked to design new materials for the applications posing severe service conditions though applications like rocket engines still present greater problems. In addition, applications like gas turbines or jet engines generally expose components to loading that requires resistance to creep, fatigue, corrosion or super-imposed creep-fatigue interactions and creep-fatigue-corrosion interactions [1]. Thus, the criticality of materials selection is related to the strength of material and its resistance to mechanical failure and chemical reactions at high temperatures.

Two important classes of materials that are used in high temperature applications are superalloys [2] and cermets [3]. Based on nickel, cobalt or nickel-iron, a superalloy typically has an austenitic face-centered cubic crystal structure that exhibits excellent mechanical strength and creep strength at high temperatures. Whereas, a cermet is a composite material composed of ceramic and metallic materials, and has the properties of both [4]. The metal part in a cermet works as a binder for an oxide, boride, carbide or alumina. Depending on the composition of the material, cermets can also be metal matrix composites, but cermets are normally less than 20% metal by volume e.g., WC-Co [5]. Cermets, though designed and best suited for cutting tool applications, are oftentimes preferred for severe service applications where hardness, wear and erosion resistance, and strength are required. They are generally formed from refractory carbide materials by press and sinter techniques into ceramic metal composites, commonly known as hard metals or as cemented or sintered carbides, where the metal phase binder acts as a sintering aid during fabrication and provides toughness to the resulting cermet [6]. But the strength and hardness of a cermet, at elevated temperatures, depends on the stability of metal phase in the composite. At high temperatures, the metal phase of the cermet starts softening, which affects the mechanical properties of the cermet and limits the operational range [6].

The development of castable refractory metal – refractory carbide and refractory metal – refractory – carbonitride alloys improved the high temperature mechanical properties of cermets [6, 7]. These alloys are made by casting a eutectic alloy of a refractory metal and a refractory carbide or carbonitride straight from the melt. One such

example is the W-Ti-C ternary system, investigated in detail by Erwin Rudy [7]. The W-Ti-C eutectic point is at 2700°C with composition 58 W – 20 Ti – 22 C atomic percent. After casting the W-Ti-C eutectic system from its melt, the liquid solidifies to a (W,Ti) metal phase and a (Ti,W)C monocarbide phase. The results showed that the cast eutectic (W,Ti) + (Ti,W)C alloy has excellent hot hardness, and it outperforms WC cemented carbide counterparts at temperatures above 500°C [7]. Thus, the W-Ti-C based eutectic alloy is expected to have excellent high temperature erosion resistance and better high temperature mechanical properties than the conventional cermets.

The castable refractory metal – refractory carbide materials (referred to as ***cast carbides*** from this point onwards) were initially developed for metal removal tool applications, but they are also potential candidate materials for applications requiring high temperature erosion resistance e.g., rocket nozzles [7, 8]. Cast carbides can be used either as a "three-dimensional component" or a "coating" depending upon the application. The two major problems associated with the fabrication of cast carbides are casting and forming [8]. The high melting temperature (approx. 2700^{o}C for W-Ti-C eutectic point) causes problems in melt processing and casting, whereas their exceptional hardness limits the machinability and formability. In addition, the casting must be done from the melt at a very high quench rate in order to achieve a very fine distribution of carbide phase and capture the benefits of strength, wear resistance and toughness [8, 9].

The problems associated with forming can be solved by using solid freeform fabrication (SFF) techniques e.g., laser enhanced net shaping (LENS^{TM}), selective laser

sintering, three-dimensional printing. The high quench rates can be achieved by using rapid solidification processing techniques e.g., laser melting, electron beam melting, thermal spraying. Laser powder deposition (LPD) combines the benefits of both the solid freeform fabrication and rapid solidification [10]. Thus, laser powder deposition is one of the effective ways for producing near net shape components. On the other hand, a cast carbide coating can be produced by laser surface alloying technique like laser induced surface improvement (LISI) [9].

In the present study, cast carbide based on W-Ti-C ternary system was made by laser processing into three-dimensional near net shape components and surface coatings. The laser processed cast carbide is termed as ***cermelt*** from this point onwards. The term cermelt was coined at the Center for Laser Applications, The University of Tennessee Space Institute to distinguish the laser processed cast eutectic cermets from conventional cast carbides and cermets.

The objective of the present study is to develop cermelts in the form of three-dimensional components and surface coatings for severe service applications. The W-Ti-C ternary system based cermelt was built into three-dimensional components using an internally developed tower nozzle powder delivery system and axis-symmetric solid freeform fabrication technique. And, protective coatings based on W-Ti-C ternary system were deposited on graphite using laser induced surface improvement process to widen the use of carbon based structural elements for high temperature applications. A method of

depositing high melting temperature W-Ti-C cermelt coating on steel is also discussed in detail.

CHAPTER 2

BACKGROUND

2.1 Refractory Carbide Materials

Refractory carbide materials are oftentimes selected for extreme environment applications where hardness, wear resistance and strength at high temperatures are required. Refractory carbide materials are usually formed by press and sinter techniques into ceramic metal composites (cermets), commonly known as hard metals or as cemented or sintered carbides, where the metal phase binder serves as a sintering aid during fabrication and provides toughness to the resulting cermet [6, 8]. For cutting tool applications, commercial sintered carbide materials usually consist of tungsten or titanium carbide particles dispersed in a matrix of an iron group metal, usually cobalt or nickel. For extreme temperature environments where the loss of strength of iron group metal based binders becomes significant, a refractory metal phase binder can be used instead.

Refractory carbide materials are processed into sintered carbide type wear-resistant surface coatings and three dimensional sintered carbide components using various thermal spraying, laser materials processing and 3D printing techniques [11-13].

2.2 Castable Refractory Metal - Refractory Carbide Alloys

Refractory carbide materials with superior hot strength and improved resistance to thermal and mechanical shock were achieved with the development of castable refractory metal - refractory carbide and refractory metal – refractory carbonitride alloys. Here, the essential idea is to cast, from the melt, a eutectic alloy of a refractory metal phase and its monocarbide or carbonitride. For example, the W-Ti-C ternary system, investigated in detail by Erwin Rudy, has a eutectic point at 2700 ºC and composition (58 W - 20 Ti - 22 C atomic %), shown in Figure 2.2(a), where a tungsten rich liquid solidifies to a refractory (W,Ti) metal phase and the (Ti,W)C monocarbide phase.

The cast eutectic (W,Ti) + (Ti,W)C alloy is known to have excellent hot hardness, outperforming WC cemented carbide counterparts at temperatures above 500 ºC, shown in Figure 2.2(b), and is therefore expected to have exceptional high temperature erosion resistance. Although developed initially for metal removal tool applications, these refractory metal – refractory carbide materials, referred as “cast carbides”, are also suitable candidate materials for rocket nozzle applications, where high temperature erosion is a major concern. However, the machinability and formability of these materials into shapes remain problematic. Their exceptional hardness severely limit the use of machining techniques for shaping purposes, and the high melting temperatures involved in making refractory cast carbide materials raise considerable melt processing and casting difficulties. Moreover, to create a very fine carbide phase distribution and achieve the full benefits of alloy strength, wear resistance and toughness, the material must be rapidly solidified from the melt [8, 9].

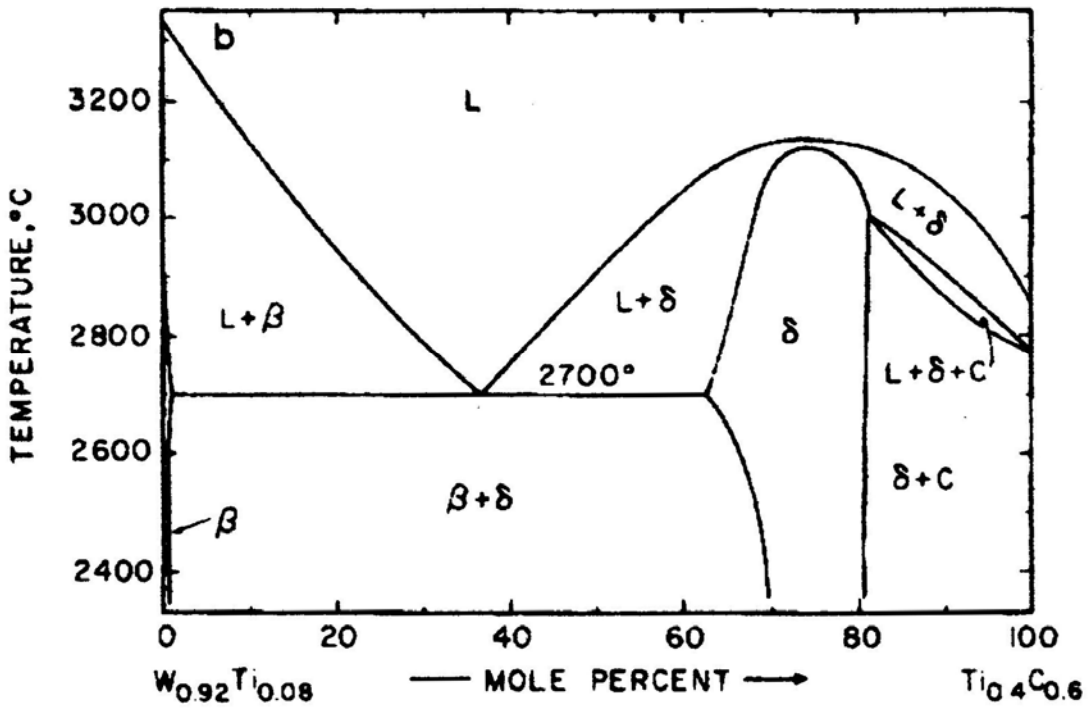

Figure 2.2(a). Isopleth at the pseudobinary section metal + monocarbide. β – (W,Ti) metal phase; δ – (Ti,W)C monocarbide phase. The W_2C phase does not form within this composition range. Source: [7].

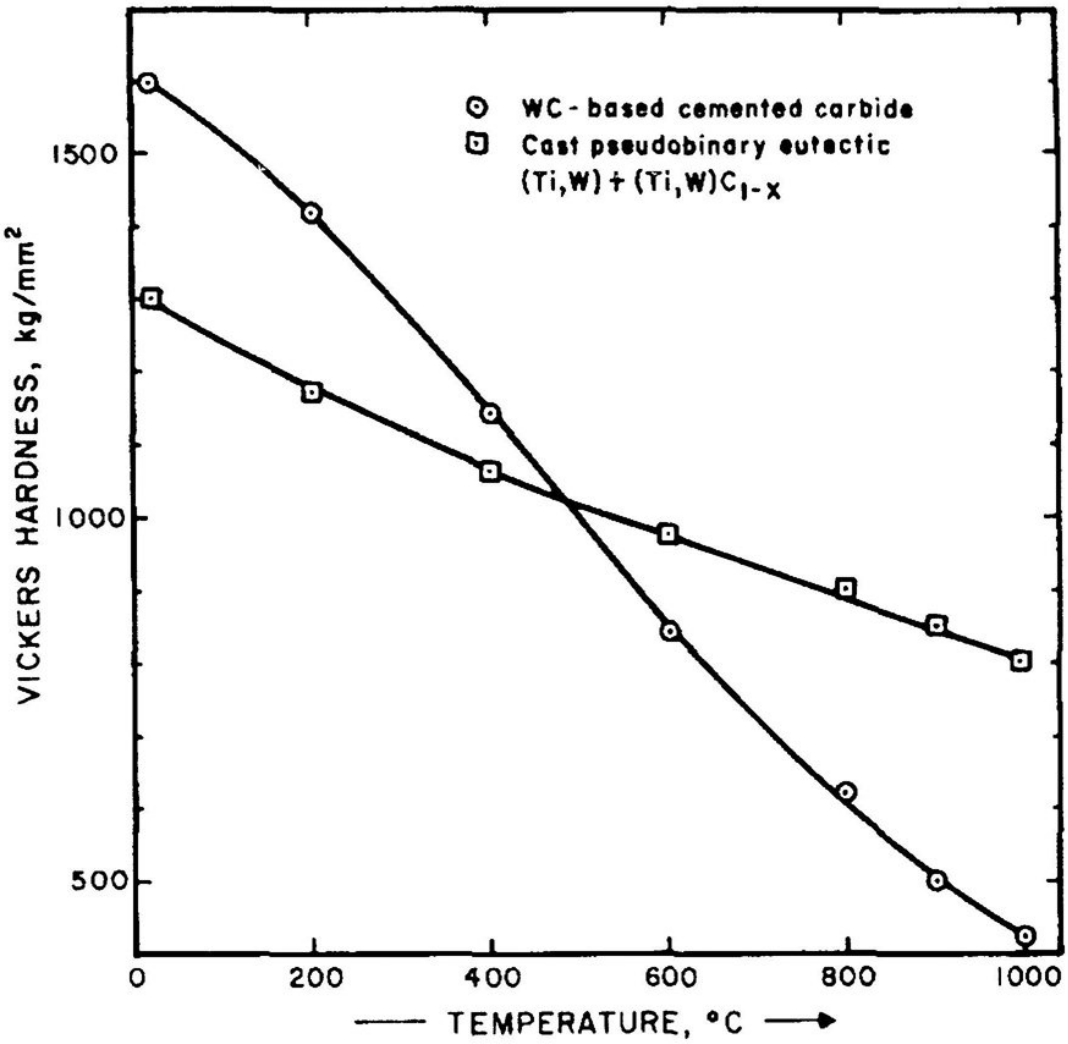

Figure 2.2(b). Vickers hardness as a function of temperature for commercial WC cemented carbide and cast eutectic W-Ti-C material. Source: [7].

2.2.1 W-Ti-C Ternary Alloy System

Tungsten-Titanium-Carbon ternary alloy system was explored in detail by Erwin Rudy using melting point, differential-thermoanalytical, x-ray diffraction, and metallograhic techniques on hot-pressed and heat treated, and melted alloy samples [7]. The starting materials used were elemental powders of tungsten, titanium and graphite, as well as powders of titanium carbide and tungsten carbide. The hot-pressed samples were processed in graphite dies, and then homogenized in a tungsten-mesh-element furnace under vacuum (for 120 hours at 1500°C) and high-purity helium (for 20 hours at 1750°C, 4 hours at 2000°C, and 1 hour at 2500°C) to construct the W-Ti-C phase diagram from 1500°C to the melting point range. The isometric view of the phase diagram for W-Ti-C ternary alloy system thus established is shown in Figure 2.2.1.

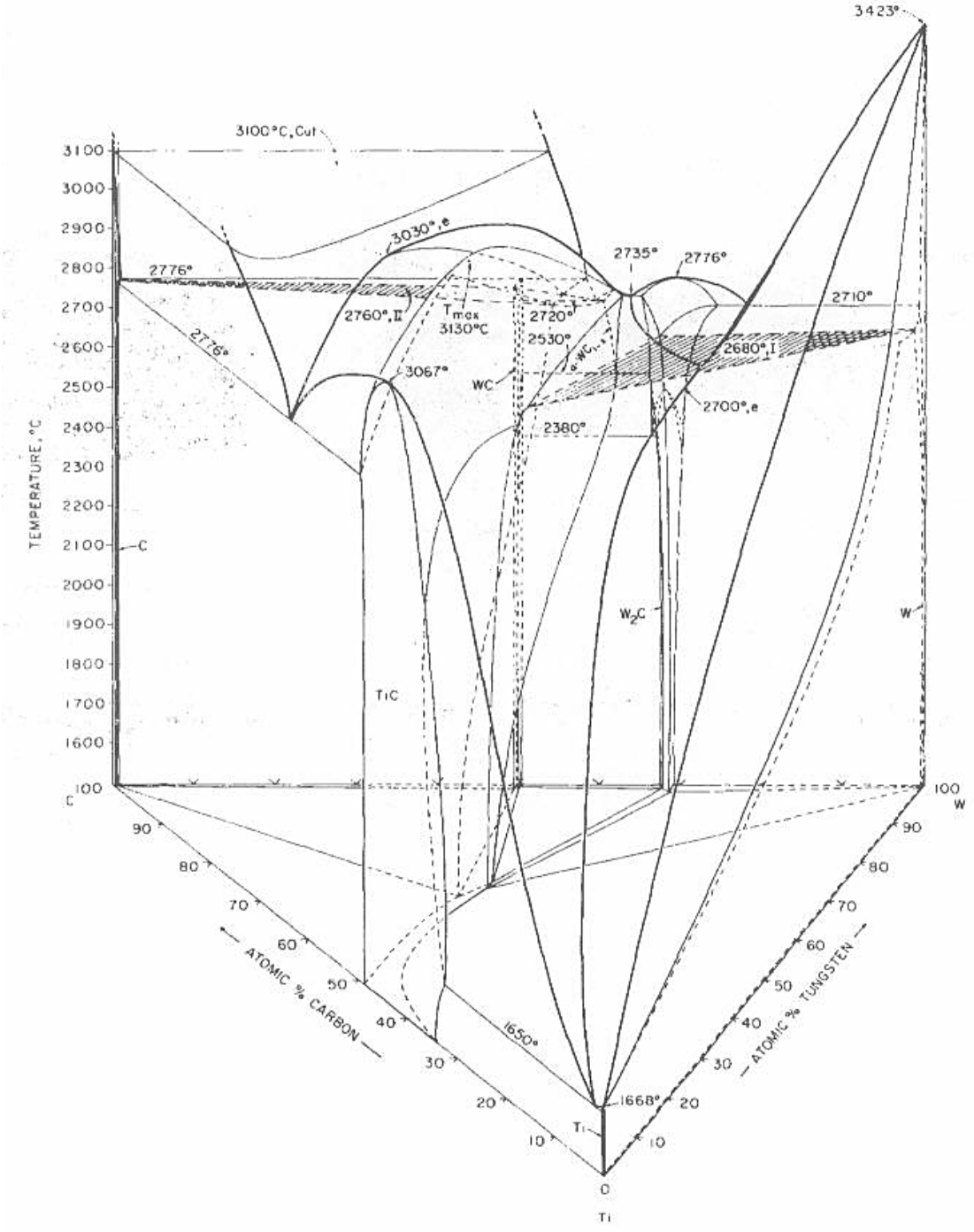

Figure 2.2.1. Isometric representation of the W-Ti-C ternary alloy system.

However, the two most important phase equilibria in the W-Ti-C ternary alloy system that are of practical importance are:

(a) the disproportionation of tungsten rich (more than 60 at.%) monocarbide solid solutions, which is used to obtain small grain size in cemented carbide tools for cutting applications.

(b) the pseudobinary eutectic between tungsten-rich metal alloys and the cubic monocarbide solid solution, which is used to make cast carbide materials with superior hot strength and high resistance to thermal and mechanical shock. The high hot hardness, Figure 2.2(b), and hot strength of the cast carbides are attributed to the small grain size of the cast metal-metal carbide structure i.e., (W,Ti)+(Ti,W)C eutectic, and to the presence of a refractory metal matrix instead of iron metal-base binders used in the cemented carbides.

2.2.2 W-Ti-C-N Cast Carbonitrides: Conventional Route Fabrication

The conventional route, reported by Erwin Rudy in his patent [6], for making castable carbonitride alloys is *arc* (skull) *melting* in a nonconsumable electrode arc furnace, or *plasma arc melting*, and *casting* of the melt in a water-cooled refractory mold. The nitrogen can be introduced either by adding TiN to the melt or by furnishing nitrogen cover gas above the melt at a value less than four atmospheres. It was also reported that *induction melting* in a low frequency (1-2 kHz) induction furnace using graphite mold, and *direct resistance melting* are also possible to make cast carbonitrides. As the mechanical properties are strongly depended on the microstructure of the alloy, the

eutectic or near-eutectic melts of the alloy must be cooled above 20°C per second in order to obtain the fine-grained microstructure.

2.2.3 Effect of Alloying Additions on Performance of W-Ti-C-N Cast Carbonitrides

(i) *Molybdenum*: When substituted up to 5 atomic percent of tungsten in the base alloy system, there is no noticeable change in performance. However, between 5 and 10 atomic percent, it impairs the castability, and above 50 atomic percent results in nose breakdown and chip welding [6].

(ii) *Chromium*: When substituted up to 3 atomic percent of tungsten in the base alloy system, there is no change in performance. However, above 10 atomic percent impairs the castability due to preferential vaporization of chromium during melting in the furnace [6].

(iii) *Rhenium*: Cracking resistance of the material improves when added above 15 atomic percent in replacement for tungsten [6].

(iv) *Zirconium & Hafnium*: When substituted in amounts up to 5 atomic percent for titanium, the tool life improves, but above 15 atomic percent adversely affects the tool performance [6].

(v) *Boron*: When substituted up to 3 atomic percent for carbon or nitrogen, it has no adverse effect on the cutting performance [6].

(vi) *Vanadium, niobium and tantalum*: There is no effect on the tool performance when substituted up to 5 atomic percent of titanium, whereas concentrations in excess of 10 atomic percent result in cracking of the casting and edge-chipping of the tools [6].

(vii) *Oxygen*: When substituted up to 4 atomic percent for carbon or nitrogen, it results in reduced friction and welding tendency, at some sacrifice in strength and cracking resistance [6].

2.2.4 Other Refractory Metal – Refractory Carbide Alloy Systems

Other refractory metal – refractory carbide alloy systems that have been studied in detail are Nb-Ti-C, Mo-Ti-C, and W-Nb-C ternary alloy systems. Rudy [14, 15] investigated these ternary alloy systems and evaluated their phase equilibria by conventional melting and casting of elemental powder mixtures as well as mixtures of metal carbides. According to the phase diagrams, other possible refractory metal – refractory carbide alloy systems are Mo-W-C, Mo-V-C, V-Ti-C, Ta-Hf-C, Ti-Zr-C, V-Nb-C, Zr-Hf-C, Ti-Hf-C, Mo-Nb-C, Nb-Zr-C ternary alloy systems. The metal phases in these ternary systems make binary isomorphous solid solution with each other, whereas the stronger carbide/carbonitride former metal forms the carbides/carbonitrides. The microstructure and the microconstituent phases of the solidified alloy depend upon the initial composition of the starting material and the cooling rate during solidification.

2.3 Laser - Material Interaction

When a laser beam or any other electromagnetic radiation interacts with the surface of a material, some radiation gets reflected, some gets absorbed and some gets transmitted as shown in Figure 2.3(a). As the radiation travels through the new medium it is absorbed according to Beer's law ($I=I_0e^{-\beta z}$), where β is the absorption coefficient, which depends on the medium, radiation wavelength, and the intensity. Multi photon interactions such as Rayleigh scattering, Brillouin scattering, and Raman scattering are more likely to arise during materials processing as it requires high intensity levels. Electromagnetic radiation can be resolved into its components as electric and magnetic field vectors as demonstrated in Figure 2.3(b). The electric field vector of the electromagnetic radiation can set a small elastically bound charged particle in motion. As the force induced by the electric field component is very small in magnitude, it is incapable of vibrating an atomic nucleus and thus does not result in any heat formation.

The photons of the electromagnetic radiation interact with the free or bound electrons, and get absorbed, which is known as *Inverse Bremsstrahlung Effect*. The electrons vibrate after absorbing photons and as a result they either reradiate in all directions or get restrained by the lattice phonons (the bonding energy within a solid or liquid structure). When they are restrained, the phonons cause the structure to vibrate and this vibration is transmitted through the structure by the normal diffusion type processes. The vibrations thus induced by the phonons result in heat formation.

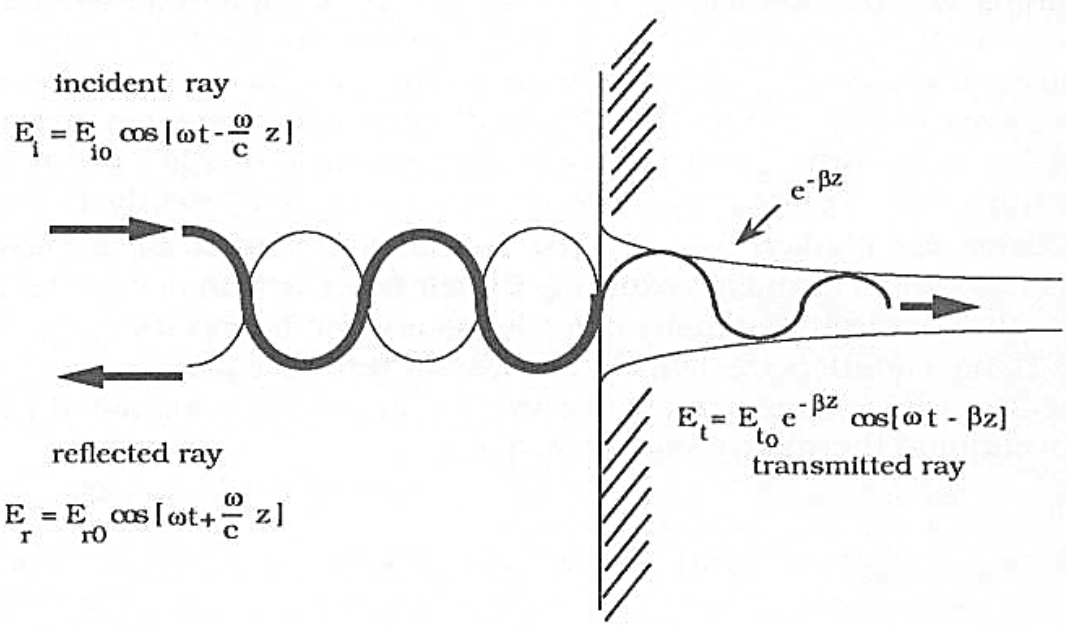

Figure 2.3(a) An electromagnetic radiation interaction with a solid surface.

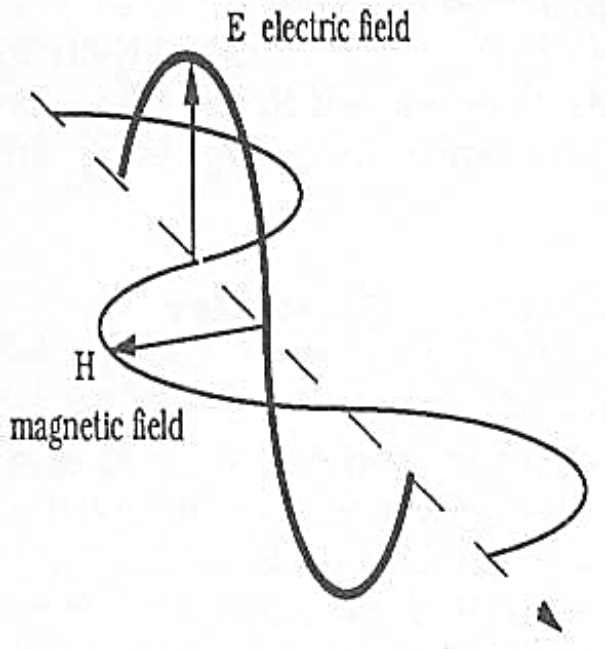

Figure 2.3(b) An electromagnetic radiation resolved into its electric and magnetic field components.

The heat flow is described by Fourier's laws on heat conduction ($q/A = -kdT/dx$). If sufficient amount energy is absorbed, the vibration becomes so strong that the molecular bonding is stretched and the material ceases to exhibit mechanical strength and eventually changes its state from solid to liquid i.e., the material melts [19]. In order to cause any effect on a material, the laser beam must be absorbed by the material under investigation, and *absorption* of the laser beam is the most critical and cumbersome step in laser processing of materials. Thus, laser processing of materials is strongly depended on the "absorption process", which acts as a secondary source of energy inside the material, and determines the state of the irradiated material [17]. The laser for materials processing must be reasonably powerful in order to provide sufficient power density to irradiate the material and trigger the absorption process. The four laser systems that are widely used in industries for materials processing are CO_2 laser, Nd:YAG laser, Yb-doped fiber laser, and excimer laser (pulsed-mode).

Fiber lasers have become leading commercial candidates for numerous applications, including mining, tunneling, welding, brazing, cutting and drilling of rock and concrete, materials modification by surface alloying and cladding. They are fully capable of delivering adequate power with precision to distant targets by means of fiber optics [20]. They have higher wall plug efficiency (~30%) when compared to Nd:YAG laser (~5%) and CO_2 laser (~10%), and improved beam quality with lower input energy requirements. The wall-plug efficiency of a laser system is defined as its total electrical-to-optical power efficiency.

Figure 2.3(c) shows the comparison of energy required to generate a 4.0 kW beam from lamp pumped Nd:YAG (LP:YAG), diode pumped Nd:YAG (DP:YAG), carbon dioxide (CO_2), and Yb-doped high power fiber laser (HPFL) [21]. Moreover, fiber lasers offer greater mobility and durability through a smaller overall size and solid state design. In addition, with projected diode failures exceeding 50,000 continuous hours, little or no maintenance is expected [21].

In the present study, a solid state ytterbium-doped fiber laser (YLR-1000 from IPG Photonics Corporation) of 1075±5 nm wavelength has been used for laser melting, laser coating, and making three-dimensional objects of W-TiC alloy systems. Also, a 3kW neodinium-doped yttrium aluminum garnet laser has been used to make three-dimensional axis-symmetric objects of W-Ti-C alloy on graphite mandrels.

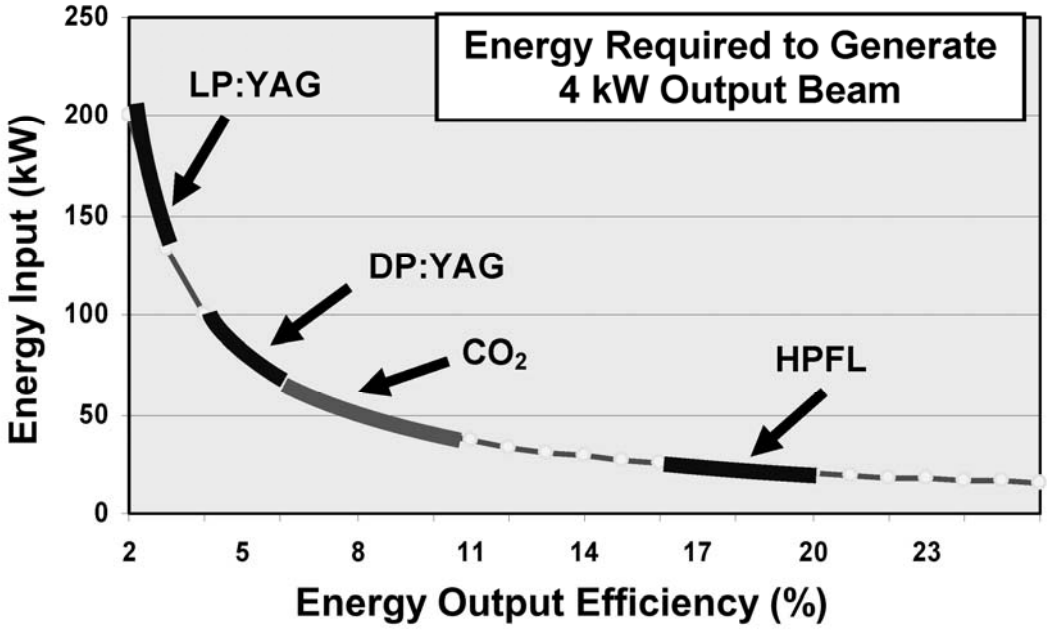

Figure 2.3(c). Comparison of energy required to generate a 4 kW output beam for four different laser systems (lamp pumped YAG laser (LP:YAG); diode pumped YAG laser (DP:YAG); carbon dioxide laser (CO_2); high power fiber laser (HPFL). Source: [21]

2.4 Solid Freeform Fabrication Techniques: A Brief Survey

Several solid freeform fabrication (SFF) techniques have been developed specifically for feedstock materials in powder form [22]. *Three-Dimensional Printing* (3DP) techniques [23, 24] use ink-jet printing technology to bind metal, ceramic or polymer powders and form three-dimensional shapes. *Selective Laser Sintering* (SLS) [25] produces parts in elastomer, polycarbonate and nylon by laser processing powder forms of these materials. *Electron Beam Melting* (EBM) [26, 27], *Laser Powder Deposition* (LPD) techniques [28-32] derived from the blown powder laser cladding technique [33], and several variations of *SLS* [25, 34], including *Selective Laser Melting* [35] and *Direct Metal Laser Sintering* [36], are used to consolidate loose metal powders into solid three-dimensional parts.

A discussion on the two most common forms of delivering the feedstock powders during SFF can be found in reference [37]. The pre-placed powder bed strategy is used in SLS, EBM and drop-on-powder 3DP [23]. Here, a thin and flat layer of feedstock powders is spread evenly over the previous layer of processed material, using either a scraper or a roller. The powders are then consolidated and the process repeated until the final shape is obtained. For SLS, this feedstock delivery strategy allows laser processing to be performed using a galvo-mirror scan head. In other cases feedstock delivery and consolidation are performed simultaneously and without scrapers and rollers. In drop-on-drop 3DP [23], the feedstock powders are fed directly through the print head. In LPD, the feedstock powders are injected directly into the laser beam generated melt pool via a powder feeding nozzle. Although simple to implement, the lateral powder feeding nozzle

configuration [38-41] has scan-direction dependent deposition rates, clearly reported in references [38, 41], and is therefore not suitable for most LPD applications. The limitations of this configuration, discussed in detail in reference [42], were overcome with the introduction of coaxial powder feeding nozzles that enable omni directional materials deposition. Coaxial nozzles have either a conical design, such as reported in [43], or a four lateral nozzle configuration as the one used in the LENS system [29]. Another feedstock delivery strategy, explored by Arcella, Whitney and Krantz during their initial work on the laser forming process [44], involves fluidizing the powders within the laser processing area. Despite the potential to deliver and fuse the feedstock powders simultaneously and without interruptions, the fluidized bed approach has apparently been abandoned.

In the present study, two new solid freeform fabrication techniques have been designed to make three-dimensional components, namely tower nozzle solid freeform fabrication system and axis-symmetric solid freeform fabrication system. Both these systems have unique features and advantages over existing solid freeform fabrication systems.

2.5 Graphite: A Potential High Temperature Structural Material

One of the three forms of carbon – graphite – is known for its exceptional chemical and physicomechanical properties viz. low elastic modulus, low coefficient of thermal expansion, high thermal conductivity, high specific heat, and high resistance to thermal shock [45, 46]. Other key properties that make graphite a potential structural

material are its low specific gravity, good machinability and fairly high strength which sharply increases with rising temperature. It has been reported that at 2500^{o}C graphite is twice as strong as at room temperature [47]. However, graphite and other carbon materials suffer low resistance to oxidation at high temperatures and low resistance to abrasive wear and erosion [48], which limit the usage of graphite as a structural material at elevated temperatures. One of the ways to improve the oxidation resistance of graphite is by depositing a protective film/coating on its surface. Some of the coatings studied earlier are based on carbides and borides of transition metals (Ti, Zr and Cr) and nitrides of aluminum, boron, silicon and titanium. Among others are SiO2, SiC, Si3N4, rhenium, iridium, BN, and glazing coatings based on refractory oxides [46]. The real-time performance of these coatings is strongly dependent on their adhesion with the substrate, and adhesion of any of these coatings is a strong function of their ability to form chemical bonds. Most metals do not wet graphite adequately and hence cannot be deposited easily. However, transition metals are capable of forming stable chemical bonds with carbon and wetting graphite to form well adhered coatings [46].

Other potential coating materials for graphite are sintered refractory carbides and castable refractory carbides/carbonitrides or cermelts. In the present study, W-Ti-C based cermelt coatings were deposited on graphite substrates using two different strategies. In first strategy, the coating was deposited straight on graphite, whereas in second strategy, a titanium intermediate layer was first deposited on graphite prior to the deposition of the main coating.

Cylindrical components of W-Ti-C based alloy systems were also made on graphite mandrels. Graphite mandrel was chosen because it offers three advantages: (i) it does not dilute the deposit, (ii) it can be easily machined, and (iii) it is inexpensive.

CHAPTER 3

EXPERIMENTAL PROCEDURES

In most of the cases, laser processing was done using a solid state ytterbium-doped fiber laser (YLR-1000 from IPG Photonics Corporation) of 1075±5 nm wavelength for solid freeform fabrication and depositing surface coatings based on W-Ti-C cermelt. W-Ti-C cermelt coatings were deposited on graphite substrates and some attempts were also made to deposit them on steel substrates. The laser beam profile was near-Gaussian in nature and the spot shape was near-circular as shown in Figures 3.1 and 3.2. The laser beam was scanned along the processing region with the help of galvanic scan mirrors (ScanLabs Hurryscan30). The values of four different process parameters, namely laser power, scanning speed, track overlap (referred to as **hatch** from this point onwards), and laser spot size were varied in order to obtain the optimum results. The hatch is defined as the distance between the centerlines of the laser beam in subsequent passes as shown in Figure 3.3 and can be correlated to the degree of overlapping of the subsequent laser melted tracks; linear overlap can be calculated as 2r – h, where r is the laser beam radius and h is the hatch. The vacuum chamber used in the experiments integrated with the overhead assembly of fiber laser and galvanic scan mirrors is shown in Figure 3.4. The vacuum chamber was technically designed to perform solid freeform fabrication (SFF) in addition to laser surface alloying. Laser processing of W-Ti-C cermelt was done in an inert atmosphere using industrial grade nitrogen or argon gas.

A 3kW neodinium-doped YAG Hobart laser of 1064 nm wavelength was also used to make three-dimensional axis-symmetric objects on graphite mandrels. The experimental samples were processed in a water-cooled vacuum chamber in an inert gas atmosphere to avoid oxidation. Figure 3.5 shows the axis-symmetric laser powder deposition apparatus used for making axis-symmetric objects.

The starting materials used to make W-Ti-C cermelt three-dimensional components and surface coatings on graphite were tungsten and titanium carbide. The desired chemistry of W-Ti-C cermelt was aimed at the eutectic composition (58 W – 20 Ti – 20 C atomic percent) as per the phase diagram shown in Figure 2.2(a).

3.1 Problems with Graphite and Titanium Carbide.

Graphite and titanium carbide have a common problem when exposed to laser radiation: **carbon evaporation**. Carbon evaporation is a result of their high optical absorptivity (0.8 - 0.9 for graphite [49] and 0.8 for titanium carbide [50]). Carbon evaporation in case of graphite leads to adhesion problem of the deposit, whereas in case of titanium carbide leads to its dissociation and change in stoichiometry. This problem of carbon evaporation can be solved by making a *barrier coating* on the surface of material to be protected. The barrier coating on the material surface prevents its direct exposure to laser radiation and protects it from carbon evaporation. In the present study, graphite is mostly coated with titanium because titanium forms a stable carbide.

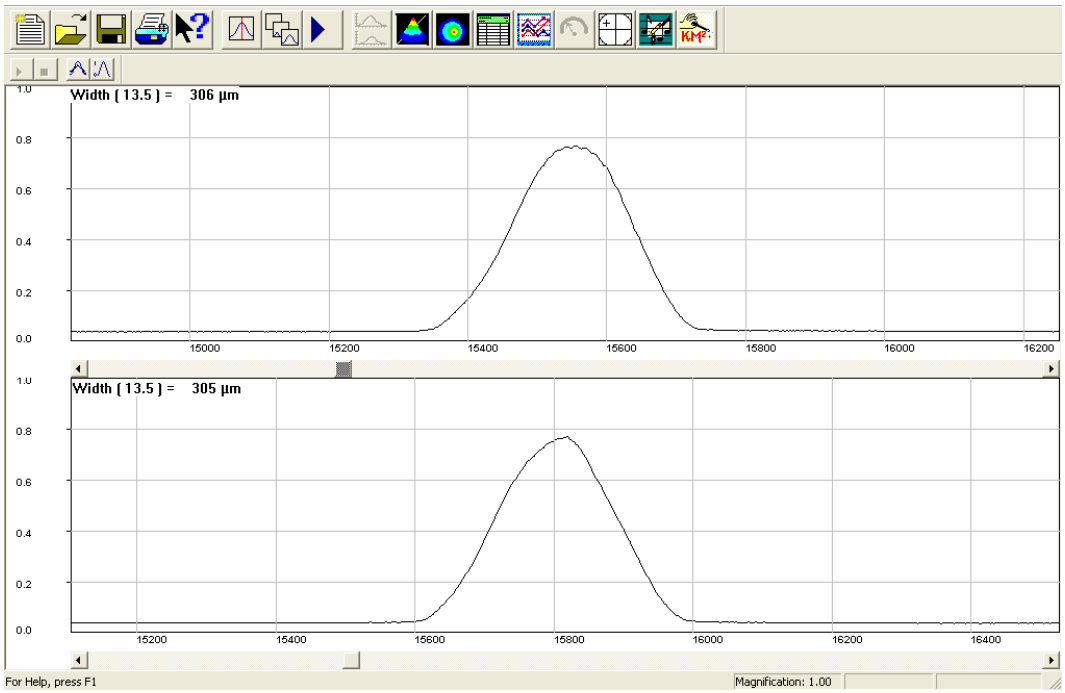

Figure 3.1. Beam profile of the fiber laser taken at 175W using BeamScan® (model: XYLAFIR) by Photon, Inc. It shows the near-Gaussian distribution of the beam intensity. The beam width (FWHM) at 175W is approximately 300 microns.

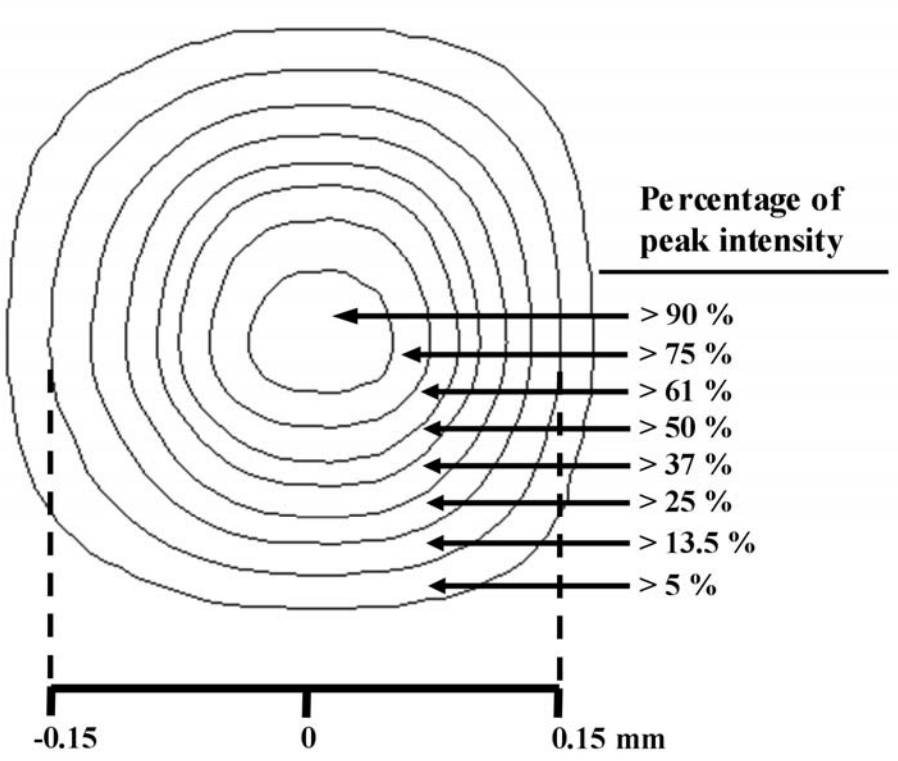

Figure 3.2. Beam intensity profile of the fiber laser taken at 175W. The beam radius is measured at 13.5% of peak intensity as shown in this figure.

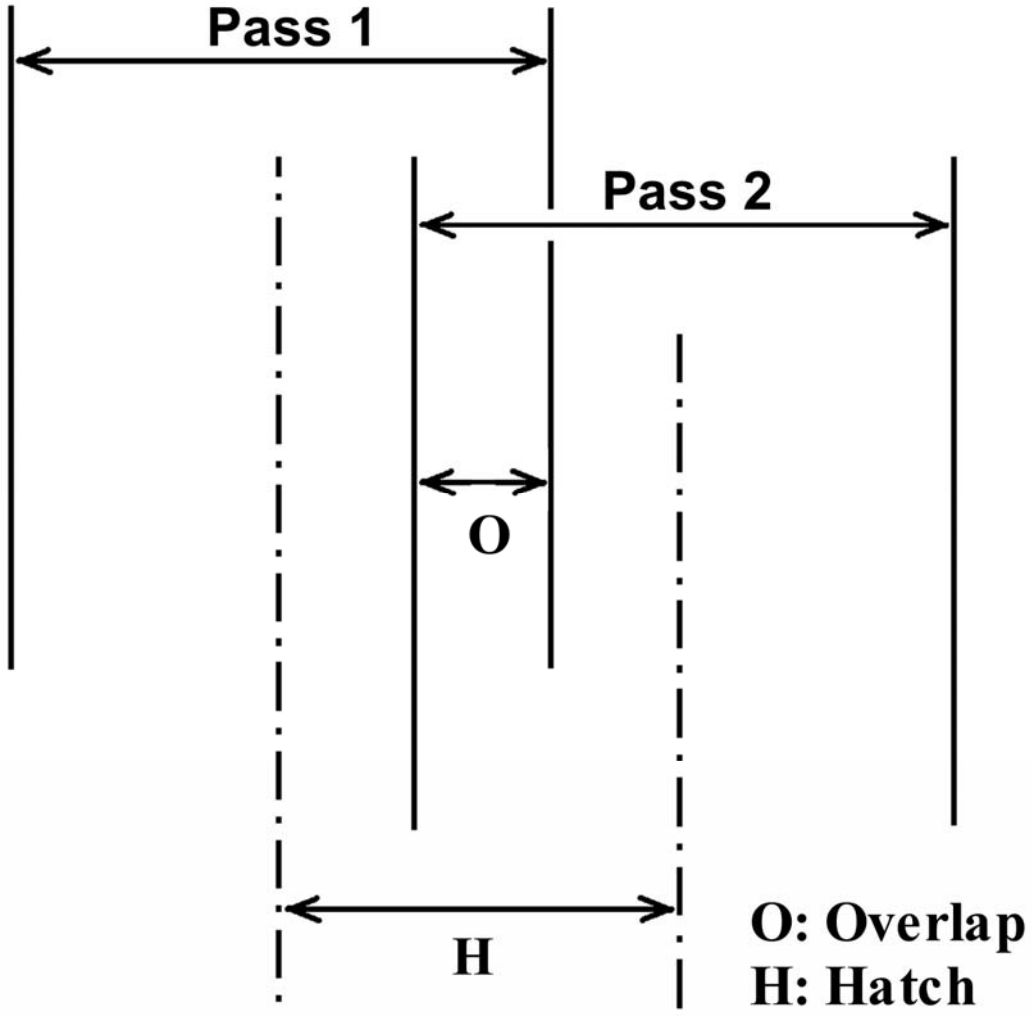

Figure 3.3. The “hatch” is defined as the distance between the centerlines of laser beam in subsequent passes as shown in this sketch.

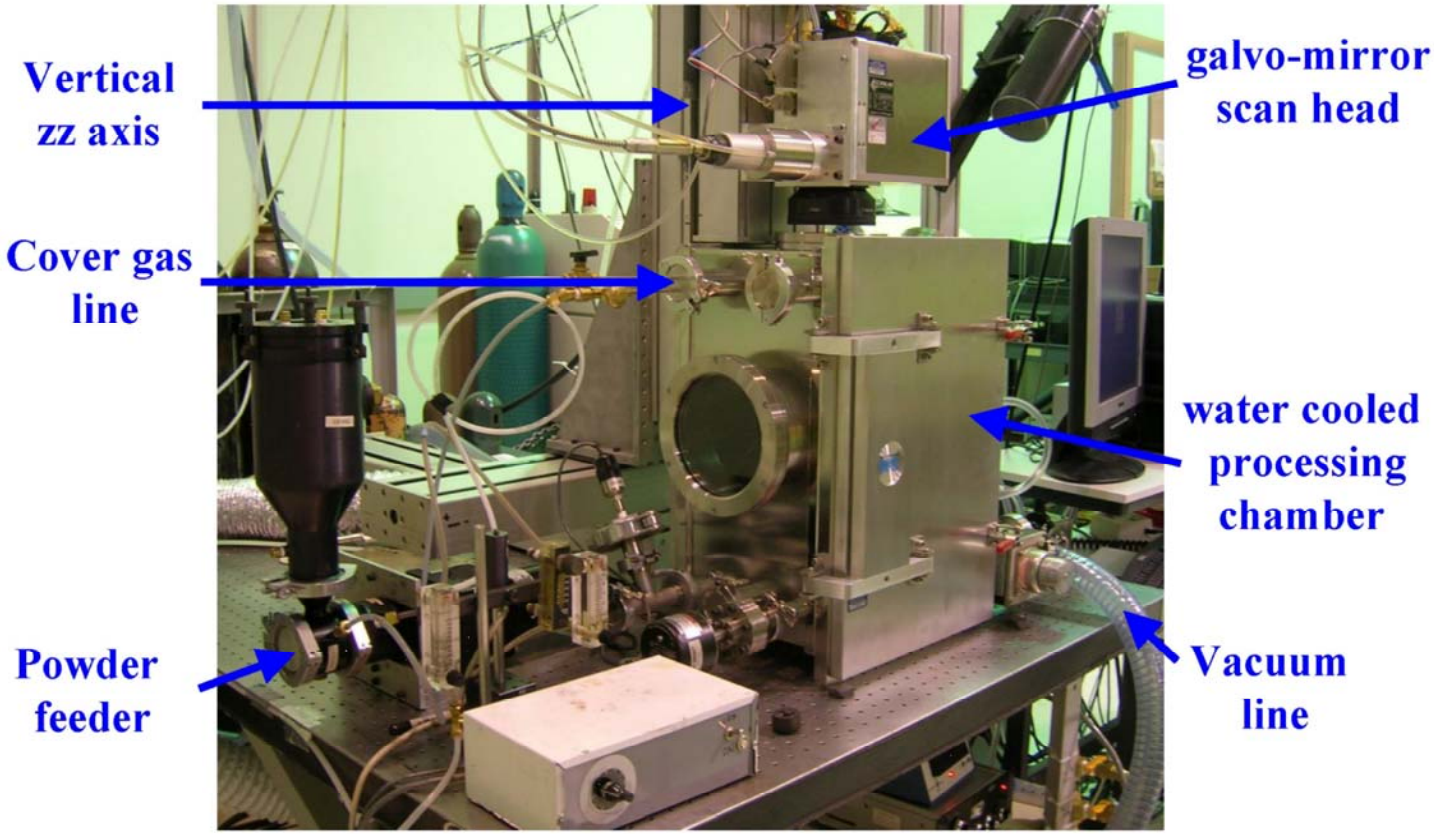

Figure 3.4. Water-cooled vacuum chamber with overhead assembly of fiber laser and galvanic scan mirrors.

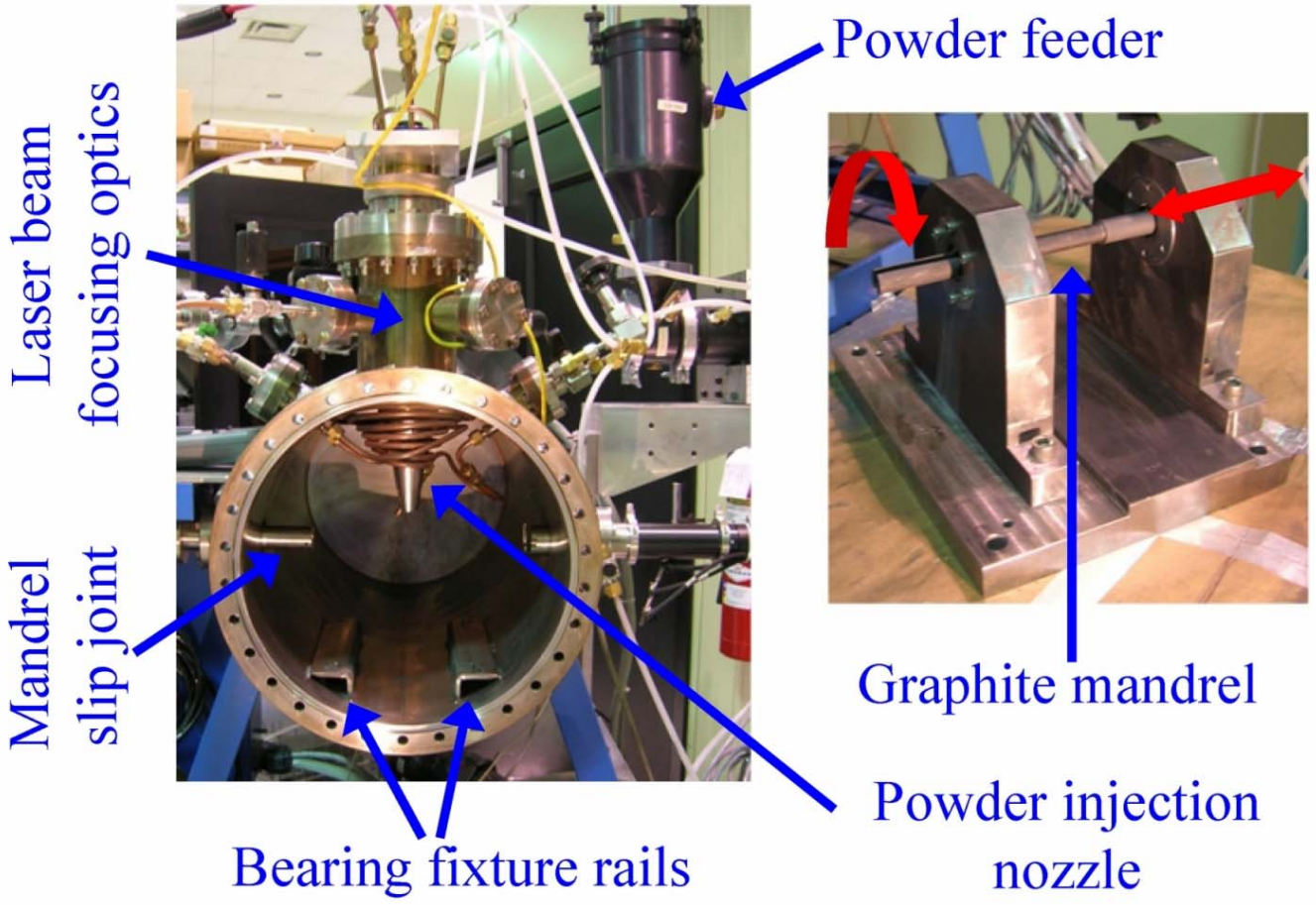

Figure 3.5. Axis-symmetric laser powder deposition apparatus used to make axis-symmetric objects on graphite mandrels. The overhead laser optics assembly is connected to a 3kW Nd:YAG Hobart laser.

In case of graphite mandrels for laser powder deposition, feedstock powders are first sprayed by the LISI^{TM} process on graphite mandrels and then induction heated using a high frequency (3-phase/64 amps/25.4 KVA) solid state induction power supply (model T-10-3-KC-TL by LEPEL Corporation). Induction heating is done to enhance the adhesion of feedstock powders on graphite mandrel and make a hard barrier coating. The induction heating unit used in the experiments is shown in Figure 3.6. A hard barrier coating on graphite mandrel is required to withstand the erosion caused by the powders blown by nozzle during laser powder deposition process. The feedstock powders used to make the barrier coatings depend on the chemistry of the final component to be made. For laser powder deposition of tantalum and molybdenum on graphite mandrels, barrier coatings based on tantalum and molybdenum, respectively, were made. In case of W-Ti-C cermelt on graphite mandrels, a barrier coating based on titanium was made.

In the present study, nanoencapsulated tungsten coated titanium carbide (W-coated TiC) powders were used in place of pure titanium carbide to avoid the problem of carbon evaporation due its dissociation. Nanoencapsulated tungsten coated titanium carbide powders (APS powders) were produced by Advanced Powder Solutions, Inc. (APS) using a fluidized chemical vapour deposition process [51, 52]. The interface of these powders has a melting temperature (~2700 ºC) much lower than that of tungsten (~3422 ºC) and titanium carbide (~3160 ºC). A pictorial description and an SEM view of these particles are shown in Figure 3.7.

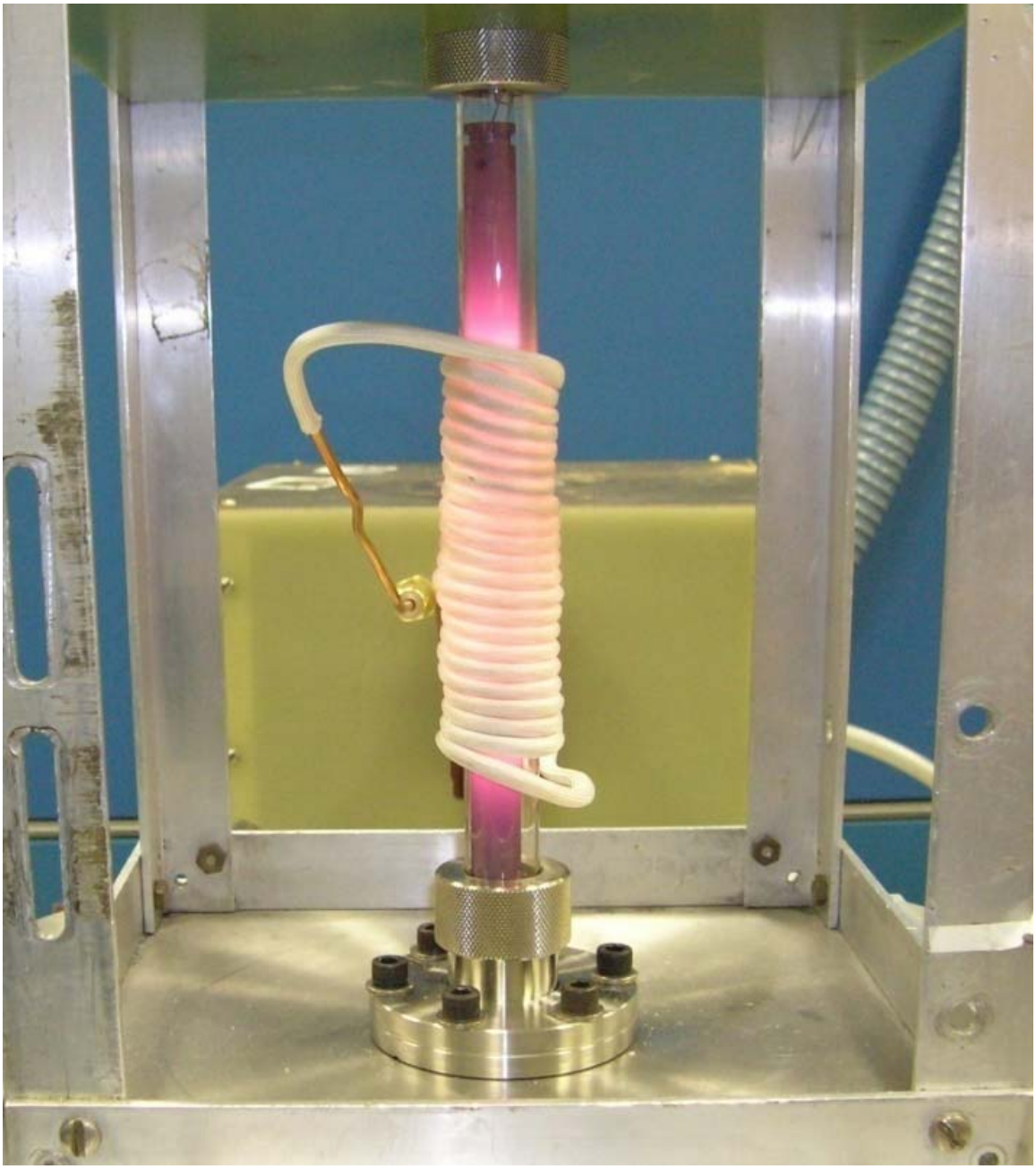

Figure 3.6. Induction heating unit used in the experiments showing induction heating of a graphite mandrel sprayed with feedstock powders.

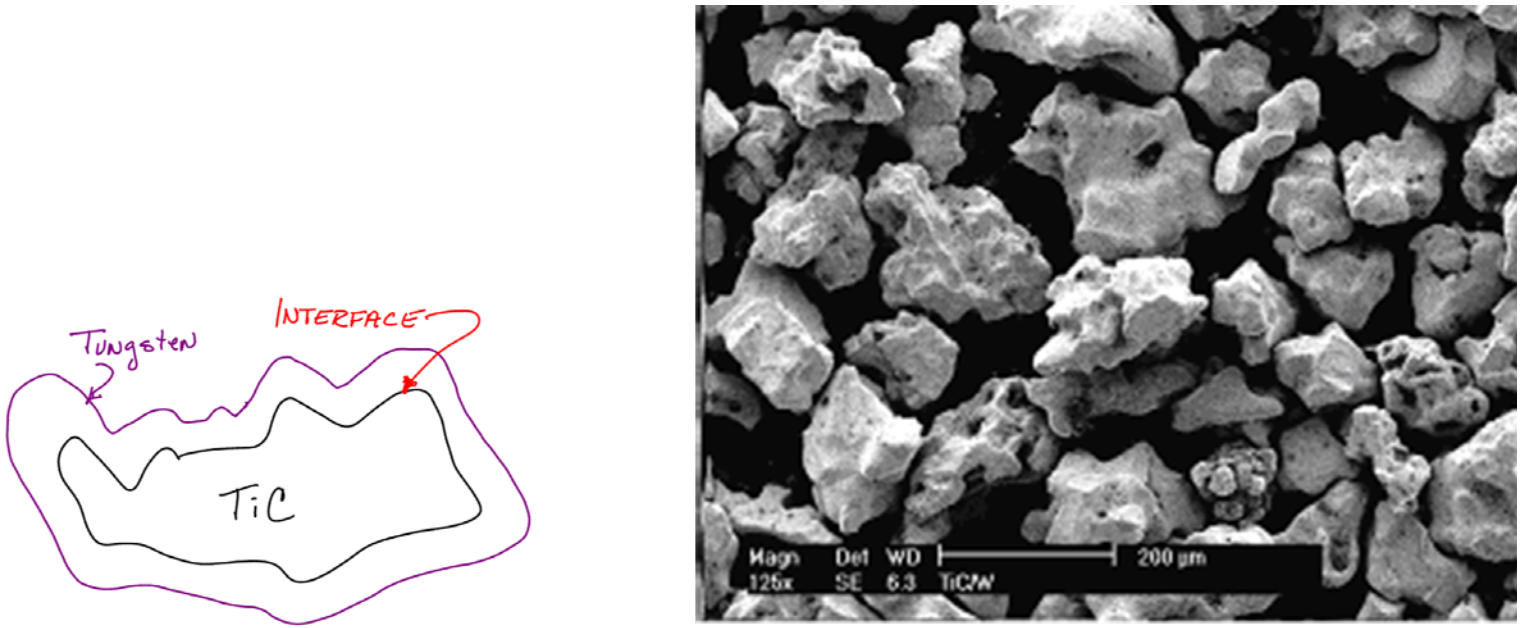

Figure 3.7. APS nanoencapsulated W-coated TiC powders by Advanced Powder Solutions, Inc.

3.2 Powder Compact Trials: W-Ti-C Cermelt

Initial trials on W-Ti-C cermelt were done on powder compact beds to compare the results with that obtained by conventional casting process done by Erwin Rudy in 1970s. Powder compacts were made by mixing tungsten (manufactured by Alfa Aesar) of size -325 mesh size and titanium carbide (manufactured by Cerac Inc.) of size -325 mesh size with 20-30 wt.% i-9 water-based binder (Warren Paint and Co., Nashville). The powder bed compacts were made in a copper gasket of thickness 2 mm on a 6 mm AISI 4140 steel substrate. The compacts were then dried under a heat lamp for several hours. The resulting powder beds were then laser processed in a water-cooled vacuum chamber in 400 torr nitrogen atmosphere. The vacuum chamber used for laser processing is shown in Figure 3.4.

3.3 Tower Nozzle Solid Freeform Fabrication

A special nozzle was designed to perform solid freeform fabrication inside the chamber. This nozzle was termed as "**tower nozzle"** and it has the ability to dispense alloying powder in the processing area homogenously with a constant build-up rate. The construction and working of the tower nozzle is described in [51]. In brief, a fluidized powder stream is injected through this nozzle on the processing area inside a cylindrical confinement. Confinements of different sizes were used to achieve different powder build-up rates. To perform the solid freeform fabrication, the laser optics assembly (also called as scan head) is moved up at the same rate as that of the powder build-up. This is done in order to maintain the laser spot size at a constant value when the component

builds up. Initial trials on tower nozzle powder delivery system done with high speed H13 steel powder proved its potential to perform solid freeform fabrication.

Simple thin wall shapes of laser melted and consolidated W and TiC powders were built, layer by layer, on a water cooled AISI 4140 steel plate in the vacuum chamber shown in Figure 3.4. A mixture of sifted 45-53 μm tungsten (manufactured by Alfa Aesar; -325 mesh size) and 53-75 μm TiC (manufactured by Cerac, Inc.; Product ID: T-1222; -140 +325 mesh) powders were fed into a nitrogen gas stream using a pneumatic Optomec powder feeder and sprayed continuously into the work area during laser processing using a tower nozzle. The laser beam was focused into a 0.9 mm wide spot and scanned at 5 mm/s. Several laser powder deposited parts were built in 600 torr nitrogen atmosphere using different laser beam power settings and powder feed rates, and are shown in Figure 4.2.1(a).

3.4 Axis-symmetric Laser Powder Deposition

The axis-symmetric laser powder deposition was done inside an indigenously developed vacuum chamber as shown in Figure 3.5, and it is different from tower nozzle solid freeform fabrication in terms of powder feeding and laser processing system. In this technique, three-dimensional shapes with cylindrical symmetry were built on graphite mandrels by laser melting a continuous powder feedstock mix delivered in fashion very similar to LENS^{TM} solid freeform fabrication technique. Here, the objective was to make a W-Ti-C cermelt prototype rocket nozzle on a graphite mandrel to find a cost effective alternative to rhenium based rocket nozzles. The construction and working of the axis-

symmetric laser powder deposition system is explained in reference [52]. Initial trials on axis-symmetric laser powder deposition system were done using molybdenum and tantalum powders, and then W-TiC cermelt on graphite mandrels.

3.4.1 Trials with Mo and Ta Laser Powder Deposition

As described in section 3.1, graphite mandrels for laser powder deposition are first prepared by making induction hardened barrier coatings on their surface. For initial trials with molybdenum laser powder deposition, a barrier coating was made from molybdenum powders. It was made by spraying a 100 μ layer of -325 mesh size molybdenum powder (manufactured by Climax Molybdenum Company) mixed with some water-soluble binder followed by induction heating for 5 hours in an induction heating unit as shown in Figure 3.6. Laser powder deposition of molybdenum was done on a molybdenum coated graphite mandrel at 1600-1800 Watts. The graphite mandrel was moved at a rotational speed of 0.2 rotation/sec and a linear speed of 0.2 mm/s to produce a 20 mm long deposit. Analogous to molybdenum, a barrier coating for tantalum laser powder deposition was made from tantalum powders. It was made by spraying a 200 μ layer of -325 mesh size tantalum powder (manufactured by Cerac, Inc.) mixed with some water-soluble binder followed by induction heating for 5 hours in an induction heating unit as shown in Figure 3.6. An example of induction hardened barrier coating on a graphite mandrel is shown in Figure 3.8. Laser powder deposition of tantalum was done on a tantalum coated graphite mandrel at 1200-1400 Watts. The graphite mandrel was moved at a rotational speed of 0.2 rotation/sec and a linear speed of 0.2 mm/s to produce a 30 mm long deposit.

3.4.2 W-TiC Laser Powder Deposition on Graphite Mandrels

In case of W-TiC cermelt laser powder deposition, a titanium based barrier coating was made on a graphite mandrel by induction heating a 200 μ thick layer of titanium. Laser powder deposition of W-TiC was done by blowing a mixture of 75 wt.% tungsten (32-38 μ) and 25 wt.% APS tungsten coated titanium carbide (75-106 μ) powders. Laser processing was done at 1200-1600 W to obtain fully melted structure. The mandrel rotational speed was kept constant at 0.2 rotation/sec with a linear speed of 0.2 mm/s to produce a 30 mm long deposit.

3.4.3 W-TiC Cermelt Deposits on Graphite Mandrels.

W-TiC cermelt cylindrical deposits were made on graphite mandrels by laser processing barrier coatings based on W-TiC eutectic composition on graphite mandrels. The experiments were performed in the axis-symmetric laser powder deposition apparatus (Figure 3.5), but in this strategy no powder was blown from the nozzle. This strategy was adopted to defeat the problems of powder segregation as explained in section 4.3.2. In the first attempt, a 0.6 mm barrier coating of W-TiC eutectic composition was made by induction hardening on a graphite mandrel. A 30 mm long and 300 μ thick cylindrical deposit was made by laser processing at 1500 W. In the second attempt, a 1.3 mm barrier coating of W-TiC eutectic composition was laser processed at 1600 W to make a 30 mm long and 1 mm thick cylindrical deposit.

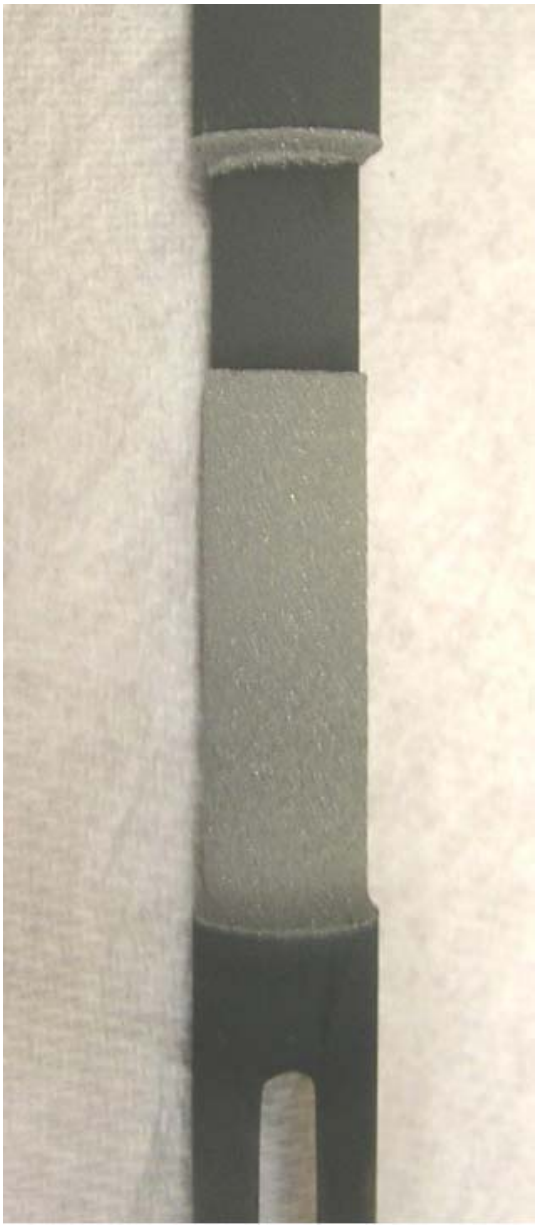

Figure 3.8. An induction hardened barrier coating on a graphite mandrel.

3.5 W-Ti-C Cermelt Coatings on Graphite Plates

For depositing W-Ti-C cermelt coating on graphite two different strategies were used. In first case, the W-Ti-C cermelt coating was deposited directly on the graphite substrate using LISI^{TM} process. In second case, a barrier coating based on titanium was deposited prior to the deposition of W-Ti-C cermelt coating. Unlike axis-symmetric laser powder deposition on graphite mandrels where a barrier coating is induction hardened prior to laser powder deposition, here a barrier coating is laser deposited on graphite substrate i.e., the barrier coating is fully melted and metallurgical bonded to graphite.

The graphite substrates used in experiments were semiconductor grade graphite plates (manufactured by Poco Graphite, Inc.) of thickness 6 mm. They were sand blasted before the experiments to give them a matt finish in order to enhance the adhesion properties. Laser processing was done inside a water-cooled chamber shown in Figure 3.4 with a 1kW YLF-1000 (IPG Photonics Corporation) fiber laser. The laser processing system and the laser beam characteristics are explained in detail in the beginning of chapter 3. The laser beam was scanned along the processing region by galvanic scan mirrors (ScanLabs HurryScan30). The values of laser power, scanning speed, focal spot size, and hatch were varied for screening purpose in order to obtain optimum results with respect to homogeneity and continuity of the cermelt coating.

3.5.1 W-Ti-C Cermelt Coating Straight on Graphite Substrate

The W-Ti-C cermelt precursor was made by mixing nanoencapsulated powder of tungsten coated titanium carbide (referred to as APS powder, manufactured by Advanced Powder Solutions, Inc.) of size approximately 10 microns with 75 wt.% i-9 LISI^{TM} binder (Warren Paint and Color Company, Nashville, TN) as shown in Table 3.5.1(a). The precursor mixture was applied on the graphite substrate with a paint brush to approximately 300 microns thickness, and then dried under heat lamp for several hours before laser processing. Laser processing was done in nitrogen atmosphere maintained at 400 torrs inside a vacuum chamber and a focal spot size of 1.5 mm for all the experiments. The screening parameters used for processing in initial trials are shown in Table 3.5.1(b). The optimized processing parameters found are shown in Table 3.5.1(c).

Table 3.5.1(a): Precursor mixture composition for W-Ti-C cermelt coating on graphite.

W-Ti-C coating precursor	=	8 gms APS powder + 6 gms i-9 LISI^{TM} binder

Table 3.5.1(b): Screening parameters for processing W-Ti-C cermelt coating on graphite.

Precursor thickness (microns)	**Laser power (watts)**	**Hatch (mm)**	**Scanning speed (mm/s)**
300	500 – 600	0.4	10 – 15

Table 3.5.1(c): Optimized parameters for processing W-Ti-C cermelt coating on graphite.

Precursor thickness (microns)	**Laser power (watts)**	**Hatch (mm)**	**Scanning speed (mm/s)**
300	550	0.4	15

3.5.2 W-Ti-C Cermelt Coating on Titanium Coated Graphite

W-Ti-C cermelt coating on titanium coated graphite was done in two stages. First, a titanium barrier coating was deposited on graphite substrate and then the final W-Ti-C cermelt coating was deposited on titanium coated graphite. Titanium barrier coating precursor was made by mixing titanium (manufactured by CERAC Inc.) of mesh size -325 with 60 wt.% i-8 LISI^{TM} binder as shown in Table 3.5.2(a). The precursor mixture was sprayed on sand blasted graphite substrates with the help of an air spray gun (Crescendo®, Model 175 by Badger Air-Brush Co., IL), and then dried under a heat lamp for several hours before laser processing. The values of laser power, scanning speed, track overlap, and laser focal spot size values were varied for screening in initial trials and are shown in Table 3.5.2(b) and the optimized parameters found are shown in Table 3.5.2(c). After laser processing titanium barrier coating on graphite surface, precursor mixture for W-Ti-C cermelt coating was sprayed on titanium coated graphite. The W-Ti-C precursor was made by mixing APS powder of approximate size 10 microns and tungsten (manufactured by Alfa Aesar GMBH & Co KG) of size 12 microns with 33 wt.% i-8 LISI^{TM} binder as shown in Table 3.5.2(d), and then dried under a heat lamp before laser processing. The original nanoencapsulated tungsten coated titanium carbide powder (APS powder) is TiC rich which shifted its stoichiometry to hypereutectic region. Thus, additional tungsten was added to the APS powder in order to shift the stoichiometry of the precursor mixture closer to the eutectic point at 85.55 wt.% W and 14.45 wt.% TiC. This new mixture was termed as modified APS powder, which was near eutectic as per the phase diagram shown in Figure 2.2(a). The screening parameters and

optimized parameters for laser processing of W-Ti-C cermelt coating on titanium coated graphite are shown in Tables 3.5.2(e) and 3.5.2(f), respectively.

Table 3.5.2(a): Precursor mixture composition for titanium intermediate coating on graphite.

Ti intermediate layer precursor	=	10 grams Ti + 6 grams i-8 LISI^{TM} binder

Table 3.5.2(b): Screening parameters for processing titanium layer on graphite.

Precursor thickness (microns)	**Laser power (watts)**	**Hatch (mm)**	**Scanning speed (mm/s)**	**Focal spot size (mm)**
75 – 85	120 – 250	0.05 – 0.2	10 – 15	0.3 and 0.9

Table 3.5.2(c): Optimized parameters for processing titanium layer on graphite.

Precursor thickness (microns)	**Laser power (watts)**	**Hatch (mm)**	**Scanning speed (mm/s)**	**Focal spot size (mm)**
75 – 85	225 – 250	0.175	12	0.9

Table 3.5.2(d): Precursor mixture composition for W-Ti-C cermelt coating on titanium coated graphite.

W-Ti-C coating precursor	=	15 gms modified APS powder + 5 gms i-8 LISI^{TM} binder

Table 3.5.2(e): Screening parameters for processing W-Ti-C cermelt coating on titanium coated graphite.

Precursor thickness (microns)	**Laser power (watts)**	**Hatch (mm)**	**Scanning speed (mm/s)**	**Focal spot size (mm)**
100 – 125	250 – 500	0.2 – 0.4	5 – 12	0.9 and 1.5

Table 3.5.2(f): Optimized parameters for processing W-Ti-C cermelt coating on titanium coated graphite.

Precursor thickness (microns)	Laser power (watts)	Hatch (mm)	Scanning speed (mm/s)	Focal spot size (mm)
100 – 125	450	0.2	5	0.9

3.6 W-Ti-C Cermelt Coatings on Steel

The eutectic of the W-Ti-C ternary system is at 2700°C with the composition 58 W – 20 Ti – 22 C atomic percent (Figure 2.2(a)). The laser surface alloying of such a high-melting-point alloy directly on steel, whose melting point is approximately in the range 1450°C to 1550°C, can cause serious fabrication problems. The two major concerns are dilution and formation of stable intermetallics between Fe & W and Fe & Ti. The dilution is caused by alloying of the coating elements with the substrate elements and it cannot be completely eliminated because of the nature of the laser surface alloying process. In some cases, it can only be reduced to a certain extent by optimizing the processing parameters in such a way that the desired coating properties are not much affected due to alloying. However, laser deposition of W-Ti-C based high-melting-point cermelt directly on steel causes high dilution because of large difference between the melting points of the W-Ti-C precursor material and the steel substrate. Fe and W form three intermetallics, namely λ phase (Fe_2W), δ phase (FeW), and μ phase (Fe_7W_6) and can be seen in the Fe – W binary phase diagram [53]. λ phase (Fe_2W) and δ phase (FeW) are stable low temperature intermetallics that can exist at room temperature, where as μ phase (Fe_7W_6) is a high temperature intermetallic. Fe and Ti form two stable

intermetallics, namely TiFe and $TiFe_2$ [55]. Intermetallics are highly ordered structures that are brittle in nature and are not desired in coatings.

One of the best ways to deposit such a high melting point alloy coating on steel is the deposition of intermediate layers between steel and the main alloy coating. In the present study, molybdenum-on-chromium dual coating was deposited on AISI 4130 alloy steel where chromium is the intermediate layer between the substrate and molybdenum coating. First, a chromium coating was deposited on steel using the Cr-CrB_2 eutectic composition, and subsequently a molybdenum coating using the Mo-MoB eutectic composition was deposited on the chromium layer. The chromium intermediate layer and the molybdenum final coating chemistries are based on their eutectic systems with boron (i.e. Cr-B and Mo-B eutectic systems). This helps in two ways: (i) by reducing the melting point of the alloy, and (ii) by increasing the hardness by solid solution strengthening. As a eutectic mixture melts at a temperature lower than its constituent elements, it further reduces dilution in the coating due to melting of the substrate. Cr-B eutectic (Cr-3.1wt.% B) melts at ~1630^{o}C and Mo-B eutectic (Mo-3wt.% B) melts at ~2180^{o}C [55]. CrB_2 and MoB have been used as sources of boron for the chromium layer and the molybdenum coating, respectively instead of elemental boron. We made use of Cr-CrB_2 eutectic composition to make the intermediate layer and Mo-MoB eutectic composition to make the main coating. Laser processing was done in the apparatus shown in Figure 3.4. The details of molybdenum-on-chromium dual coating on steel are discussed in detail in reference [56]. However, only important results of this experiment are presented in section 4.5.

CHAPTER 4

RESULTS & DISCUSSION

Section 4.1 presents results and discussion on powder compact bed trials done on W-Ti-C cermelt using tungsten and titanium carbide as the starting material. Section 4.2 presents results of tower nozzle solid freeform fabrication of W-Ti-C cermelt thin wall structures. The first part of section 4.3 presents results on trials done on axis-symmetric laser powder deposition of tantalum and molybdenum on graphite mandrels; whereas the second part deals with laser powder deposition of W-Ti-C cermelt rocket nozzles on titanium coated graphite mandrels. The first part of section 4.4 presents results on W-Ti-C cermelt coating deposited straight on graphite substrate and the second part presents results on W-Ti-C cermelt coating deposited on titanium coated graphite substrate. Section 4.5 presents a possible method of depositing W-Ti-C cermelt coating on steel by adopting the strategy of depositing compatible intermediate layers prior to the deposition of the main coating. This section presents some selected results of molybdenum-on-chromium dual coating deposited on AISI 4130 steel using LISI^{TM} process.

4.1 Powder Compact Trials: W-Ti-C Cermelt

The starting material used in the trials for making W-Ti-C cermelt was a mixture of tungsten and titanium carbide powders (as described in section 3.1) instead of elemental powders as used in the conventional method i.e., centrifugal casting in a graphite mould. Laser processing was done in a 400 torr nitrogen atmosphere inside a water-cooled vacuum chamber to avoid the formation of any oxidation products in the final material. A W-TiC powder compact bed with several laser processed test patches made at different sets of processing conditions is shown in Figure 4.1(a).

4.1.1 Microstructural Characterization

Samples exhibiting a refractory cast carbide microstructure were obtained after processing the W-TiC powder compacts at 5 – 20 mm/s with 400 – 500 W laser beam focused into a 1.5 mm circular spot and using a hatch spacing of 0.4 – 0.7 mm between consecutive laser passes. A cross-sectional view of a layer of laser consolidated materials is displayed in Figure 4.1(b) and it shows two distinct regions that are present within the consolidated layer. The lower section presents a sintered carbide type microstructure formed by partial melting of the precursor powders during laser processing. The upper section presents a microstructure consisting of primary dendrites of (Ti,W)C surrounded by the (W,Ti) + (Ti,W)C eutectic as shown in scanning electron micrographs in Figures 4.1(c) and Figure 4.1(d) at higher magnifications.

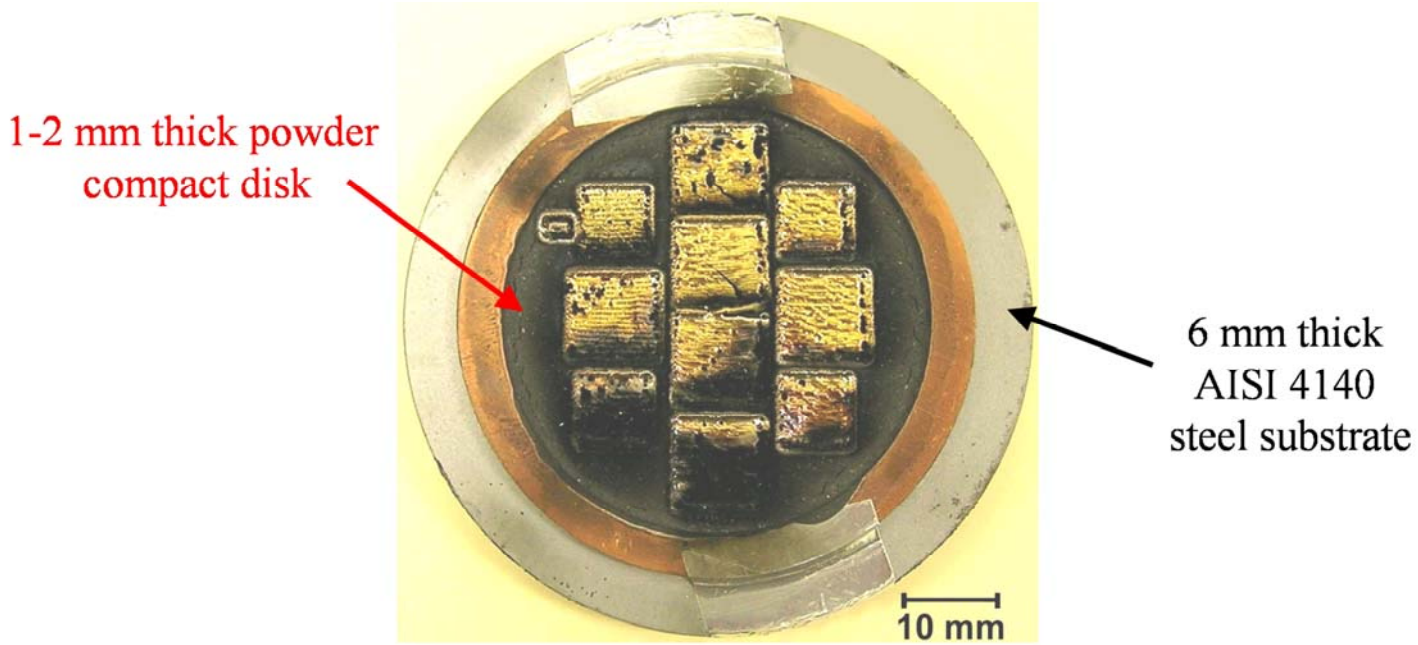

Figure 4.1(a). A W-TiC powder compact bed made by mixing tungsten and titanium carbide powders with i-9 LISI^{TM} water-soluble binder. The various laser processed (golden) areas represent trials done at different processing conditions.

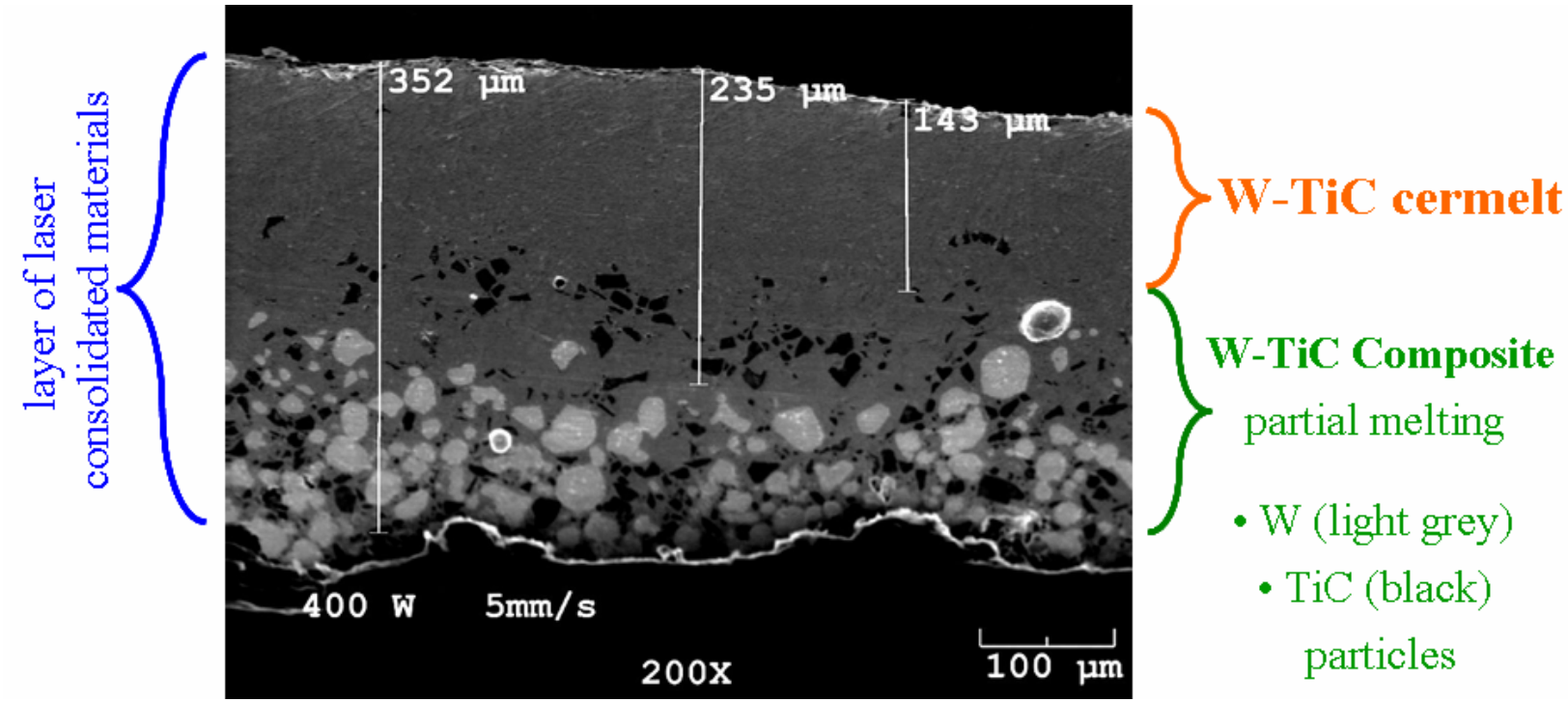

Figure 4.1(b). An SEM cross-sectional view of a laser processed W-TiC powder compact. The lower section of this layer consists mostly of unmelted W (light grey) and TiC (black) particles. A higher magnification image of the upper section is shown in Figure 4.1(c).

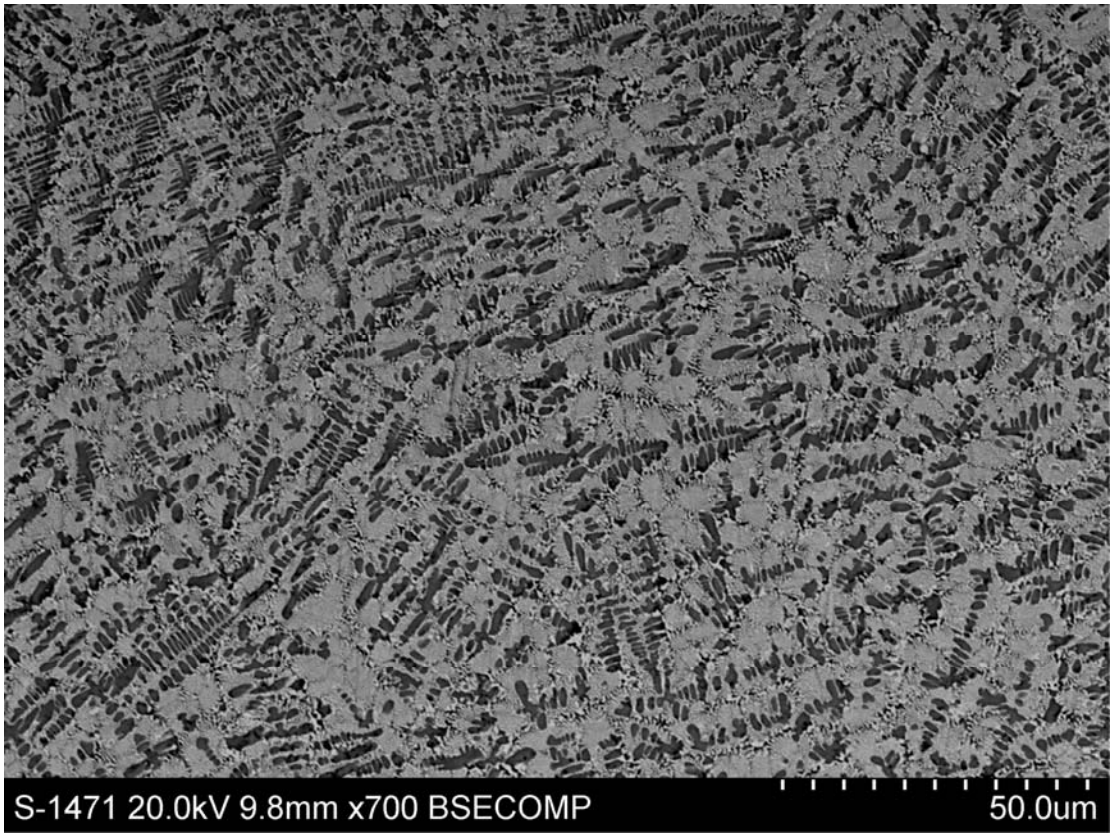

Figure 4.1(c). An SEM micrograph of the cast carbide microstructure formed by laser processing a mixture of tungsten and titanium carbide powders. Dark areas are primary dendrites of (Ti.W)C. Light areas are the (W,Ti) + (Ti,W)C eutectic, seen in more detail at higher magnification in Figure 4.1(d).

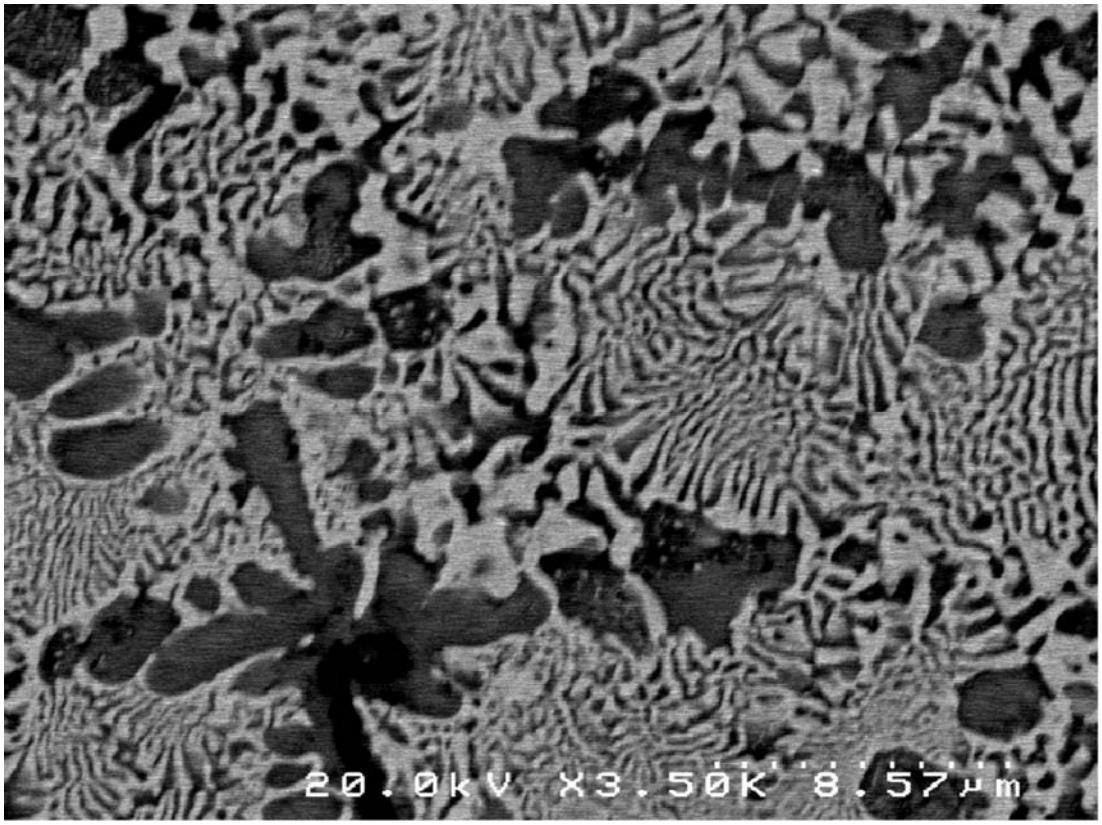

Figure 4.1(d). An SEM image of the eutectic structure of the cast carbide. The light phase is the (W,Ti) metallic phase and the dark regions are the (Ti,W)C ceramic phase.

The chemical composition of the W – TiC powder mix used was hypereutectic and according to the phase diagram, refer Figure 2.2(a), the first solid phase to form from the liquid phase during solidification is the (Ti,W)C ceramic phase. Thus, according to this phase diagram, the resulting microstructure should consist of the carbide phase and the eutectic of metal and carbide phases, which can be seen in Figures 4.1(c) and 4.1(d). The cast carbide microstructure, shown in Figure 4.1(c), appears only in regions where the precursor powders underwent complete melting prior to resolidification. The eutectic phase has a lamellar structure and in fact in some locations it appears to have a divorced structure as well.

4.1.2 Microindentation Hardness

Microindentation hardness testing was done on a LECO LM 300AT microhardness tester, integrated with LECO AMH32 software, under a load of 100 gf for 15 seconds using Vickers indenter. Microhardness measurements performed on the cast carbide material revealed a hardness ranging typically between 1100 and 1300 HV, which is consistent with the data reported by Rudy et al [7] as shown in Figure 2.2(b). The scanning electron micrograph of the microhardness indentation on the cast carbide material is shown in Figure 4.1(e).

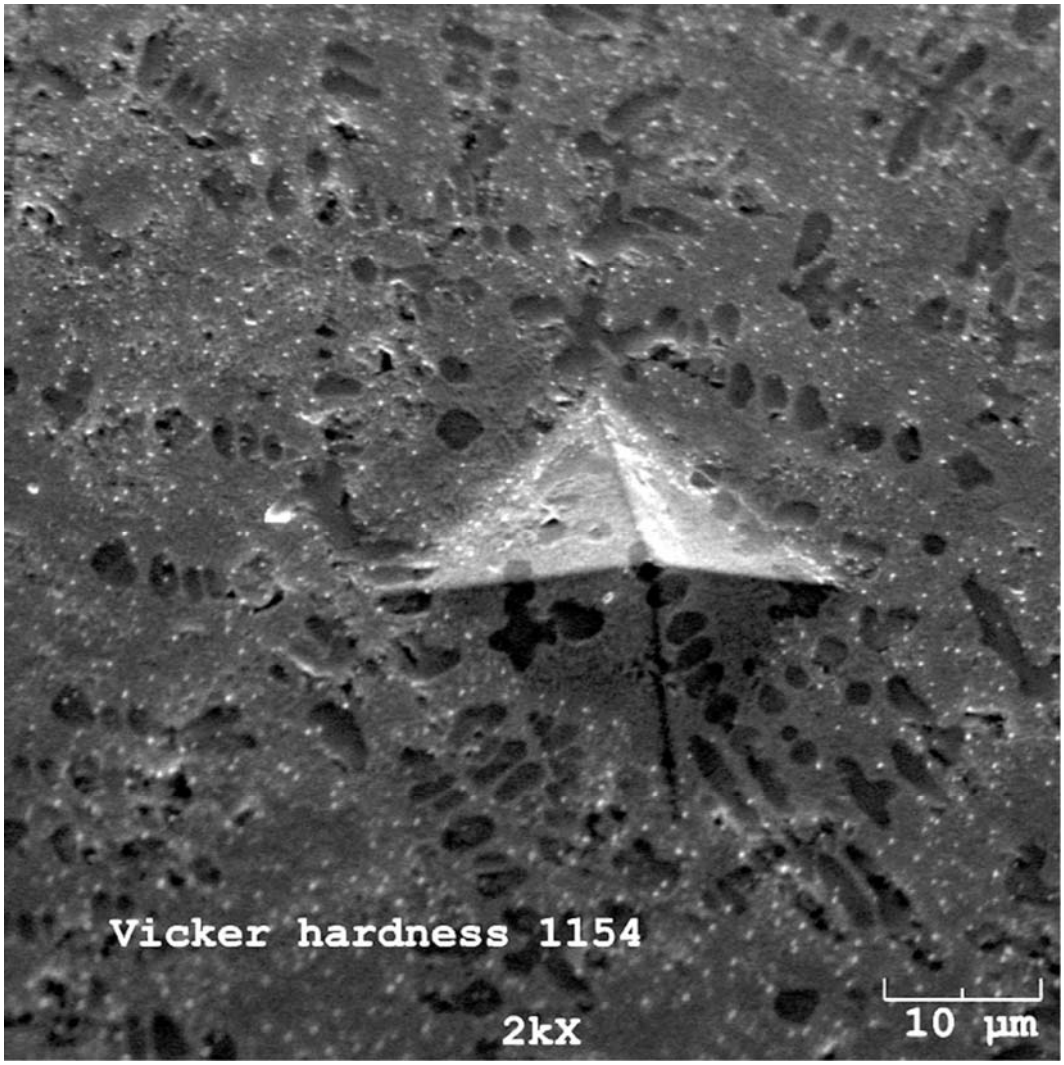

Figure 4.1(e) An SEM image of a Vickers microhardness impression on the cast carbide material performed using a 500g load.

4.2 Tower Nozzle Solid Freeform Fabrication

Tower nozzle solid freeform fabrication of W-Ti-C cermelt was done at different processing conditions to find the optimum results. Initial trials were done using a mixture of tungsten, titanium, and carbon nanoparticles, but melting and retaining carbon in the solution to form carbides and carbonitrides was a problem. To avoid this problem, the starting material used was a mixture of tungsten and titanium carbide, where titanium carbide becomes the source of carbon to form carbides or carbonitrides.

4.2.1 Microstructural Characterization

SEM analysis was done on an ISI Super IIIA Scanning Electron Microscope equipped with IXRF Energy Dispersive Spectrometer (version 1.3 RevP). Cross-sectional samples were cut, mounted on bakelite using hot press, ground and polished down to emery grit number 1200 followed by cloth polishing. Finally, they were etched with modified Murakami's reagent to reveal the microstructure. Figure 4.2.1(b) shows the scanning electron micrograph (taken at 300X magnification) of the cross-section of W-Ti-C thin wall structure made by tower nozzle solid freeform fabrication technique at 450 Watts laser beam power. It shows the presence of fine dendrites of (Ti,W)C in a matrix of eutectic alloy of (W,Ti) + (Ti,W)C, similar to what was seen in case of powder compact trials. The materials thus produced do present some inhomogeneities, such as small unmelted regions, and cracks that appear mainly along the interface between adjacent layers as shown in Figure 4.2.1(c), where a continuous deposit of (Ti,W)C forms during solidification.

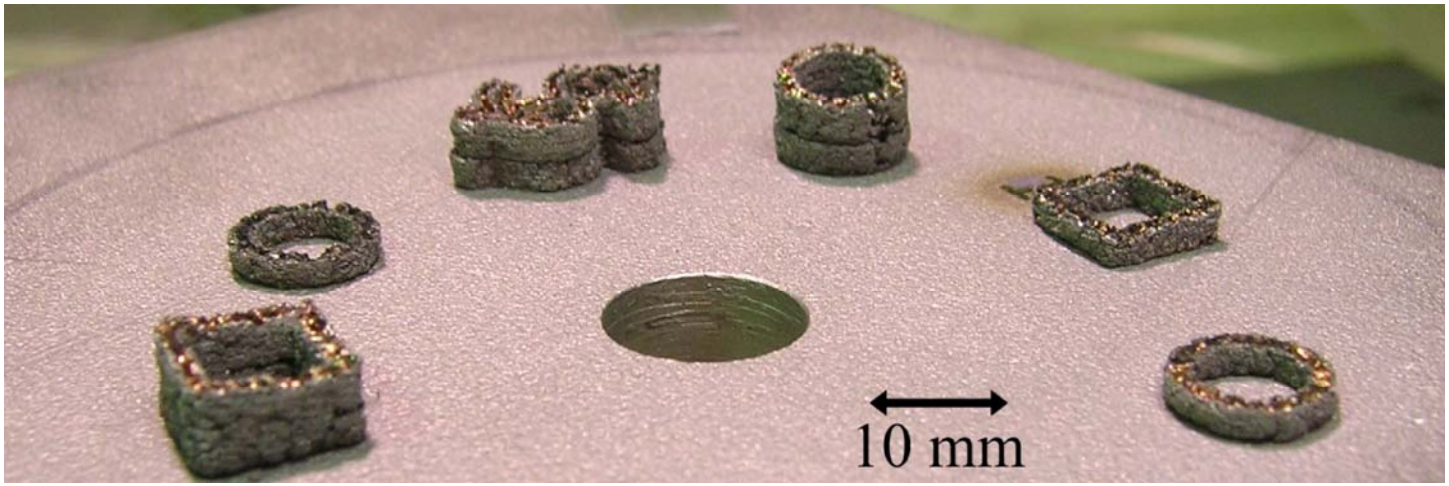

Figure 4.2.1(a) Laser powder deposited shapes, with 10 and 20 layers of laser consolidated W-TiC powders.

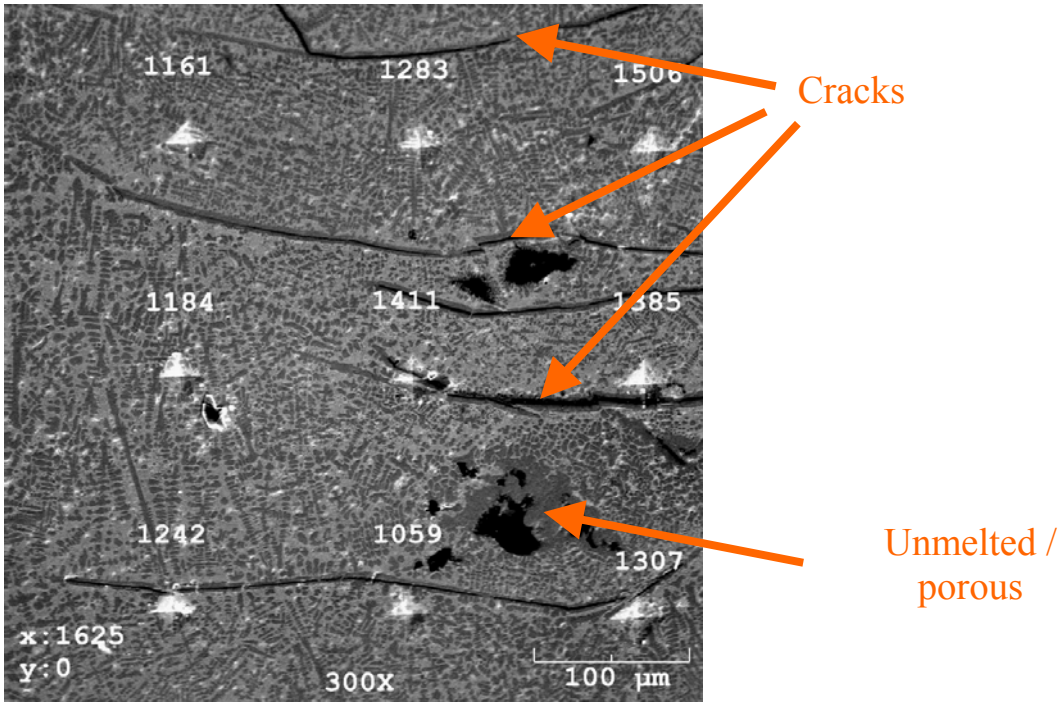

Figure 4.2.1(b) An SEM cross-sectional view of the microstructure of a laser powder deposited cast carbide multilayer. Vickers hardness measurements are indicated.

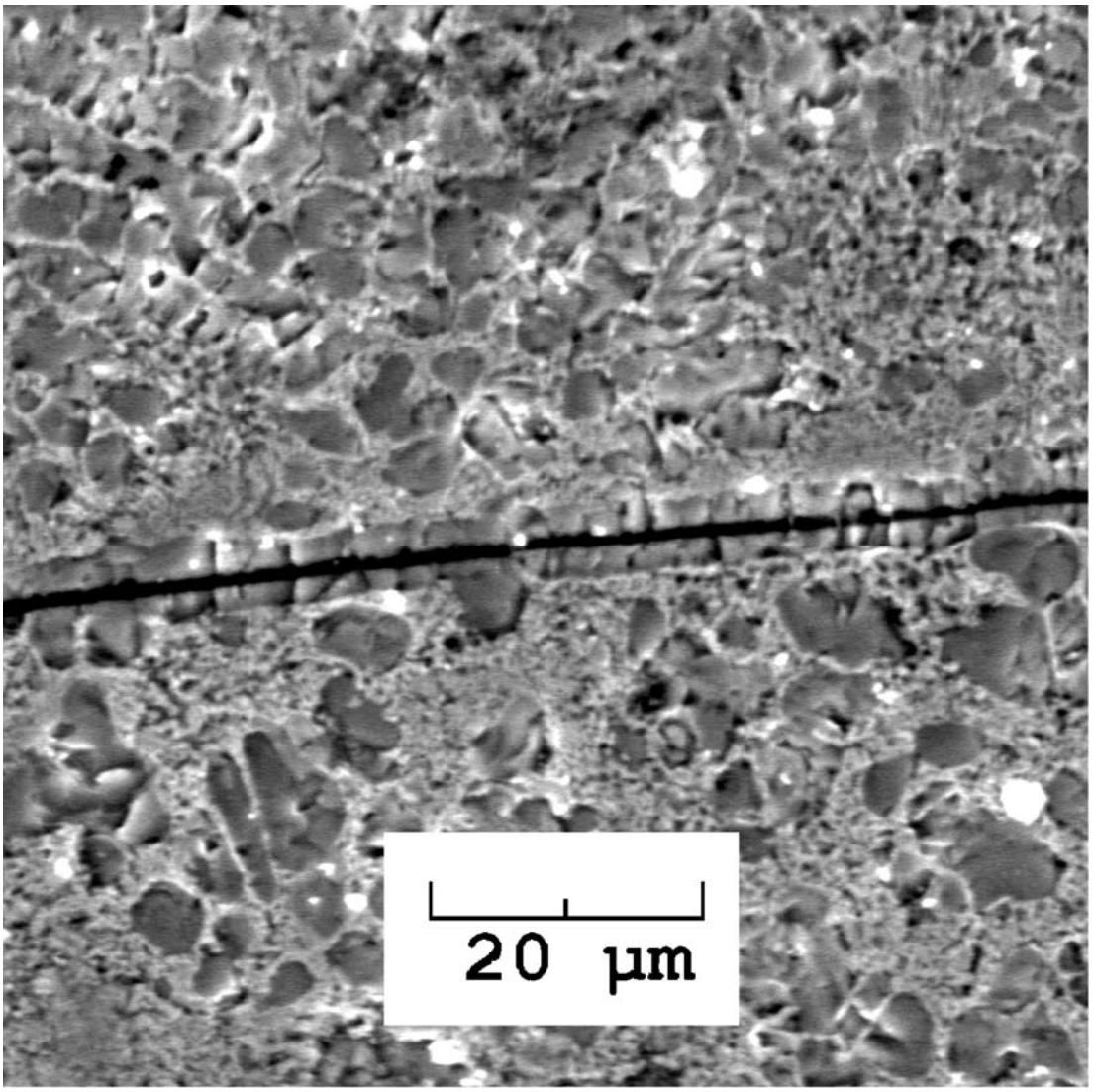

Figure 4.2.1(c) An SEM micrograph of the interface between adjacent layers of cast carbide material.

4.2.2 Microindentation Hardness

The microhardness obtained was in the range 1150 to 1500 VHN, very similar to that measured for compact powder bed trials. The scanning electron micrograph shown in Figure 4.2.1(a) shows the microhardness indentations and their hardness values. Some indentations interfered with the cracks present in the material and could have affected the hardness values. Overall, the microhardness values range measured is consistent with that measured on compact powder bed trials and also with the data published by Erwin Rudy [7].

4.3 Axis-symmetric Laser Powder Deposition

Section 4.3.1 shows the results of trials done with laser powder deposition of molybdenum and tantalum on graphite mandrels. Section 4.3.2 presents results of three-dimensional W-Ti-C cermelt on titanium coated graphite mandrel.

4.3.1 Trials with Mo and Ta Laser Powder Deposition

A 20 mm long molybdenum deposit was made on a 100 μ molybdenum coated graphite mandrel and is shown in Figure 4.3.1(a). Figure 4.3.1(b) demonstrates a 30 mm long tantalum deposit made on a tantalum coated graphite mandrel. This part presents a fully melted microstructure except for a narrow region near to the interface with the graphite mandrel as shown in Figure 4.3.1(c). The tantalum deposit thus produced presents no cracks. The trial results show that the axis-symmetric laser powder deposition apparatus is qualified to perform laser powder deposition to make W-TiC cermelt components on graphite mandrels.

Figure 4.3.1(a) A 20 mm long molybdenum cylinder made on a molybdenum coated graphite mandrel.

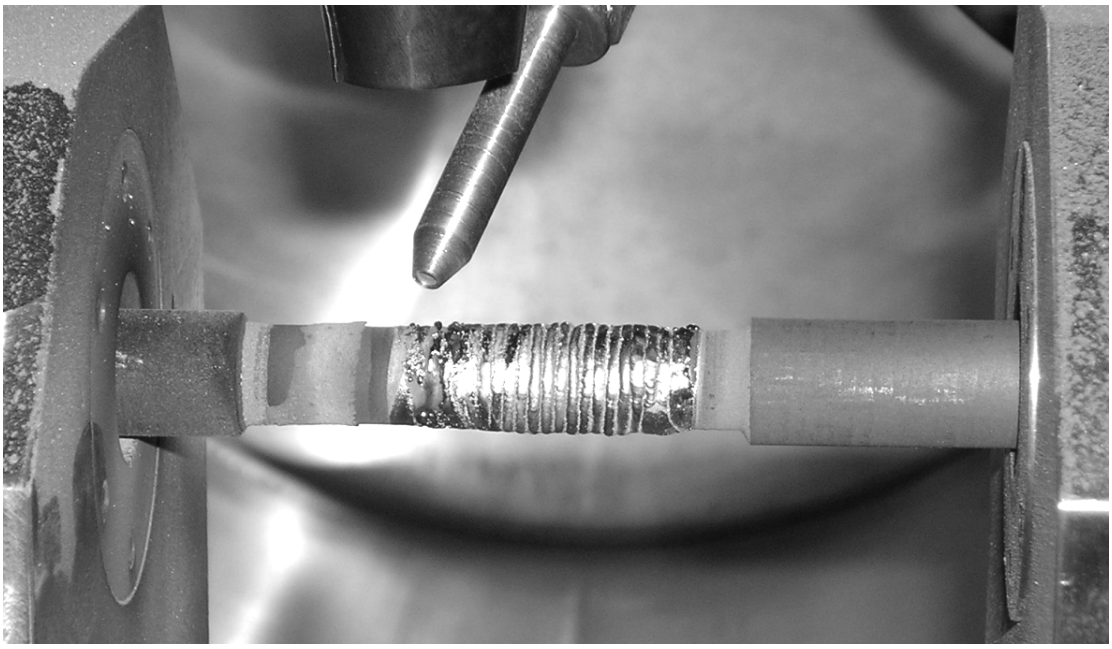

Figure 4.3.1(b) A 30 mm long tantalum cylinder made using -80/+270 mesh tantalum powders on a tantalum coated graphite mandrel.

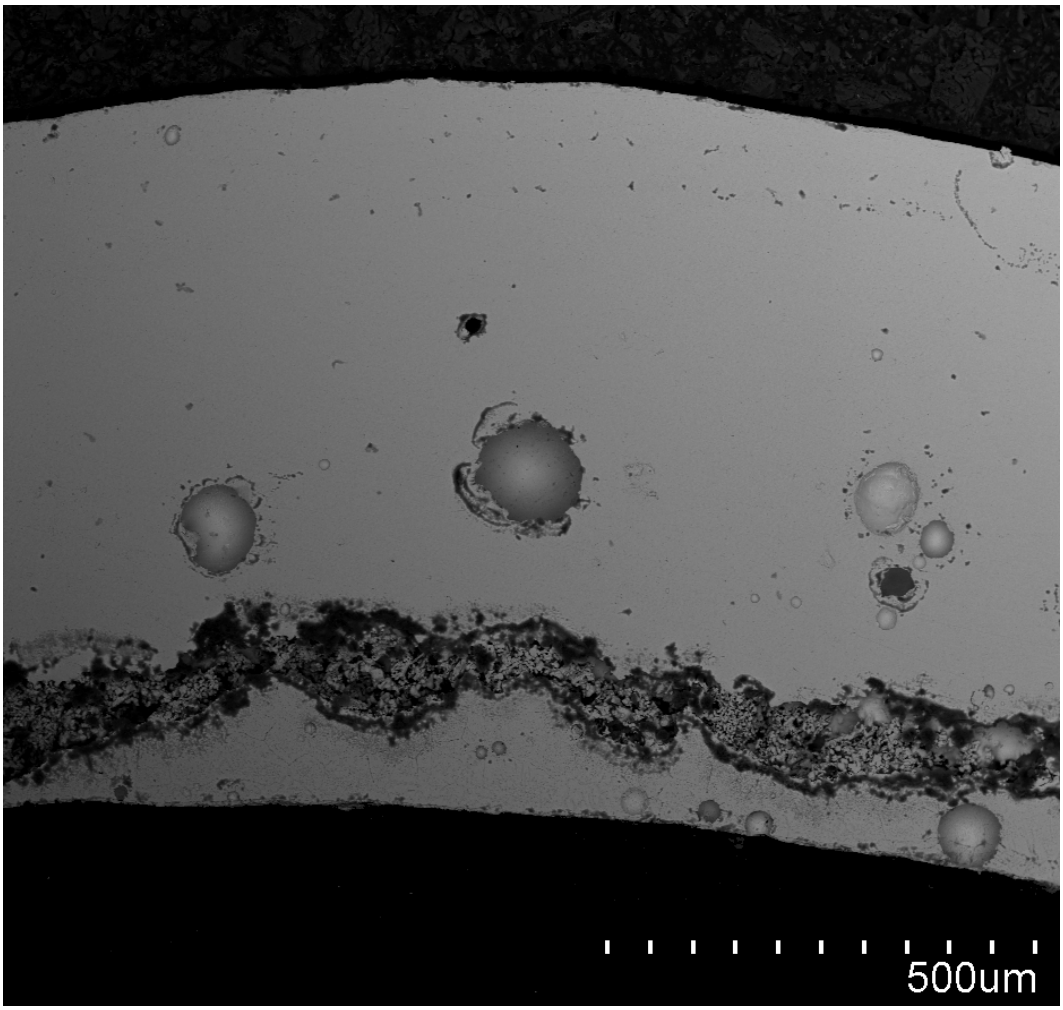

Figure 4.3.1(c) An SEM cross-sectional view of the microstructure of the laser powder deposited tantalum cylinder on a tantalum coated graphite mandrel.

4.3.2 W-TiC Laser Powder Deposition on Graphite Mandrels

Initial trial was done at 1200W laser beam power and a 30 mm long cylinder was made on a titanium coated graphite mandrel as shown in Figure 4.3.2(a). This part presents a sintered type microstructure formed by partial melting of the feedstock powders during laser processing, as seen in Figure 4.3.2(b). The laser beam power was raised to completely fuse the feedstock powders. At 1400 W, most of the feedstock powders melt under the action of the laser beam, as seen in Figure 4.3.2(c). Here, only the region closest to the graphite mandrel surface presents unmelted feedstock particles. The fully melted region presents a microstructure of fine (Ti,W)C surrounded by the (W,Ti) + (Ti,W)C eutectic, as observed previously in reference [8]. One also notes the presence of cracks within the fully melted material, which do not appear to propagate into the partially melted region. Parts produced at 1400 W were more brittle than those produced at 1200 W. A fully melted but brittle microstructure was obtained when the feedstock powders were laser processed at 1600 W as shown in Figure 4.3.2(d). The obtained microstructure presents various defects at the interface where consecutive laser passes overlap.

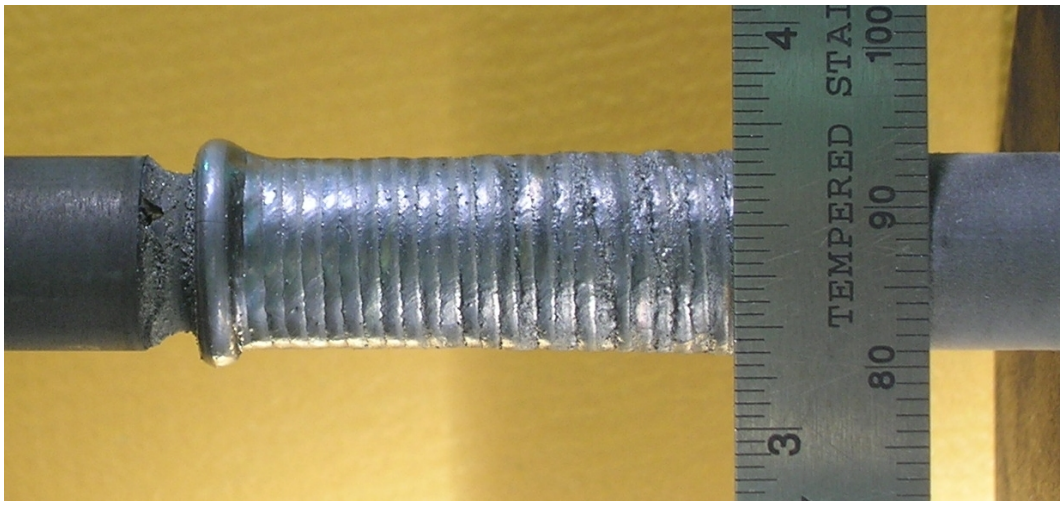

Figure 4.3.2(a) A 30 mm long cylinder produced using a ¾ (32-38 mm W) + ¼ (75-106 mm APS W-coated TiC) powder mix.

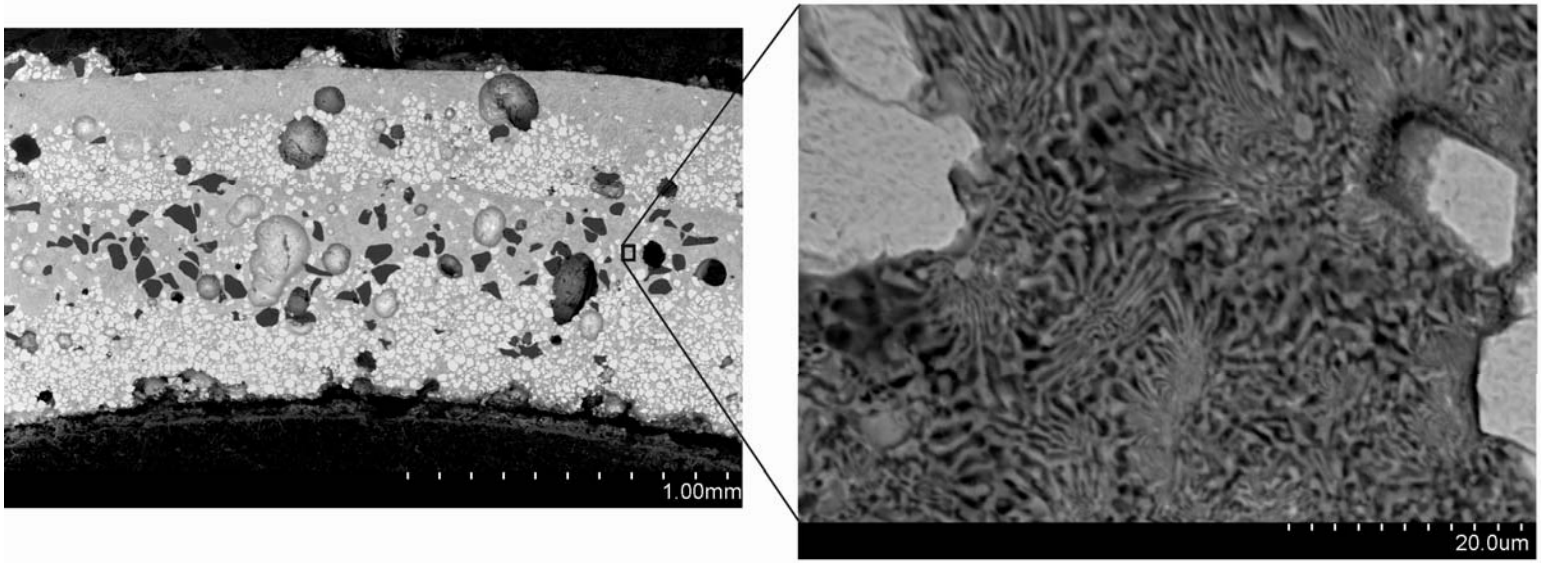

Figure 4.3.2(b) An SEM view of the microstructure of the laser powder deposited material shown in Figure 4.3.1(a). One the left, one can clearly observe unmelted feedstock particles. On the right, one can observe the fine (W,Ti) – (Ti,W)C eutectic formed between the unmelted particles.

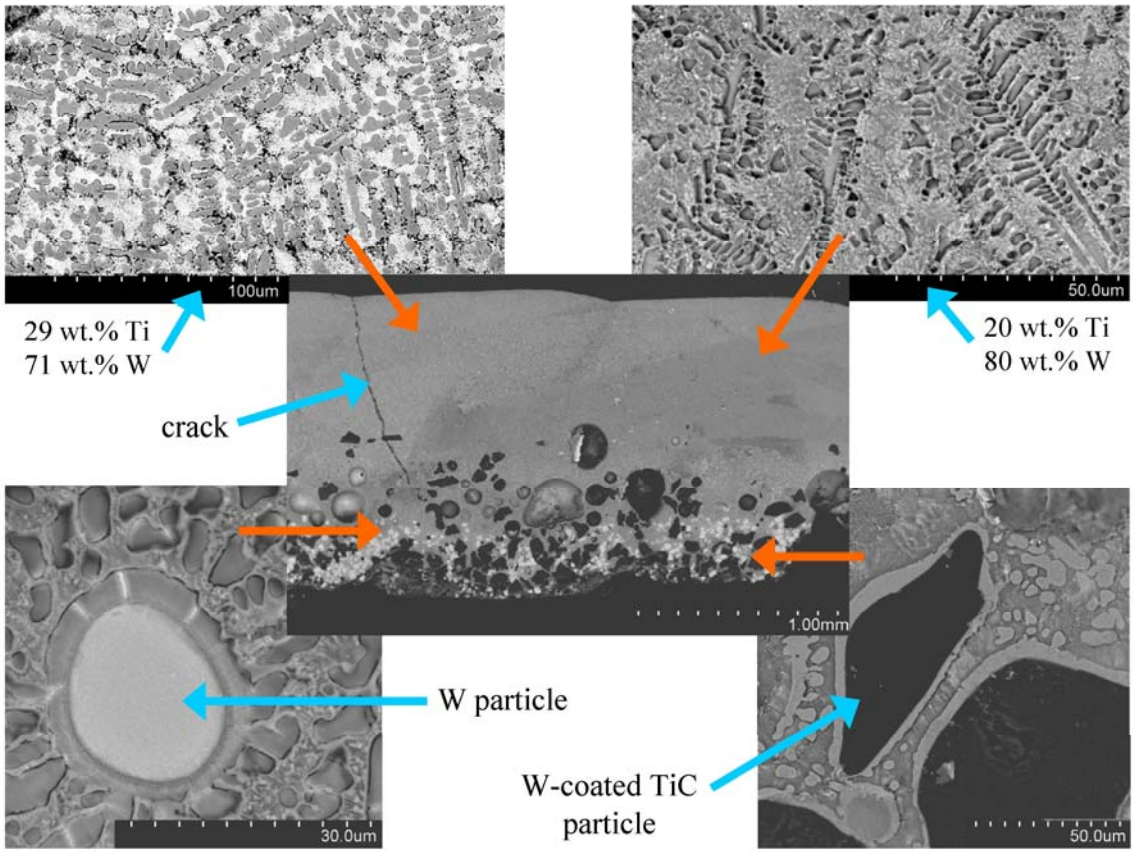

Figure 4.3.2(c) An SEM view of the microstructure of the material (APS+W) deposited at 1400 W.

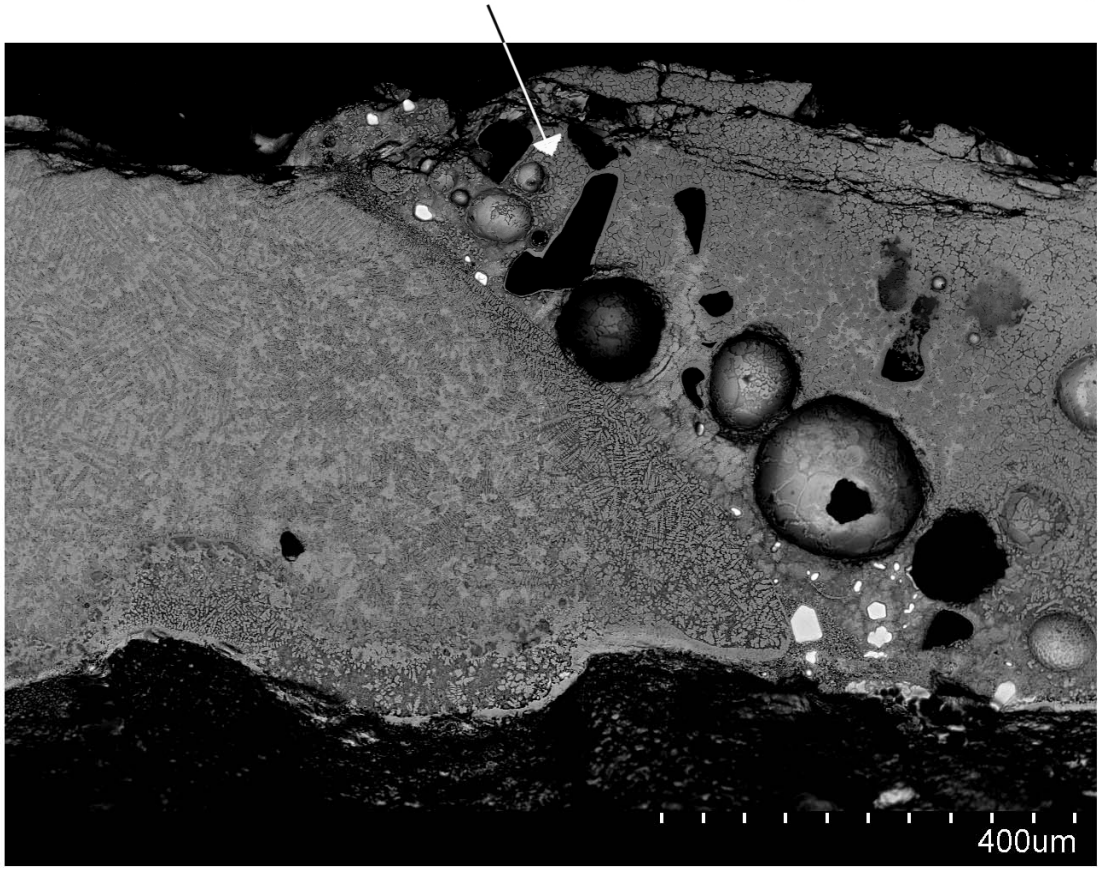

Figure 4.3.2(d) An SEM view of the microstructure of the material deposited at 1600 W.

4.3.3 W-TiC Cermelt Deposits on Graphite Mandrels.

Laser powder deposition of W-TiC results in segregation of tungsten and tungsten coated titanium carbide (APS) powders inside the hopper. The segregation happens because of a large difference in densities of tungsten (~18 g/cc) and APS powders (~6.3 g/cc). As a result of this segregation, the chemistry of the blown powders changes, which after laser melting and solidification gives different microstructures. The SEM micrograph of W-TiC deposit in Figure 4.3.2(c) shows two regions of different microstructures and chemistries. There are two ways to defeat this problem: (i) use different hoppers for powders of different densities, and (ii) laser process a thick barrier coating itself without blowing any powder. In fact, the second way changes the concept and the processing no longer remains laser powder deposition. In the present study, we processed thick barrier coatings based on W-TiC eutectic composition straight on graphite mandrels. In the first attempt, a 0.6 mm thick induction hardened W-TiC barrier coating was laser processed at 1500 W to produce a 30 mm long and 300 μ thick cylindrical deposit on a graphite mandrel as shown in Figure 4.3.3(a). The deposit thus produced was fully melted and resolidified as shown in Figure 4.3.3(b). The microhardness of the deposit was found to be in the range 1100 – 1300 VHN, which corroborates with the results obtained earlier (sections 4.1.2 and 4.2.2). In the second attempt, a 1.3 mm thick induction hardened W-TiC barrier coating was laser processed at 1600 W to produce a 30 mm long and 1 mm thick cylindrical deposit on a graphite mandrel as shown in Figure 4.3.3(c). Figure 4.3.3(d) shows the W-TiC cylindrical deposit that was obtained by machining out the graphite mandrel. This figure also justifies the fact that graphite mandrels can be machined out to obtain the deposits made on them

using any technique. Also, graphite being a good conductor of electricity enables induction heating as well.

Figure 4.3.3(a) A 30 mm long and 0.3 mm thick W-TiC deposit made on a graphite mandrel by laser processing a 0.6 mm W-TiC barrier coating induction hardened for 5 hours. Laser processing was done at 1500 W.

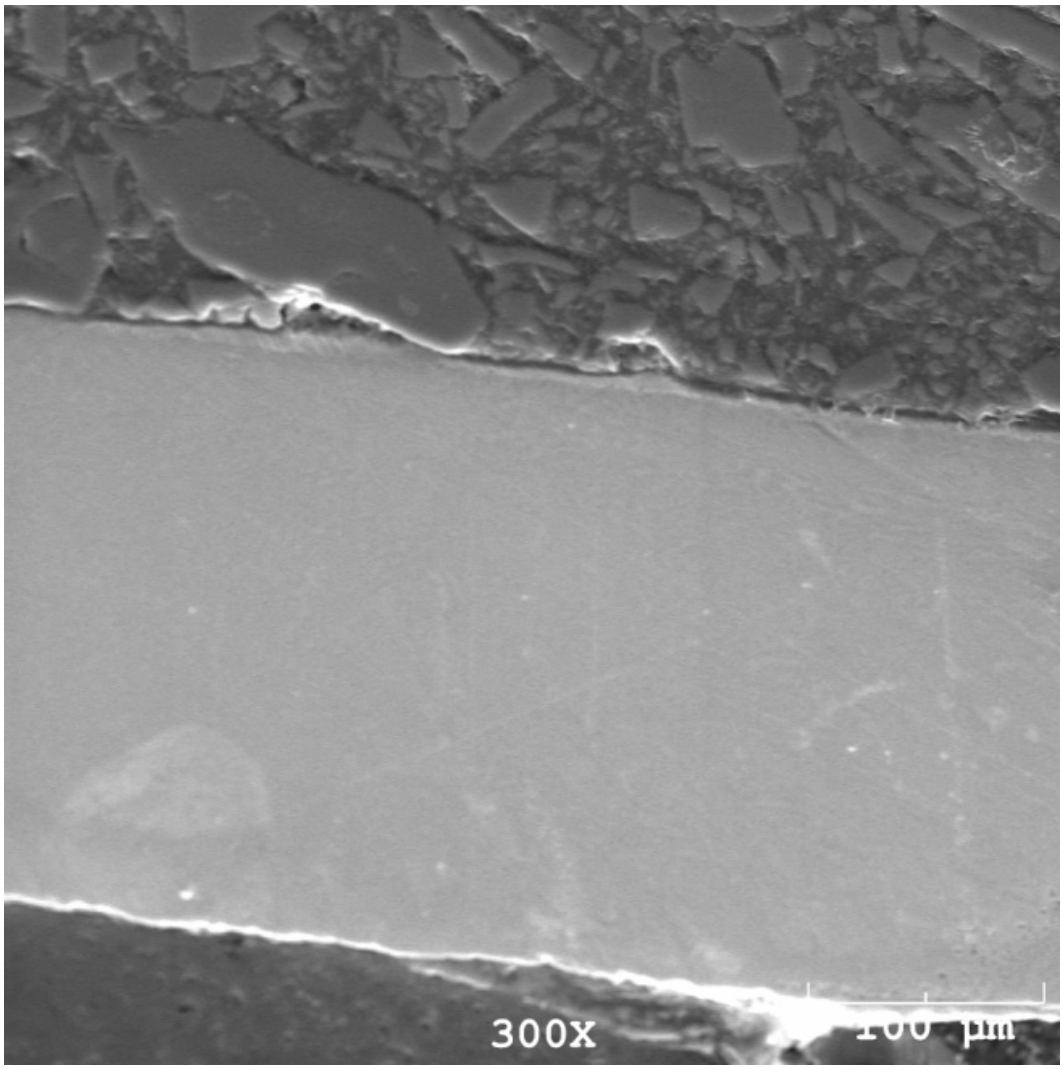

Figure 4.3.3(b) An SEM micrograph of the deposit shown in Figure 4.3.3(a). It shows that the deposit is completely melted and resolidified. This deposit does not have any cracks.

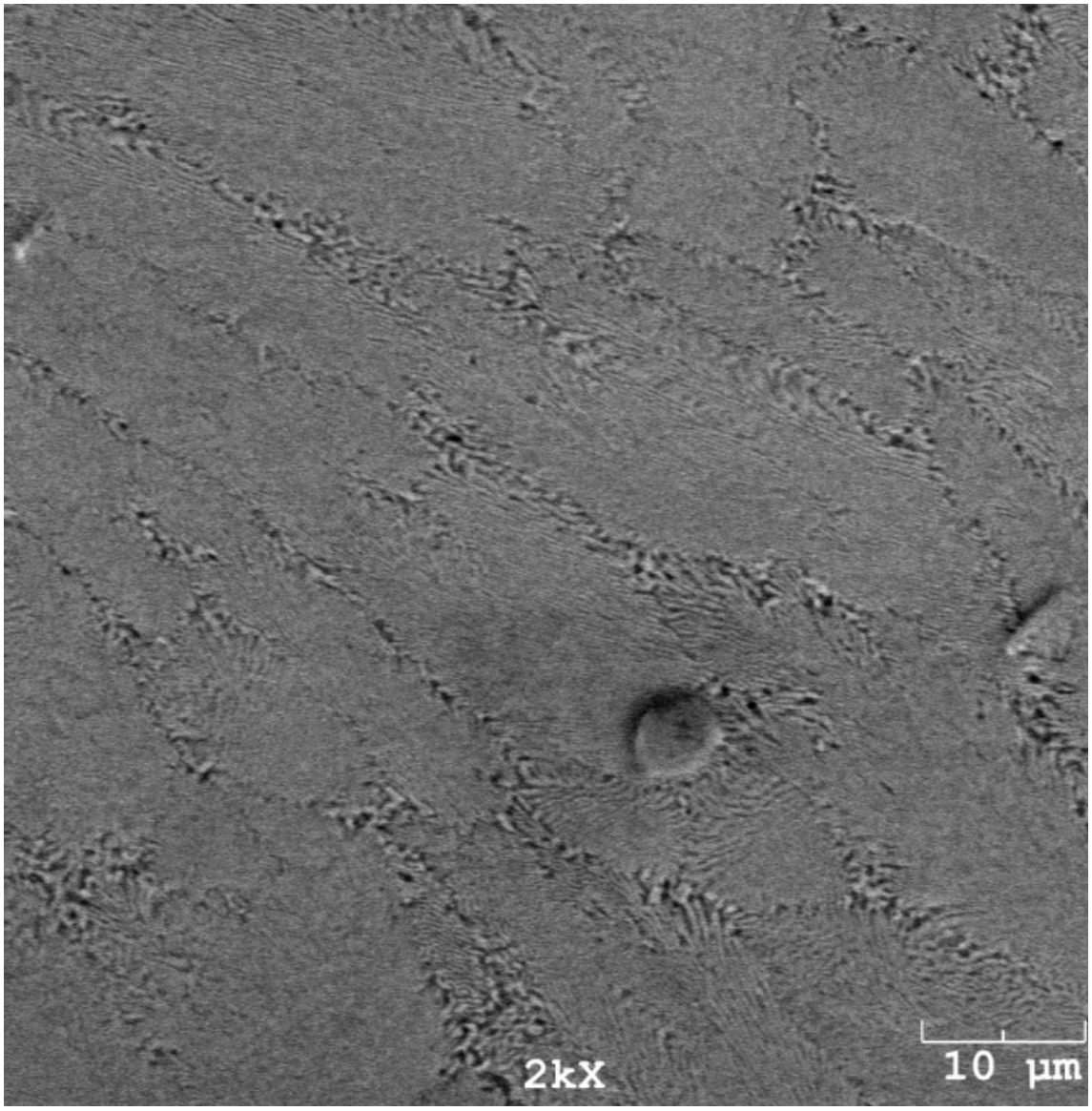

Figure 4.3.3(c) A high magnification SEM micrograph of the deposit shown in Figure 4.3.3(a) and (b). It shows the (W,Ti) + (Ti,W)C eutectic type microstructure of the deposit.

Figure 4.3.3(d) A 30 mm long and 1 mm thick W-TiC cylindrical deposit made on a graphite mandrel by laser processing a 1.3 mm thick W-TiC barrier coating at 1600 W.

4.4 W-Ti-C Cermelt Coatings on Graphite Plates

Section 4.4.1 presents the results and discussion on W-Ti-C coatings deposited straight on graphite substrates using LISI^{TM} process. Section 4.4.2 presents results and discussion on W-Ti-C cermelt coatings deposited on titanium coated graphite substrates. In this case, the graphite substrate was first coated with titanium using LISI^{TM} process, which modifies the graphite substrate surface, and then W-Ti-C coating was deposited on titanium coated graphite. The titanium intermediate barrier coating was deposited on graphite to modify the surface and enhance the bonding characteristics as explained in section 3.1. The starting material used in both the cases was nanoencapsulated tungsten coated titanium carbide (APS) powders.

4.4.1 W-Ti-C Cermelt Coating on Graphite

W-Ti-C cermelt coating on graphite was characterized with scanning electron micrographs and Vickers hardness. SEM analysis was done on a Hitachi S-3400 N variable pressure scanning electron microscope equipped with OXFORD INCA version 4.06 energy dispersive x-ray spectrometer.

4.4.1.1 SEM and EDS Analysis

The cross-sectional samples of W-Ti-C cermelt coating on graphite were mounted on bakelite, ground and polished to grit size 2400, cloth polished with diamond suspension of 1 micron, and etched with modified Murakami's solution for 30 seconds to reveal the microstructure. The microstructure of the coating is shown in Figures 4.4.1.1(a) and 4.4.1.1(b).

The elemental composition of the cermelt coating was checked with energy dispersive x-ray spectrometer and was found to contain 54 wt.% titanium and 46 wt.% tungsten. The analysis showed that the chemical composition of the coating is in the hypereutectic region instead of near-eutectic region, which gives the indication that there was excess titanium in the precursor material. Moreover, the microstructure of the cermelt did not match with that of the previous work done by Hofmeister et al. [8]. This compositional shift from near-eutectic region to hypereutectic region can be attributed to the problems associated with coating method for coating titanium carbide with tungsten. The lack of tungsten around titanium carbide particle makes it richer in titanium carbide and shifts the composition toward hypereutectic region; refer Figure 2.2(a).

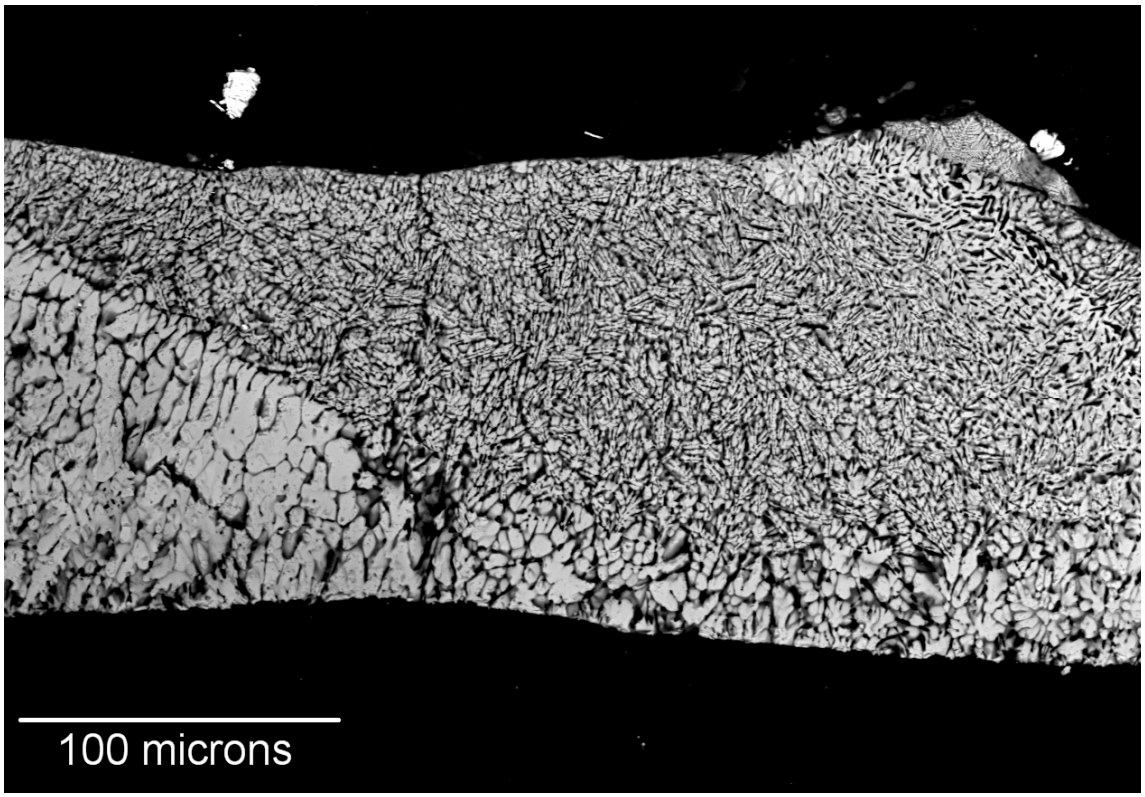

Figure 4.4.1.1(a). An SEM micrograph of W-Ti-C coating on graphite taken at 350X magnification.

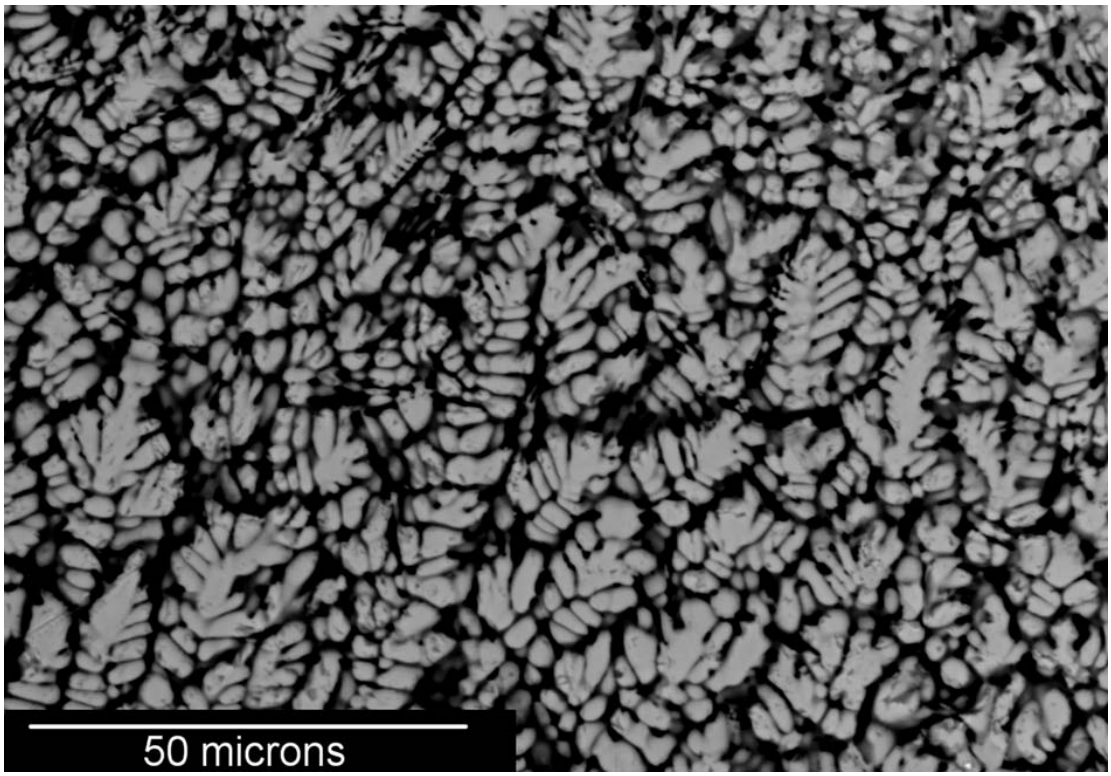

Figure 4.4.1.1(b). A high resolution SEM micrograph of W-Ti-C coating on graphite taken at 1000X magnification.

4.4.1.2 Microindentation Hardness

The indentation marks were very small (~5 microns) and very difficult to read under the microscope due to insufficient contrast between the indentation marks and the microconstituent phases, which may present some errors in hardness calculation. However, the hardness of the cermelt coating was found to be in the range 1500 to 3000 VHN with an average of 2500 VHN. The big variation in the hardness can be attributed to the presence of various phases in the coating and their composition. The high hardness values (>2200 VHN) give the indication that the cermelt coating consisted of a large volume of carbide phases.

4.4.2 W-Ti-C Cermelt Coating on Titanium Coated Graphite

Early work on protective coatings for graphite reported wetting-ability of the coating material as the major shortcoming that reduces their protective power. It was also reported that a small addition of titanium to the coating material markedly improves the wetting tendency by decreasing the wetting angle and increasing the work of adhesion [46]. In the present study, a thin titanium layer was deposited on graphite prior to the deposition of cermelt coating. Instruments used for characterization are mentioned in section 4.4.1.

4.4.2.1 SEM and EDS Analysis

Figure 4.4.2.1(a) shows two different titanium layers deposited on graphite substrate at different optimized laser power levels as shown in Table 3.5.2(c). Figure 4.4.2.1(b) shows trial (small patches in the left) and final (big patches in the right) W-Ti-

C coatings on titanium coated graphite. The screening and optimized laser processing parameters are shown in Tables 3.5.2(e) and 3.5.2(f). The SEM micrographs of W-Ti-C coating are shown in Figures 4.4.2.1(c) and 4.4.2.1(d).

The SEM micrograph of W-Ti-C coating on titanium coated graphite shows the presence of partially melted tungsten (grey particles), titanium carbide of the APS powder (dark particles), and W-Ti-C eutectic alloy. The presence of unmelted particles suggests that the W-Ti-C precursor requires higher laser power for complete melting and forming W-Ti-C eutectic alloy. The elemental analysis of the coating done using energy dispersive x-ray spectrometry was found to be 88.5 wt.% tungsten and 11.5 wt.% titanium. It indicates that the chemical composition of the coating is in the near-eutectic region of W-Ti-C ternary system.

4.4.2.2 Microindentation Hardness

The microindentation hardness testing of the W-Ti-C coating on graphite showed a large variation in hardness values ranging from 700 VHN to 1600 VHN. This large variation in hardness values can be attributed to the presence of tungsten, titanium carbide, and W-Ti-C eutectic alloy.

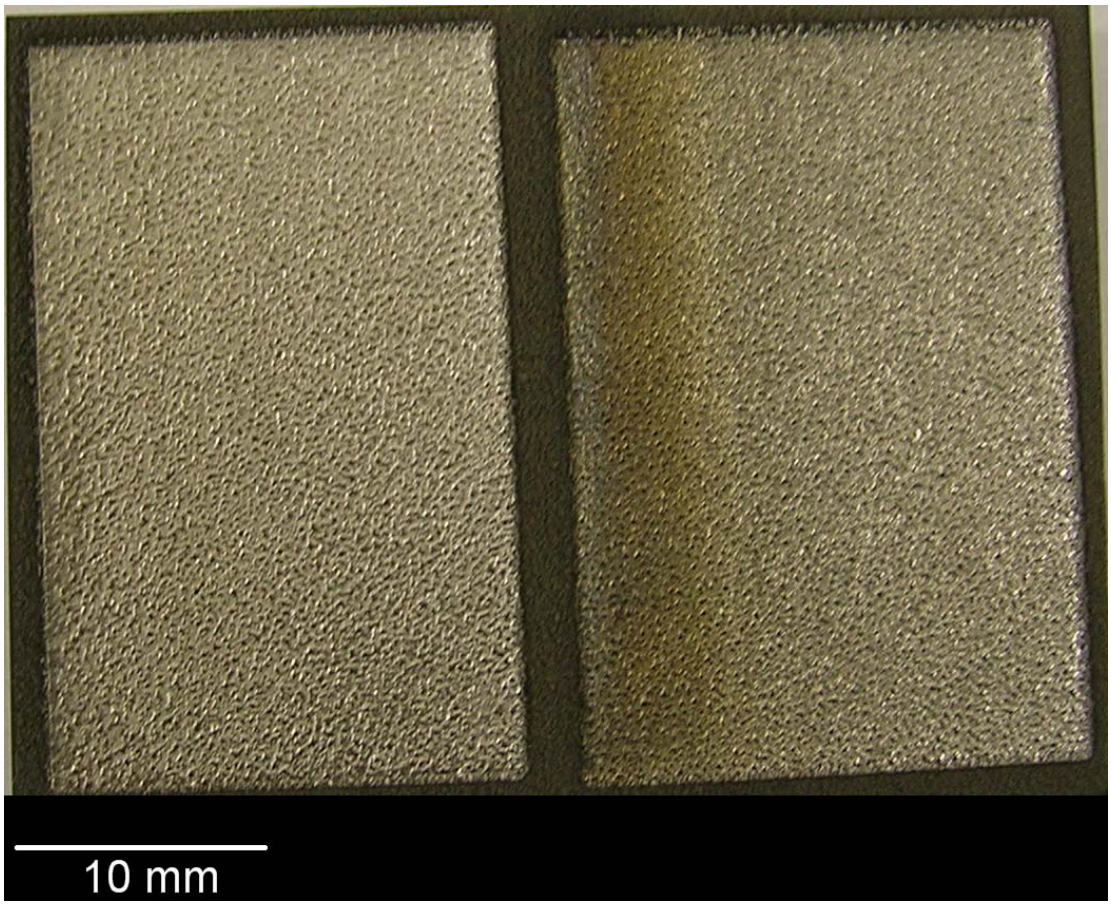

Figure 4.4.2.1(a). Titanium coated graphite substrate showing two coatings made at different laser power levels.

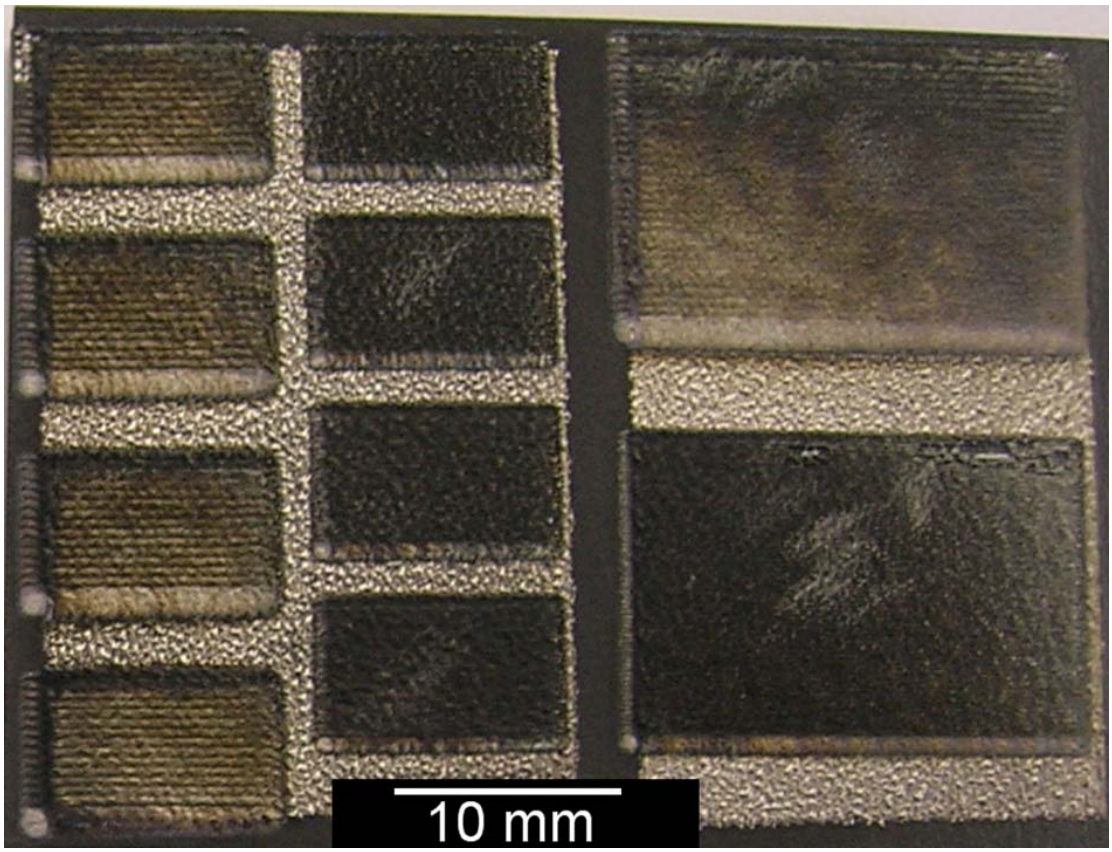

Figure 4.4.2.1(b). W-Ti-C cermelt coating on titanium coated graphite substrate. Small patches were initial trials and big patches were final coatings.

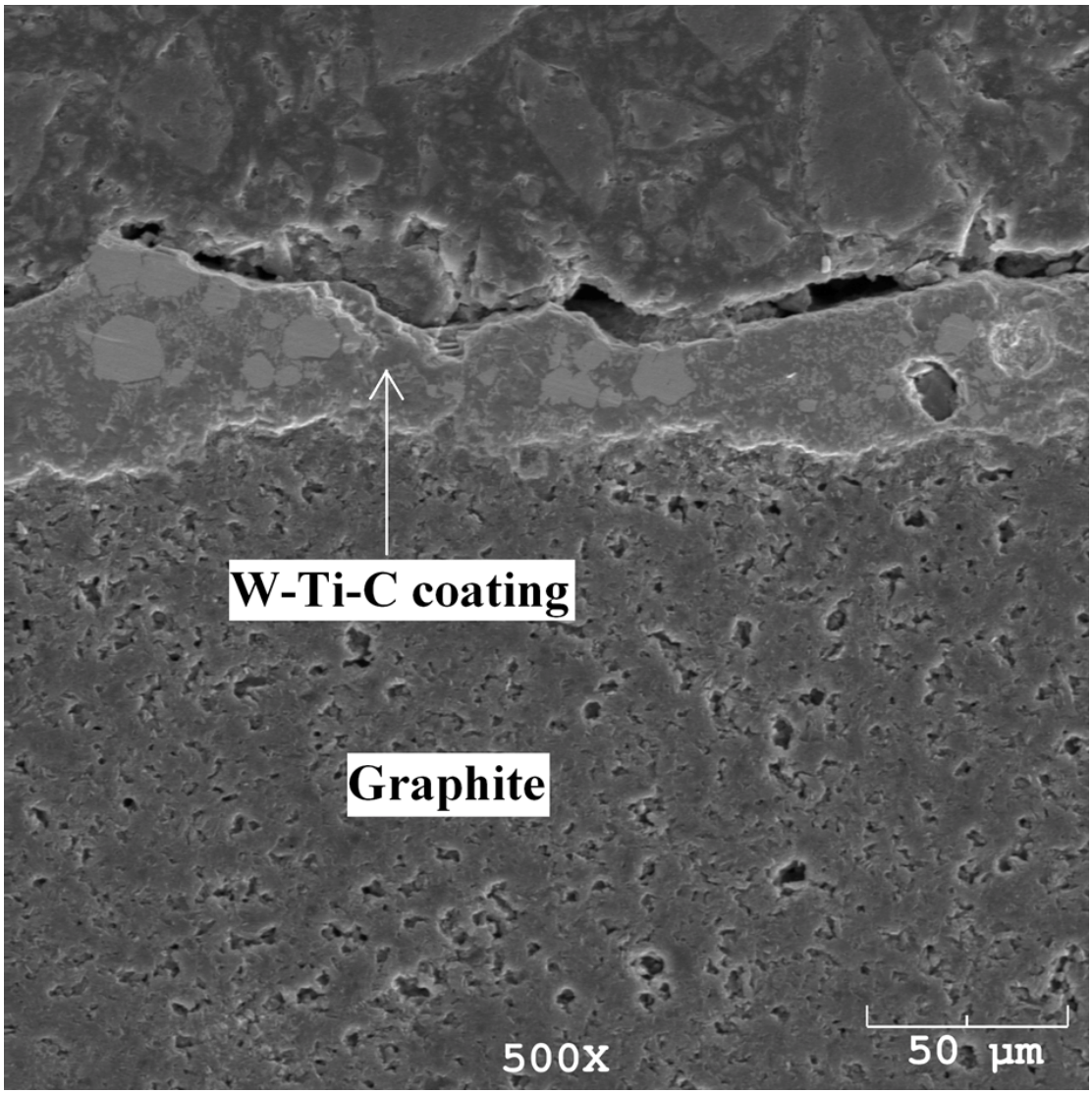

Figure 4.4.2.1(c). An SEM micrograph of W-Ti-C coating on titanium coated graphite at 500X magnification.

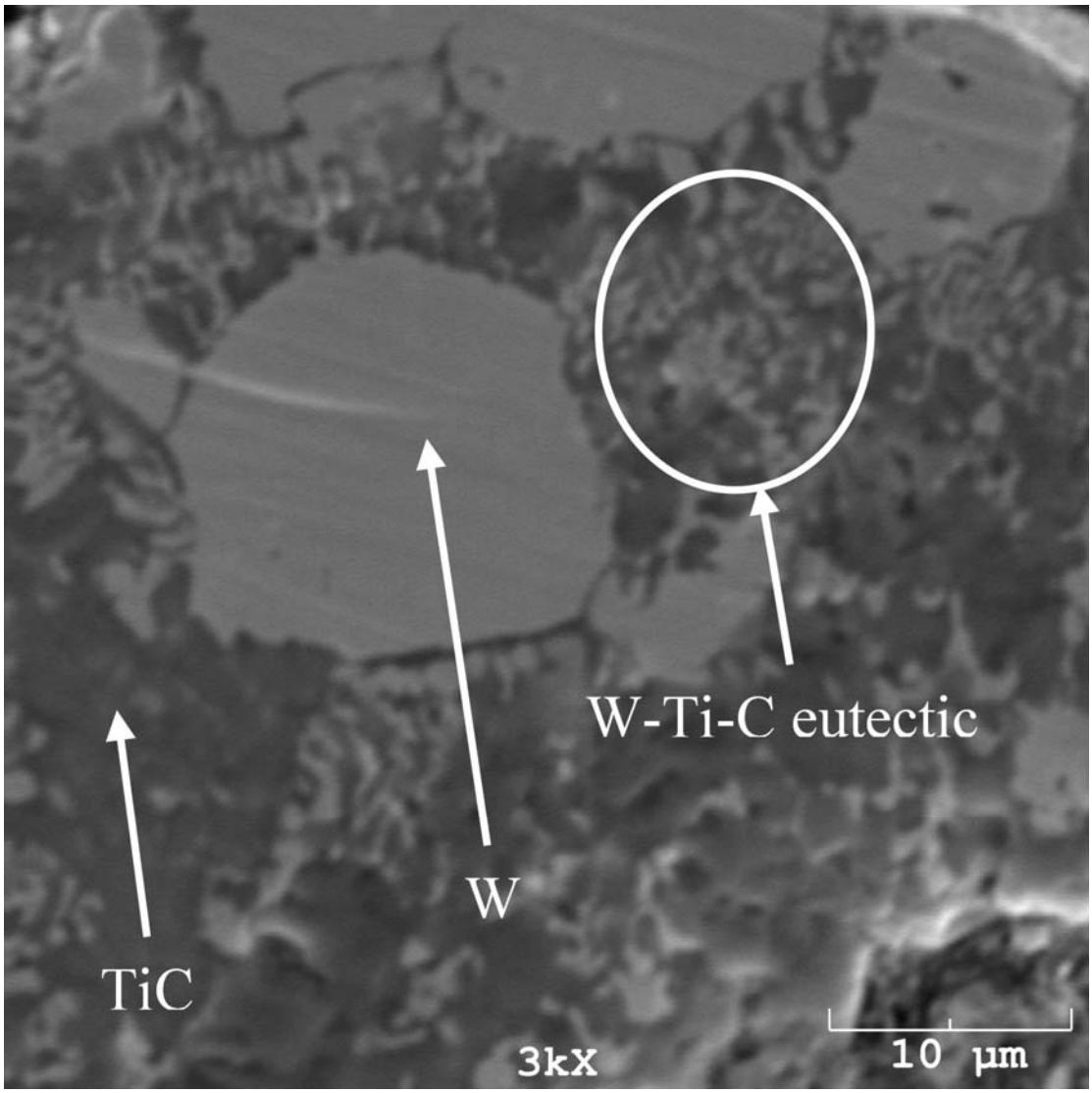

Figure 4.4.2.1(d). A high resolution SEM micrograph of W-Ti-C coating on titanium coated graphite at 3000X magnification.

4.5 W-Ti-C Cermelt Coatings on Steel

As described in section 3.6 the problems associated with direct laser deposition of W-Ti-C cermelt coating on steel, a strategy of multiple compatible layers on steel was adopted. First, a chromium layer was deposited on AISI 4130 steel using Cr-CrB_2 eutectic composition and then a molybdenum coating on chromium coated steel using Mo-MoB eutectic composition. This strategy leads to the development of a new surface, an alloy of molybdenum, on which a W-Ti-C cermelt coating can be deposited. A detailed characterization of these coatings is presented in reference [56]. However, this section presents some selected results of molybdenum-on-chromium dual coating deposited on AISI 4130 alloy steel.

Cross-section samples of Cr layer and Mo coating were polished and etched with 2% nital solution and Murakami's reagent, respectively. Figure 4.5.1(a) shows the SEM micrograph of Cr layer taken at 300X magnification and it shows that the layer thickness is around 125-150 microns. It also shows the presence of a narrow heat affected zone (white cloudy region) which stretches about 100 microns underneath the Cr layer. The EDS analysis shows that the amount of Fe (dilution) in the Cr layer is around 10-20 wt.%. It was noticed that the Cr layers with Fe content less than 10 wt.% chipped off from some locations whereas those with Fe content more than 10 wt.% were very continuous and homogenous all through the coating. This indicates that the Cr layer is brittle and it requires a minimum of 10 wt.% Fe to keep the coating intact. A homogenous and continuous Cr layer is of paramount importance even if it contains 10-20 wt.% Fe content as dilution because of the subsequent processing of Mo* on Cr coated steel.

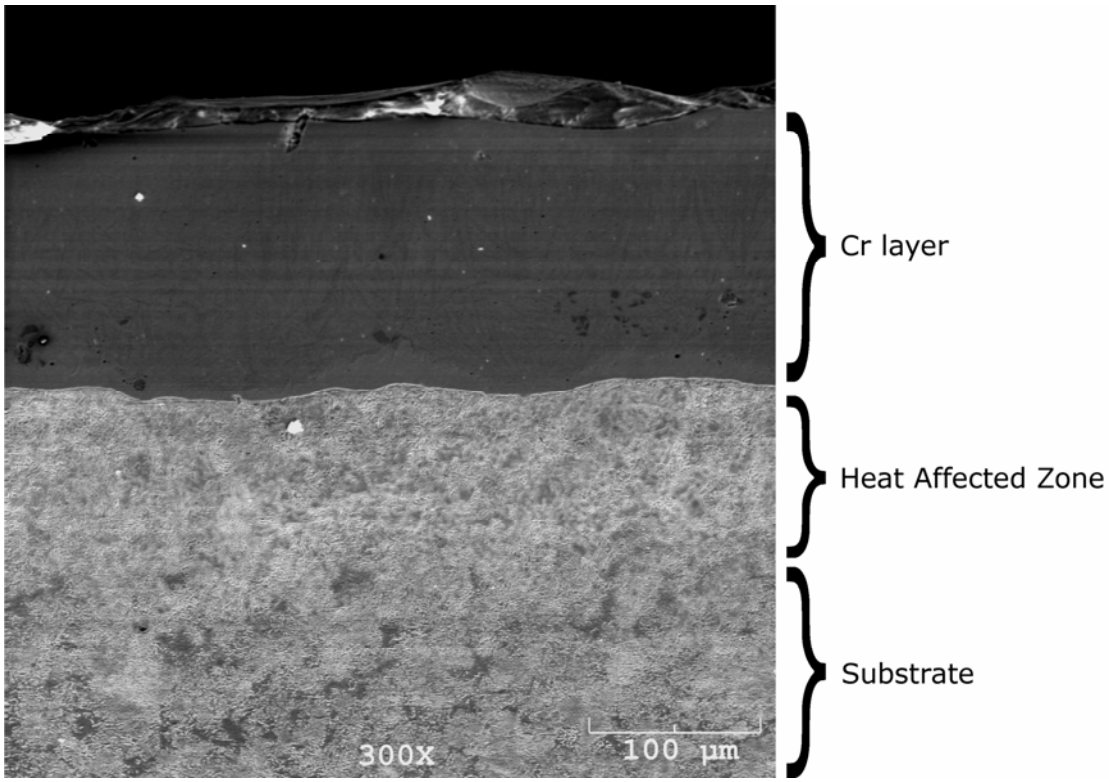

Figure 4.5.1(a). An SEM micrograph of the cross-section of chromium layer deposited on AISI 4130 steel.

While laser processing Mo coating on Cr coated steel, heat travels through the Mo* precursor layer and affects the Cr layer, the heat affected zone (HAZ), and the steel substrate. Thus, the thickness and composition of Cr layer alter after processing Mo* on Cr coated steel. This affected Cr layer is termed as reprocessed-Cr layer from this point onwards. The SEM micrograph, shown in Figure 4.5.1(b), shows that the Mo coating is around 100-125 microns thick whereas the reprocessed-Cr layer underneath is 100-125 microns thick as well. Mo* precursor alloys with the Cr layer and forms the Mo coating. EDS analysis showed that the Mo coating is a solid solution of Mo, Cr, Fe, and B, which contains 20-25 wt.% Cr and 6-8 wt.% Fe. The molybdenum coating produced by this method does not have high level of dilution with iron and is thus a suitable substrate for the subsequent deposition of high-melting-point alloy like W-Ti-C cermelt.

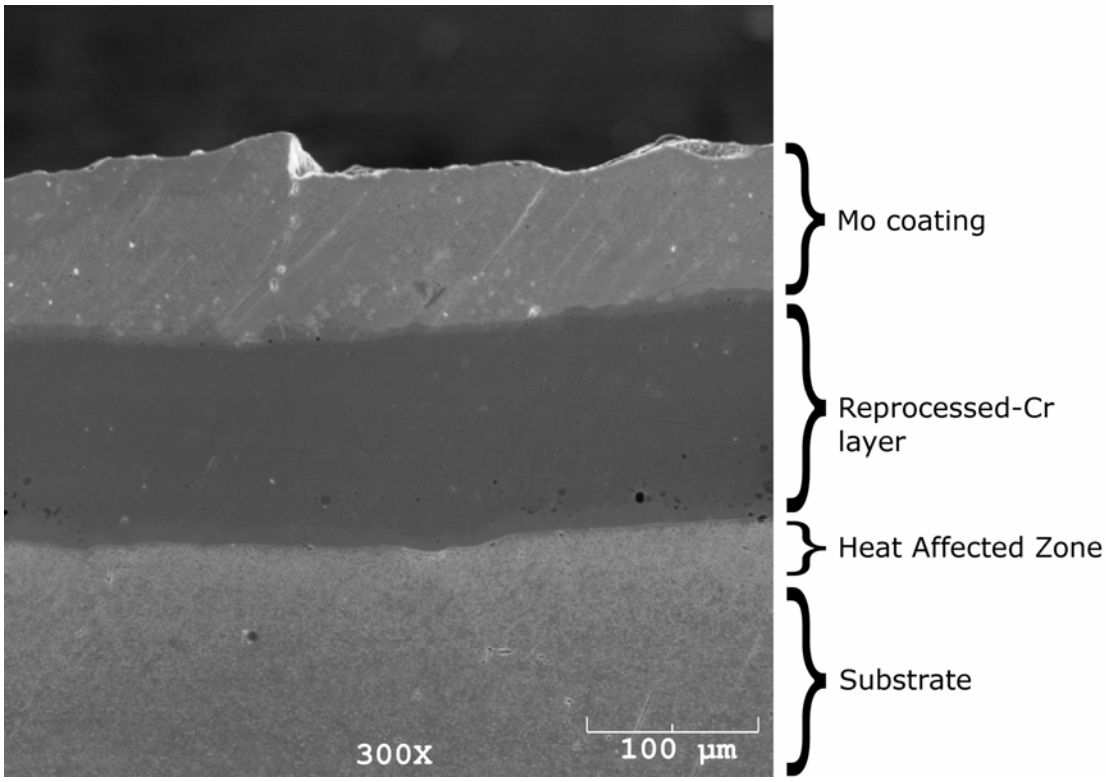

Figure 4.5.1(b). An SEM micrograph of the cross-section of molybdenum coating on chromium coated AISI 4130 steel.

CHAPTER 5

CONCLUSIONS

W-Ti-C based cermelt has been fabricated into near-net shape components using two different techniques: tower nozzle solid freeform fabrication system and axis-symmetric laser powder deposition system. W-Ti-C based cermelt coatings have been deposited on graphite plates and graphite mandrels. Also, a method for depositing W-Ti-C cermelt coating on steel has been investigated.

The strategy of making barrier coatings on graphite and titanium carbide has been found to be effective in mitigating the problems of carbon evaporation. Graphite plates have been coated with titanium through LISI^{TM} process, whereas graphite mandrels have been induction hardened after spraying feedstock powders. Titanium carbide powders have been coated with tungsten by a fluidized bed chemical vapor deposition technique.

5.1 Powder Compact Trials: W-Ti-C Cermelt

Initial trials on powder compact beds are very useful in finding approximate laser processing conditions for solid freeform fabrication and surface coatings of cermelts. Trials on powder compact beds made with W-TiC powder mix show that W-Ti-C cermelt can be made by laser processing a mixture of tungsten and titanium carbide powders, which is an alternative to using tungsten, titanium, and graphite/nano-carbon powders. The microstructure consisted of (Ti,W)C dendrites in a matrix of (W,Ti) metal phase. The

microhardness of W-Ti-C cermelt processed on powder bed compacts was found to be in the range 1100-1300 VHN, which corroborates with the results of W-Ti-C cast carbides processed through conventional arc melting process reported by Erwin Rudy.

5.2 Tower Nozzle Solid Freeform Fabrication

A novel tower nozzle solid freeform fabrication system has been developed to produce near-net shape components. The potential to form refractory metal (W,Ti) – refractory carbide (Ti,W)C alloys into near-net shape components using this system was demonstrated. The simple three-dimensional thin wall structures formed by laser melting successive layers of a 85.55 wt% W – 14.45 wt% TiC powder mix present a hard microstructure of finely distributed (Ti,W)C dendrites surrounded by a (W,Ti) + (Ti,W)C eutectic.

5.3 Axis-symmetric Laser Powder Deposition

A laser powder deposition technique suitable for near-net shape fabrication of axis-symmetric components on graphite mandrels has been successfully demonstrated. The technique is particularly suited for the deposition of refractory materials and fabrication of rocket nozzles and thrust-combustion chambers. This deposition technique was successfully applied to the deposition of molybdenum and tantalum. The potential to form cylindrical shape (W,Ti) – (Ti,W)C cermelts by laser powder depositing a mix of tungsten and nanoencapsulated tungsten coated titanium carbide powders has also been demonstrated. However, the produced materials present poor toughness. The formed cermelts present a microstructure of finely distributed (Ti,W)C dendrites surrounded by a

(W,Ti) + (Ti,W)C eutectic. The cermelts also present some inhomogeneities, especially at the interface where consecutive laser passes overlap, and cracks that render the cermelts more brittle than the materials formed at lower laser power levels, which exhibit a sintered type microstructure. In addition to these inhomogeneities and poor toughness, the cermelt thus produced revealed non-homogenous microstructure. This inhomogeneity in the microstructure has been attributed to the large difference in the densities of the feedstock powders, which segregates them while in the powder hopper.

The barrier coatings deposited on graphite mandrels prior to laser powder deposition revealed effective in protecting the graphite mandrels from sublimation during laser processing and provided a suitable base for laser powder deposition. The nanoencapsulated powders from Advanced Powder Solutions have been successfully melted by laser processing without excessive carbon loss.

5.4 W-Ti-C Cermelt Deposits on Graphite Mandrels

W-Ti-C cermelt deposits have been made on graphite mandrels using axis-symmetric laser powder deposition system. In this strategy, a barrier coating was made by spraying and induction hardening feedstock powders of W-TiC eutectic composition on graphite mandrels. The barrier coatings thus produced were laser processed without blowing any powder in the axis-symmetric laser powder deposition system. Fully melted and resolidified deposits of up to 1 mm thickness have been successfully made using this strategy. The deposits thus produced present no cracks and variation in microstructure. This strategy proved an improvement over W-TiC laser powder deposition. Also, the

concept of machining out graphite mandrel to obtain the deposit made on it has been successfully demonstrated.

5.5 W-Ti-C Cermelt Coatings on Graphite Plates

W-Ti-C coatings have been deposited on graphite substrate using nanoencapsulated tungsten coated titanium carbide (APS powder) as the starting material and LISI^{TM} as the fabrication process. Two different coating strategies have been used to deposit W-Ti-C coating on graphite. In the first strategy, W-Ti-C coating was deposited straight on graphite using the APS powder. The elemental analysis of this coating showed that it contains 54 wt.% titanium and 46 wt.% tungsten, which gave the indication that the APS powder was rich in titanium carbide and its composition was in the hypereutectic range. In the second strategy, a titanium barrier coating was first deposited on graphite substrate prior to the deposition of W-Ti-C coating to improve the wetting ability of W-Ti-C coating on graphite, and then a correction was made to the APS powder by adding tungsten to shift the composition closer to the eutectic point. The SEM analysis showed that this coating contains partially melted tungsten, titanium carbide of the APS powder, and W-Ti-C eutectic alloy. The elemental analysis showed that the composition of this coating was close to the eutectic point of the W-Ti-C ternary system. The hardness of this coating varied in the range 700 VHN to 1600 VHN due to the presence of tungsten, titanium carbide, and W-Ti-C eutectic alloy.

5.6 W-Ti-C Cermelt Coatings on Steel

One of the ways for depositing W-Ti-C cermelt coating on steel is the deposition of suitable intermediate layers between the steel substrate and the main cermelt coating. A possible combination of intermediate layers (in sequence) was found to be chromium and molybdenum that can be deposited on steel prior to the deposition of W-Ti-C cermelt coating. First, a chromium layer was deposited on steel and then a molybdenum coating on chromium coated steel using LISI^{TM} process. Both the coatings, chromium layer and molybdenum coating were continuous in nature and their thicknesses were 125-150 microns and 100-125 microns, respectively. Molybdenum coating was found to be an alloy of molybdenum, 20-25 wt.% chromium, 6-8 wt.% iron and boron. SEM/EDS analysis did not show the presence of any intermetallic phases in both the intermediate and main coatings. Molybdenum-on-chromium dual coating thus deposited on steel is expected to be a suitable substrate for depositing high-melting-point W-Ti-C cermelt coating.

REFERENCES

1. *Advanced Materials for Severe Service Applications*, K. Iida and A.J. McEvily, Editors. 1987, Elsevier Applied Science. p. 183-200.
2. *Superalloys* ed. E.F. Bradley. 1988: ASM International.
3. Steinitz, R., *Cermets - New High-Temperature Materials* Jet Propulsion, 1955. 25(7): p. 326-330.
4. Callister, W.D., *Fundamentals of Materials Science and Engineering*. Second Edition ed. 2005.
5. Available from: http://en.wikipedia.org/wiki/Cermet.
6. Rudy, E., *Method for Making Castable Carbonitride Alloys.* US Patent 3703368, 1972.
7. Rudy, E., *Constitution of Ternary Titanium-Tungsten-Carbon Alloys.* Journal of Less-Common Metals, 1973. 33: p. 245-273.
8. Hofmeister, W., et al., *Cast Carbide-Metal Composite Components via Laser Based Solid Freeform Fabrication*, in *26th ICALEO*. 2007, LIA: Orlando, FL USA.
9. Rajput, D., et al. *Novel Refractory Cermelt Coatings on Graphite*. in *International Conference on W, Refractory & Hardmaterials VII*. 2008. Washington D.C.
10. Costa, L., *Laser Powder Deposition: Process Simulation by Finite Element Analysis*. 2008, Universidade Tecnica de Lisboa, Portugal.

11. Bozzi, A.C. and J.D.B. Mello, *Wear Resistance and Wear Mechanisms of WC-12%Co Thermal Sprayed Coatings in Three-body Abrasion.* Wear. 233-235: p. 575-587.

12. Hickman, R., T. McKechnie, and A. Agarwal. *Net Shape Fabrication of High Temperature Materials for Rocket Engine Components*. in *37th AIAA/ASME/SAE/ASEE Joint Propulsion Conference*. 2001. Salt Lake City, Utah.

13. Liu, J. and H. Kuhn. *Manufacture of Tungsten/Copper Components by Three-dimensional Printing (3DP).* in *International Conference on Tungsten, Refractory & Hardmetals VI*. 2006. Orlando.

14. Rudy, E., *Ternary Phase Equilibria in Transition Metal-Boron-Carbon-Silicon Systems*. 1969, Aerojet-General Corporation.

15. Rudy, E., *Phase Equlibria Investigation of Binary, Ternary, and Higher Order Systems*. 1970, Aerojet-General Corporation.

16. Maiman, T.H., *Stimulated Optical Radiation in Ruby.* Nature, 1960.

17. Allmen, M.v. and A. Blatter, *Laser-Beam Interactions with Materials*. Second Edition ed, ed. U. Gonser. 1995: Springer.

18. *Lasers in Surface Engineering*. Surface Engineering Series, ed. N.B. Dahotre. Vol. Volume 1. 1998: ASM International.

19. Steen, W.M., *Laser Material Processing*. 1991: Springer-Verlag.

20. Gahan, B.C. and B. Shiner, *New High-Power Fiber Laser Enables Cutting-Edge Research*. 2004. p. 29-31.

21. Gahan, B.C., *Fiber Laser Offers Fast Track to Clean Perforations*. 2005, Gas Technology Institute. p. 17-20.

22. Wohlers, T., *Wohlers Report 2006*. 2006, Wohlers Associates: Fort Collins, Colorado, USA.

23. Dimitrov, D., K. Schreve, and N.d. Beer, *Advances in three dimensional printing - state of the art and future perspectives.* Rapid Prototyping Journal, 2006. 12(3): p. 136-147.

24. Sachs, E., et al., *Production of Injection Molding Tooling with Conformal Cooling Channels using the Three Dimensional Printing Process.* Polymer Engineering and Science, 2000. 40(5): p. 1232-1247.

25. Kruth, J.P., et al., *Lasers and materials in selective laser sintering.* Assembly Automation, 2003. 23(4): p. 357-371.

26. Cormier, D., O. Harrysson, and H. West, *Characterization of H13 steel produced via electron beam melting.* Rapid Prototyping Journal, 2004. 10(1): p. 35-41.

27. Gibbons, G.J. and R.G. Hansell, *Direct Tool Steel Injection Mould Inserts through the ARCAM EBM free-form fabrication process.* Assembly Automation, 2005. 25(4): p. 300-305.

28. Arcella, F.G. and F.H. Froes, *Producing Titanium Aerospace Components from Powder using Laser Forming.* JOM, 2000. 52(5): p. 28-30.

29. Keicher, D.M. and W.D. Miller, *LENS moves beyond RP to direct fabrication.* Metal Powder Report, 1998. 53: p. 26-28.

30. Mazumder, J., et al., *The direct metal deposition of H13 tool steel for 3D components.* JOM, 1997. 49(5): p. 55-60.

31. Sears, J.W., *Direct Laser Powder Deposition*, in *ASTM/TMS Materials Week*. 1999: Cincinnati, OH, USA. p. 213-226.

32. Xue, L. and M.U. Islam, *Free-form laser consolidation for producing metallurgically sound and functional components.* Journal of Laser Applications, 2000. 12(4): p. 160-165.

33. Vilar, R., *Laser cladding.* Journal of Laser Applications, 1999. 11(2): p. 64-79.

34. Agarwala, M., et al., *Direct selective laser sintering of metals.* Rapid Prototyping Journal, 1995. 1(1): p. 26-36.

35. Kruth, J.P., et al., *Binding mechanisms in selective laser sintering and selective laser melting.* Rapid Prototyping Journal, 2005. 11(1): p. 26-36.

36. Radstok, E., *Rapid Tooling.* Rapid Prototyping Journal, 1999. 5(4): p. 164-168.

37. Wu, X., *A review of laser fabrication of metallic engineering components and of materials.* Materials Science and Technology, 2007. 23(6): p. 631-640.

38. Fessler, J.R., et al., *Laser deposition of metals for shape deposition manufacturing*, in *Solid Freeform Fabrication Symposium*, D. Bourell, et al., Editors. 1996, University of Texas at Austin: Austin, Texas, USA. p. 117-124.

39. Gremaud, M., et al., *Laser metal forming: process fundamentals.* Surface Engineering, 1996. 12(3): p. 251-259.

40. Kreutz, E.W., et al., *Rapid prototyping with C02 laser radiation.* Applied Surface Science, 1995. 86: p. 310-316.

41. Murphy, M., C. Lee, and W.M. Steen, *Studies in rapid prototyping by laser surface cladding*, in *ICALEO*, P. Denney, I. Miyamoto, and B.L. Mordike, Editors. 1993, Laser Institute of America: Orlando, Florida, USA. p. 882-891.

42. Hu, Y.P., C.W. Chen, and K. Mukherjee, *Development of a new laser cladding process for manufacturing cutting and stamping dies.* Journal of Material Science, 1998. 33: p. 1287-1292.

43. Koch, J.L. and J. Mazumder, *Rapid prototyping by laser cladding*, in *ICALEO*, P. Denney, I. Miyamoto, and B.L. Mordike, Editors. 1993, Laser Institute of America: Orlando, Florida, USA. p. 556-565.

44. Arcella, F.G., E.J. Whitney, and D. Krantz, *Laser Forming Near Shapes in Titanium*, in *ICALEO*. 1995, Laser Institute of America. p. 178-183.

45. Chung, D.D.L., *Review Graphite.* Journal of Materials Science, 2002. 37: p. 1475-1489.

46. Dzyadikevich, Y.V. and V.E. Oliinik, *Films for Protecting Graphite Materials from Oxidation.* Powder Metallurgy and Metal Ceramics, 1996. 35(3-4): p. 150-153.

47. Malmstrom, C., R. Keen, and L. Green, *Some Mechanical Properties of Graphite at Elevated Temperatures.* Journal of Applied Physics, 1951. 22(5): p. 593-600.

48. Gorbunov, N.S., *Protective Coatings on Graphite.* Fiziko-Khimicheskaya Mekhanika Materialov, 1967. 3(6): p. 682-687.

49. J. F. Ready and D. F. Farson (editors), LIA Handbook of Laser Materials Processing - Chapter 5: Laser-Material Interactions; 1994, Laser Institute of America, Magnolia Publishing, Inc.

50. N. K. Tolochko, T. Laoui, Y. V. Khlopkov, S. E. Mozzharov, V. I. Titov and M. B. Ignatiev, "Absorptance of powder materials suitable for laser sintering", Rapid Prototyping J., 2000, vol. 6, no. 3, pp. 155-160

51. Baker, D., et al., *Net shape processing of encapsulated powders, Phase I SBIR Final Report Contract NNM05AA65C*. 2005.

52. Biswas, A., et al., *Advanced composites through nano engineering*, in *2008 World Congress on Powder Metallurgy & Particulate Materials*. 2008, MPIF: Washington DC.

53. Costa L., Rajput D., Lansford K, Yue W, and Hofmeister W., *The Tower Nozzle Solid Freeform Fabrication Technique*. Rapid Prototype Journal (under review).

54. Costa L., Hofmeister W., Rajput D., and Lansford K. *Axis-symmetric Solid Freeform Fabrication of W-TiC Cermelt Rocket Nozzles* in *2008 World Congress on Powder Metallurgy & Particulate Materials*. 2008, MPIF: Washington DC.

55. *Alloy Phase Diagrams*. ASM Handbook. Vol. 3: ASM International.

56. Rajput D., Lansford K., Costa L., and Hofmeister W., *Molybdenum-on-Chromium Dual Coating on Steel.* Surface & Coatings Technology, (doi:10.1016/j.surfcoat.2008.10.029).

APPENDICES

APPENDIX I

THE TOWER NOZZLE SOLID FREEFORM FABRICATION TECHNIQUE

(This paper is under review in Rapid Prototyping Journal)

The Tower Nozzle Solid Freeform Fabrication Technique

L. Costa, D. Rajput, K. Lansford, W. Yue, W. Hofmeister

University of Tennessee Space Institute
Center for Laser Applications
411 B. H. Goethert Parkway
Tullahoma, TN 37388

Abstract

Laser consolidation of feedstock powders into near net shape parts has been achieved using a novel powder delivery strategy. A specially designed "tower nozzle" located at the center of the processing area dispenses the feedstock powders continuously and uniformly onto the processing area where powders accumulate progressively as a flat powder bed. As they accumulate, the powders are selectively consolidated using a laser beam which is scanned in a predefined pattern using a galvo-mirror scan head. Unlike pre-placed powder bed techniques, both powder delivery and laser consolidation are performed simultaneously and without interruption. No powder delivery scrapers or rollers are used. The main characteristics of a prototype tower nozzle and the typical processing conditions used to form thin wall AISI H13 steel shapes are presented in this paper.

Key-words

Solid freeform fabrication, powder feedstock, AISI H13 steel

Introduction

Several solid freeform fabrication (SFF) techniques have been developed specifically for feedstock materials in powder form [1]. *Three-Dimensional Printing* (3DP) techniques [2, 3] use ink-jet printing technology to bind metal, ceramic or polymer powders and

form three-dimensional shapes. *Selective Laser Sintering* (SLS) [4] produces parts in elastomer, polycarbonate and nylon by laser processing powder forms of these materials. *Electron Beam Melting* (EBM) [5, 6], *Laser Powder Deposition* (LPD) techniques [7-11] derived from the blown powder laser cladding technique [12], and several variations of *SLS* [4, 13], including *Selective Laser Melting* [14] and *Direct Metal Laser Sintering* [15], are used to consolidate loose metal powders into solid three-dimensional parts.

A discussion on the two most common forms of delivering the feedstock powders during SFF can be found in reference [16]. The pre-placed powder bed strategy is used in SLS, EBM and drop-on-powder 3DP [3]. Here, a thin and flat layer of feedstock powders is spread evenly over the previous layer of processed material, using either a scraper or a roller. The powders are then consolidated and the process repeated until the final shape is obtained. For SLS, this feedstock delivery strategy allows laser processing to be performed using a galvo-mirror scan head. In other cases feedstock delivery and consolidation are performed simultaneously and without scrapers and rollers. In drop-on-drop 3DP [3], the feedstock powders are fed directly through the print head. In LPD, the feedstock powders are injected directly into the laser beam generated melt pool via a powder feeding nozzle. Although simple to implement, the lateral powder feeding nozzle configuration [17-20] has scan-direction dependent deposition rates, clearly reported in references [17, 20], and is therefore not suitable for most LPD applications. The limitations of this configuration, discussed in detail in reference [21], were overcome with the introduction of coaxial powder feeding nozzles that enable omni directional materials deposition. Coaxial nozzles have either a conical design, such as reported in [22], or a four lateral nozzle configuration as the one used in the LENS system [9]. Another feedstock delivery strategy, explored by Arcella, Whitney and Krantz during their initial work on the laser forming process [23], involves fluidizing the powders within the laser processing area. Despite the potential to deliver and fuse the feedstock powders simultaneously and without interruptions, the fluidized bed approach has apparently been abandoned.

Tower nozzle powder delivery

This new powder delivery strategy relies on a specially designed powder delivery nozzle, named tower nozzle, to dispense the feedstock powders continuously and uniformly onto the processing area where they accumulate progressively as a flat powder bed without interrupting the laser consolidation operation. The tower nozzle is mounted vertically in the center of the processing area as depicted in Figure 1. Carried by a gas stream, the feedstock powders travel up through the tower nozzle and disperse uniformly over the processing area. The airborne feedstock particles eventually settle as a flat powder bed, while the fluidization gas ascends vertically within the feedstock confinement cylinder and eventually exits the processing chamber through the vacuum pump line.

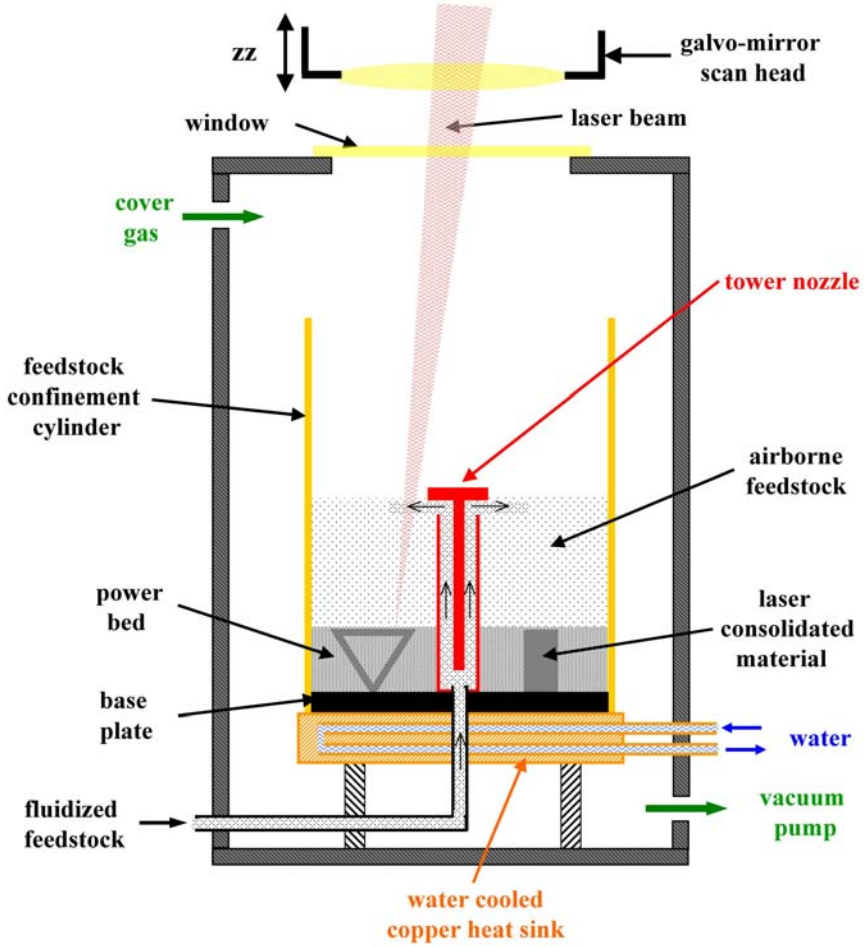

Figure 1 – Schematic representation of the tower nozzle solid freeform fabrication system. The three components that form the tower nozzle are shown in Figure 2.

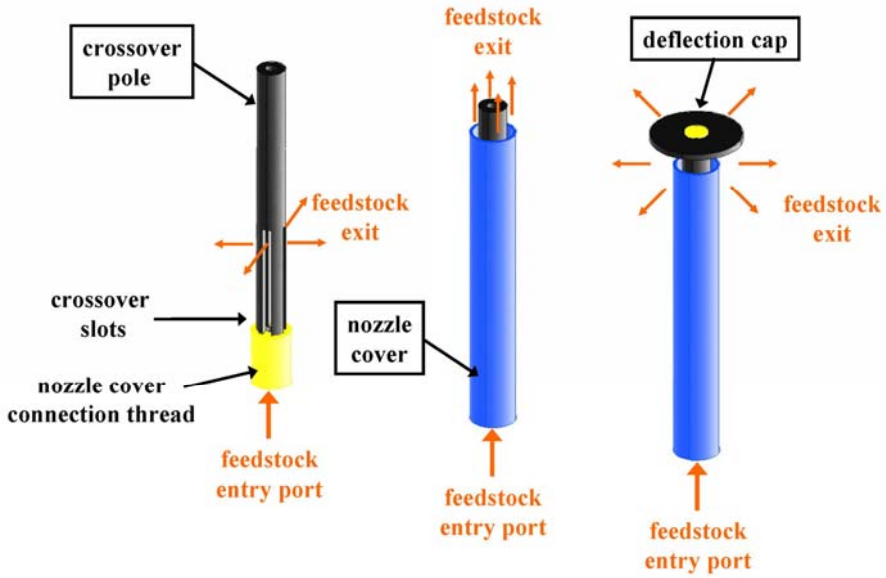

Figure 2 – The tower nozzle is formed by three concentric components: a crossover pole with four slots; a nozzle cover; a deflection cap.

The crossover pole transfers the incoming powder from the entry port to its exterior via four crossover slots (Figure 2 - left). The nozzle cover enclosing the crossover pole forces the feedstock to ascend vertically along a 1 mm wide annular cylindrical guide (Figure 2 - middle). The feedstock deflection cap attached to the crossover pole forces the feedstock to deflect radially (Figure 2 - right), covering the processing area uniformly.

The prototype tower nozzle solid freeform fabrication system

The prototype tower nozzle solid freeform fabrication (SFF) system chamber, laser scan head, and associated components are shown in Figure 3. The assembled prototype tower nozzle, presented schematically in Figure 2, is shown in Figure 4.

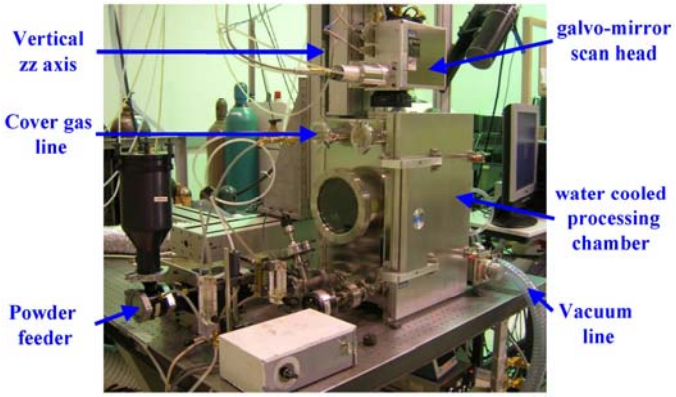

Figure 3 – The prototype tower nozzle SFF system.

Figure 4 – A 2 ½'' tall prototype tower nozzle in service at UTSI.

SFF is performed in a controlled atmosphere using a 1.06 μm 1kW diode-pumped ytterbium fiber laser (YLR-1000-WC by IPG Photonics). The feedstock powders are fed to the tower nozzle using a pneumatic Optomec powder feeder. The laser beam is rastered over the powder bed using a galvo-mirror scan head with a 80×80 mm^2 processing range (hurrySCAN30^{TM} by ScanLabs) according to the sequence of laser paths defined for each layer in the SAMLight^{TM} software (by Scaps). During SFF, the scan head moves up along the vertical zz axis (Figure 3) at a constant speed that equals the powder bed height accumulation rate, thus keeping the laser beam spot size constant throughout the SFF operation.

Experiments with AISI H13 steel

The effects that gas flow rate and confinement cylinder inner diameter (ID) have on the thickness and flatness of a tower nozzle deposited powder bed were analyzed for AISI H13 steel -100/+325 mesh powders (by Crucible Research). These powders were fed to the tower nozzle using Argon as a carrier gas. Five Argon flow rates – 5, 10, 15, 20 and

30 standard cubic feet per hour (SCFH) – and three confinement cylinders – 3'', 4'' and 5'' ID – were used. A powder bed was formed for each combination of gas flow rate and confinement cylinder ID. After a deposition period of 600 seconds, the confinement cylinder was removed. For each combination of confinement cylinder ID and gas flow rate, a print of the resulting powder bed profile was obtained by cutting the powder bed with the sticky end of a Post-it™ note, as shown in Figure 5.

Figure 5 – Post-it™ measurement of the profile of a tower nozzle deposited powder bed.

The powder bed profile obtained for the 3'' cylinder using an Argon flow rate of 5 SCFH is shown in Figure 6.

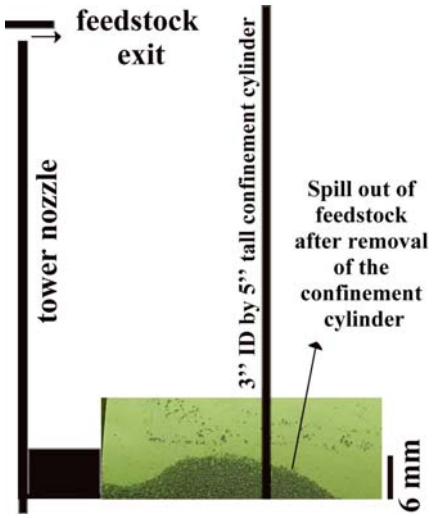

Figure 6 – Post-it™ note print of the powder bed profile obtained for a 3'' ID confinement cylinder using an Argon flow rate of 5 SCFH. This print is overlaid by a schematic representation of the relative positions of the tower nozzle and confinement cylinder. The significant spill out of feedstock after removal of the confinement cylinder points to a significant accumulation of feedstock next to the wall of the confinement cylinder.

At 5 SCFH, the H13 particles exit the tower nozzle at relatively low velocity. This results in a highly uneven powder bed as few particles accumulate near the nozzle. This happens even with the 3'' cylinder (Figure 6) where the particles are more likely to bounce off the confinement cylinder wall back to the nozzle surroundings. At 10 SCFH (Figure 7), the H13 particles have enough momentum to bounce off the walls of the 3 and 4'' cylinders. A near-flat powder bed was obtained with the 4'' cylinder with little accumulation near the cylinder wall (Figure 7). Under these flow conditions, the powder bed height accumulation rate and the mass accumulation rate within the 4'' cylinder equal 375 μm/min and 13.8 g/min, respectively. At different gas flow rates, one obtains very distinct profiles: while in some cases one obtains essentially flat powder beds (3'' at 15 and 30 SCFH), in other cases one gets highly uneven powder beds with accumulation of feedstock near both nozzle and confinement cylinder wall (5'' at 30 SCFH).

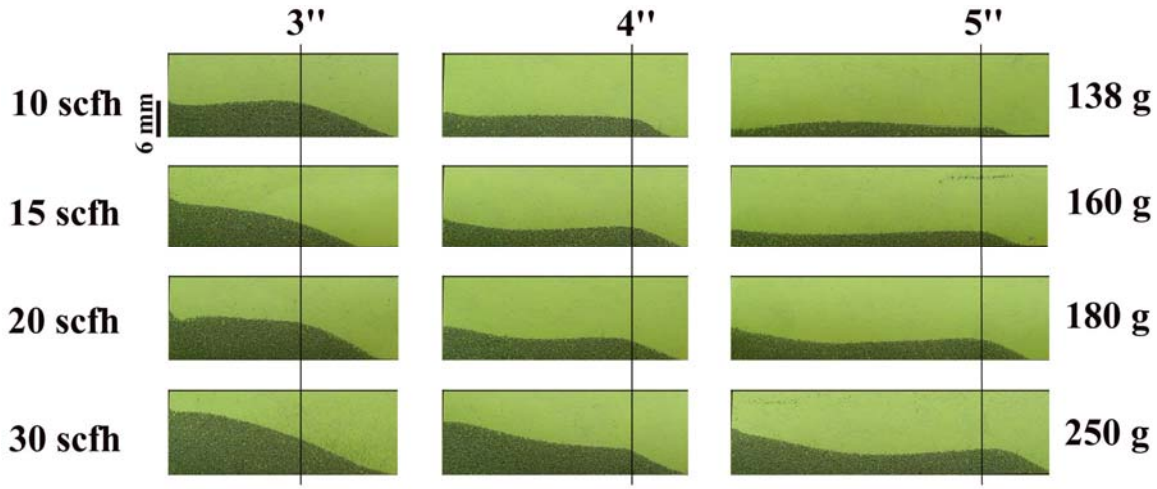

Figure 7 – Sticky note prints of powder bed profiles obtained for different combinations of Argon flow rate and confinement cylinder ID. The mass of AISI H13 powder obtained for each Argon flow rate, after the 600 second deposition period, is also shown.

A 40 mm tall University of Tennessee logo made in AISI H13 steel using the tower nozzle SFF technique is shown in Figure 8.

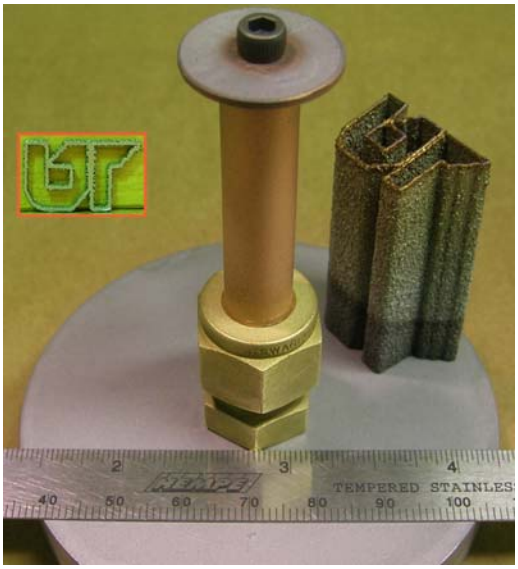

Figure 8 – A 40 mm tall AISI H13 steel solid freeform fabricated extrusion of the University of Tennessee logo. The outlined insert, depicting a 2 mm thick slice of the UT logo extrusion, reveals that the AISI H13 material is fully dense.

This UT logo was built on a ¼'' thick, 3'' diameter AISI 4140 steel disk and inside a 5'' tall 3'' inner diameter confinement cylinder. The powder bed height accumulation rate was 1 mm/min. A 180 W laser beam, focused to a 0.9 mm diameter spot, was scanned over the powders at 20 mm/s, allowing for an 80 μm thick layer of laser melted and solidified material to be deposited every 5 seconds. Under these conditions, 480 layers (i.e., 40 mm of material) were deposited in 40 minutes. When cross-sectioned as in the outlined insert of Figure 8, the material was found to be fully dense. The powder feeding conditions used to fabricate the UT logo produced a slight accumulation of feedstock next to the confinement cylinder wall that visibly affected the flatness of the powder bed once the height of the build exceeds 25 mm. The effects of this localized accumulation worsened as the logo height increased. The 30 mm logo (Figure 9) exhibited a maximum height variation of 1 mm, while the 40 mm logo (Figure 10) exhibited a maximum height variation of 3 mm.

Discussion

Figure 9 – A 30 mm AISI H13 steel solid freeform fabricated extrusion of the University of Tennessee logo.

Figure 10 – A 40 mm AISI H13 steel solid freeform fabricated extrusion of the University of Tennessee logo.

The results show that the tower nozzle powder delivery strategy is suitable for SFF operations. Besides thin wall objects, the tower nozzle approach has also been used to form AISI H13 steel items with bulk sections and overhangs. The produced near-net shape items have a relatively poor surface finish given the incompletely melted particles that cover the surfaces of the produced items.

Unlike other SFF processes, there is no need for either a complex LPD powder feeding nozzle or powder scrapers or rollers. The tower nozzle is compact, simple to construct and allows delivery and laser consolidation of the feedstock powders to be performed simultaneously and without interruption. This keeps the deposited material warm during the entire deposition operation, a fact that may prove valuable when depositing high melting temperature materials. This SFF technique can be potentially used with all materials commonly processed with SLS, EBM and LPD and may be of great interest for SFF of small, custom tailored items such as dental implants.

The feedstock confinement cylinder is a fundamental component of the system's design. Without it, one cannot obtain a flat powder bed. By containing the airborne feedstock within the processing range of the galvo-mirror scan head, the confinement cylinder also maximizes the powder bed height accumulation rate. The powder bed height accumulation rate and profile depend strongly on confinement cylinder inner diameter and gas flow rate. The profile is also expected to depend on the tower nozzle height and to change somewhat during deposition as the powder bed accumulates. Accumulation rate and profile are known to depend on the feedstock powders used.

Conclusions

The tower nozzle solid freeform fabrication technique has been successfully used to laser consolidate AISI H13 steel powders into dense three dimensional shapes. Combinations of gas flow rate and confinement cylinder diameter can be found which lead to a suitable delivery of feedstock powders to the processing area were identified. Within the 45 cm^2 processing area delimited by a 3'' ID confinement cylinder, the feedstock powders were

laser consolidated at a build rate of 1 mm/min, up to a height of 40 mm. With the 2 ½'' tall prototype tower nozzle, the part build height remains consistent up to 25 mm.

Acknowledgements

This work is supported by the Tennessee Higher Education Commission through a grant to the Center for Laser Applications.

References

1. Wohlers, T., *Wohlers Report 2006*. 2006, Wohlers Associates: Fort Collins, Colorado, USA.
2. Sachs, E., et al., *Production of Injection Molding Tooling with Conformal Cooling Channels using the Three Dimensional Printing Process.* Polymer Engineering and Science, 2000. 40(5): p. 1232-1247.
3. Dimitrov, D., K. Schreve, and N.d. Beer, *Advances in three dimensional printing - state of the art and future perspectives.* Rapid Prototyping J, 2006. 12(3): p. 136-147.
4. Kruth, J.P., et al., *Lasers and materials in selective laser sintering.* Assembly Automation, 2003. 23(4): p. 357-371.
5. Gibbons, G.J. and R.G. Hansell, *Direct Tool Steel Injection Mould Inserts through the ARCAM EBM free-form fabrication process.* Assembly Automation, 2005. 25(4): p. 300-305.
6. Cormier, D., O. Harrysson, and H. West, *Characterization of H13 steel produced via electron beam melting.* Rapid Prototyping J, 2004. 10(1): p. 35-41.
7. Sears, J.W. *Direct Laser Powder Deposition*. in *ASTM/TMS Materials Week*. 1999. Cincinnati, OH, USA.
8. Arcella, F.G. and F.H. Froes, *Producing Titanium Aerospace Components from Powder using Laser Forming.* JOM, 2000. 52(5): p. 28-30.
9. Keicher, D.M. and W.D. Miller, *LENS moves beyond RP to direct fabrication.* Metal Powder Report, 1998. 53: p. 26-28.
10. Mazumder, J., et al., *The direct metal deposition of H13 tool steel for 3D components.* JOM, 1997. 49(5): p. 55-60.
11. Xue, L. and M.U. Islam, *Free-form laser consolidation for producing metallurgically sound and functional components.* J Laser Appl, 2000. 12(4): p. 160-165.
12. Vilar, R., *Laser cladding.* J Laser Appl, 1999. 11(2): p. 64-79.
13. Agarwala, M., et al., *Direct selective laser sintering of metals.* Rapid Prototyping J, 1995. 1(1): p. 26-36.
14. Kruth, J.P., et al., *Binding mechanisms in selective laser sintering and selective laser melting.* Rapid Prototyping J, 2005. 11(1): p. 26-36.
15. Radstok, E., *Rapid Tooling.* Rapid Prototyping J, 1999. 5(4): p. 164-168.
16. Wu, X., *A review of laser fabrication of metallic engineering components and of materials.* Materials science and technology, 2007. 23(6): p. 631-640.
17. Murphy, M., C. Lee, and W.M. Steen. *Studies in rapid prototyping by laser surface cladding*. in *ICALEO*. 1993. Orlando, Florida, USA: Laser Institute of America.
18. Kreutz, E.W., et al., *Rapid prototyping with C02 laser radiation.* Appl Surf Sci, 1995. 86: p. 310-316.
19. Gremaud, M., et al., *Laser metal forming: process fundamentals.* Surf Eng, 1996. 12(3): p. 251-259.
20. Fessler, J.R., et al. *Laser deposition of metals for shape deposition manufacturing*. in *Solid Freeform Fabrication Symposium*. 1996. Austin, Texas, USA: University of Texas at Austin.
21. Hu, Y.P., C.W. Chen, and K. Mukherjee, *Development of a new laser cladding process for manufacturing cutting and stamping dies.* J Mater Sci, 1998. 33: p. 1287-1292.

22. Koch, J.L. and J. Mazumder. *Rapid prototyping by laser cladding*. in *ICALEO*. 1993. Orlando, Florida, USA: Laser Institute of America.
23. Arcella, F.G., E.J. Whitney, and D. Krantz. *Laser Forming Near Shapes in Titanium*. in *ICALEO*. 1995: Laser Institute of America.

APPENDIX II

AXIS-SYMMETRIC SOLID FREEFORM FABRICATION OF W-TiC CERMELT ROCKET NOZZLES

(This paper was published in the Proceedings of 2008 World Congress on

Powder Metallurgy & Particulate Materials)

AXIS-SYMMETRIC SOLID FREEFORM FABRICATION OF W-TiC CERMELT ROCKET NOZZLES

Lino Costa, William Hofmeister, Deepak Rajput, Kathleen Lansford

University of Tennessee Space Institute
Center for Laser Applications
411 B. H. Goethert Parkway
Tullahoma, TN 37388

ABSTRACT

Refractory metal (W,Ti) – refractory carbide (Ti,W)C alloys formed by eutectic solidification from the melt – cermelts – are promising materials for high temperature rocket nozzle applications. At the Center for Laser Applications (CLA) at the University of Tennessee Space Institute (UTSI), these materials are being formed into three-dimensional shapes using various laser powder deposition techniques. Shapes with cylindrical symmetry are built on graphite mandrels by laser melting a continuous powder feedstock mix. Processing is performed inside a Argon atmosphere and the obtained materials have a fully dense microstructure of fine (Ti,W)C dendrites surrounded by the (W,Ti) – (Ti,W)C eutectic. With a melting temperature of 2700 °C, this microstructure is expected to offer high temperature strength, toughness and erosion resistance at elevated temperatures. The specific axis-symmetric solid freeform fabrication technique, typical processing conditions and a representative set of results are presented herein.

INTRODUCTION

Soaring oil prices have triggered a massive jump in the price of Rhenium [1]. Rhenium currently trades above $11000 / kg, up from $1330 / kg during 2007 and $1260 / kg during 2006 [2]. This rise in the price of Rhenium is driven by the airline industry's demand for more fuel-efficient jet engines [1], based on single-crystal nickel-based super-alloys containing 3-6 wt. % Rhenium [3-7]. Demand for these super-alloys is estimated to account for about 77% of current world Rhenium consumption [8]. Within the aerospace industry, Iridium-coated Rhenium is the preferred material to make rocket nozzles and thrust-combustion chambers [9-15]. Amongst the low cost alternatives to Rhenium in rocket nozzle applications are castable refractory metal – refractory carbide [16] and refractory metal – refractory carbonitride [17] alloys formed by eutectic solidification from the melt. Here, the essential idea is to cast, from the melt, a eutectic

alloy of a refractory metal phase and its monocarbide or carbonitride – a **cermelt**[1]. For example, the W-Ti-C ternary system, investigated in detail by Erwin Rudy [16], has a eutectic point at 2700 ºC and composition (58 W - 20 Ti - 22 C at. %) (Figure 11) where a tungsten rich liquid solidifies to the refractory (W,Ti) metal phase and the (Ti,W)C monocarbide phase.

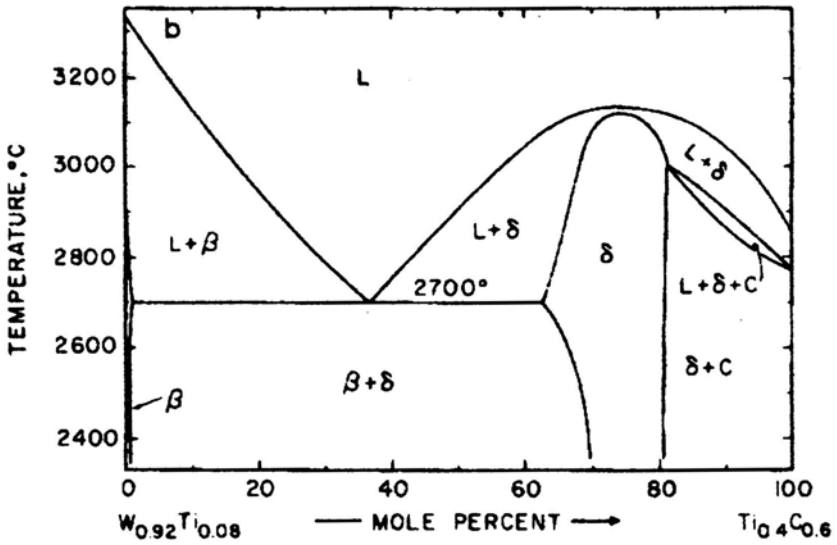

Figure 11 – Isopleth at the pseudobinary section metal + monocarbide. Source: [16]. β – (W,Ti) metal phase; δ – (Ti,W)C monocarbide phase. Within this composition range, the W_2C phase does not form.

The cast eutectic (W,Ti) – (Ti,W)C is known to have excellent hot hardness [16], outperforming WC cemented carbide counterparts at temperatures above 500 ºC (Figure 12), and is therefore expected to have exceptional high temperature erosion resistance.

Developed initially for metal removal tool applications, the machinability and formability of (W,Ti) – (Ti,W)C cermelts is problematic. Their exceptional hardness severely limit the use of machining techniques for shaping purposes, and the high melting temperatures involved raise considerable melt processing and casting difficulties. Moreover, to create a very fine carbide phase distribution and achieve the full benefits of alloy strength, wear resistance and toughness, the material must be rapidly solidified from the melt. Alternatively, these (W,Ti) – (Ti,W)C cermelts can be produced by laser melting mixtures of tungsten and titanium carbide powders, as shown by Hofmeister et al [18]. (W,Ti) – (Ti,W)C cermelts produced by laser melting 85.55 wt% W – 14.45 wt% TiC powder compacts exhibit a fine microstructure consisting of primary dendrites of (Ti,W)C surrounded by the (W,Ti) + (Ti,W)C eutectic (Figure 13 and Figure 14).

[1] "Cermelts" are formed from the melt, as opposed to cermets formed by press and sinter or thermal spraying techniques.

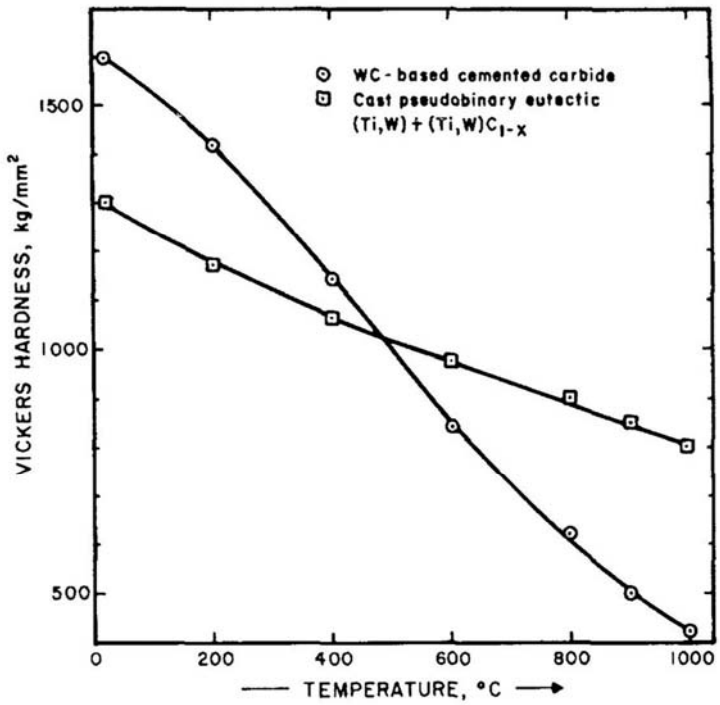

Figure 12 – Vickers hardness as a function of temperature for commercial WC cemented carbide material and cast eutectic (W,Ti) – (Ti,W)C cermelt. Source: [16].

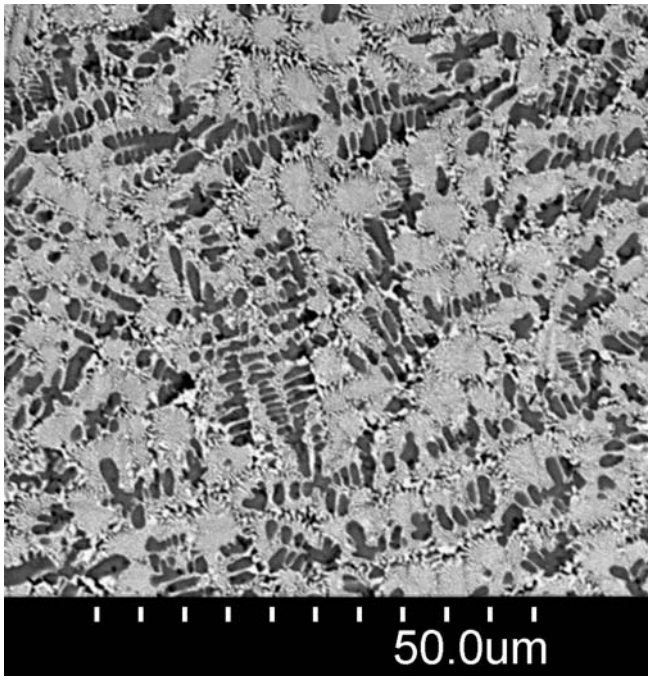

Figure 13 – A SEM micrograph of a (W,Ti) – (Ti,W)C cermelt. Source: [18]. Dark areas are primary dendrites of (Ti.W)C. Light areas are the (W,Ti) – (Ti,W)C eutectic, shown in more detail in Figure 14.

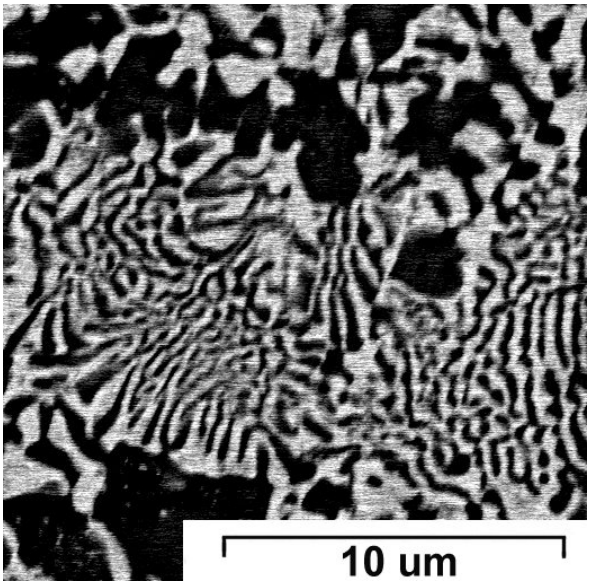

Figure 14 – A SEM image of the eutectic structure of the a (W,Ti) – (Ti,W)C cermelt. Source: [18]. The light areas are the (W,Ti) metallic phase and the dark regions are the (Ti,W)C ceramic phase.

Microhardness measurements performed on these (W,Ti) – (Ti,W)C cermelts revealed a hardness ranging typically between 1100 and 1300 HV, which is consistent with the data reported by Rudy et al (Figure 12).

These results open the door to the fabrication of near-net shape (W,Ti) – (Ti,W)C cermelt components via laser powder deposition (LPD) techniques [19, 20]. With LPD, three dimensional components are built layer by layer. Each layer is formed progressively as the feedstock material in powder form is injected into the laser beam's path, melted simultaneously with a thin surface layer of the underlying material, and rapidly resolidified into continuous deposits that overlap in a suitable pattern. Given its ability to progressively deposit relatively small amounts of laser melted and resolidified material at precise locations, LPD combines all the advantages of solid freeform fabrication (SFF) with the benefits of rapid solidification processing [21, 22].

AXIS-SYMMETRIC LASER POWDER DEPOSITION APPARATUS

Figure 15 shows the experimental LPD apparatus used to form cylindrical (W,Ti) – (Ti,W)C cermelt shapes.

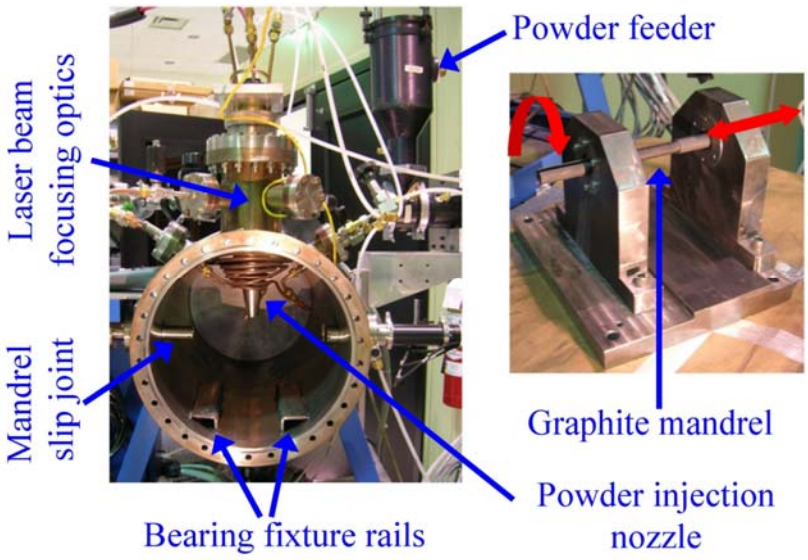

Figure 15 – Controlled atmosphere processing chamber (left) and twin-bearing mount used to laser powder deposit refractory materials on graphite mandrels. The graphite mandrel rotates and displaces linearly under the laser beam.

These shapes are built on graphite mandrels by laser melting a continuous feed of feedstock powders inside an Argon atmosphere. The graphite mandrels used in the experiments were semiconductor grade (manufactured by Poco Graphite, Inc.). Prior to LPD, the deposition section of the mandrels was machined down to an outer diameter of 10 mm and coated with a 100-200 μm thick layer of Titanium or Tantalum powders. This powder layer serves two purposes: (1) it protects the graphite from direct exposure to the high laser power required for melting the cermelt feedstock powders, thus preventing graphite from sublimation and (2) it provides a better base to deposit the cermelt material. During LPD, the graphite mandrel rotates and displaces linearly under the laser beam, at 0.2 Hz and 0.2 mm/s, respectively. Processing was performed in an 760 torr Argon atmosphere using a continuous wave Hobart HLP 3000 3 kW Nd:YAG laser. The feedstock powders were fed into an Argon gas stream using a pneumatic Optomec powder feeder and delivered continuously into the laser beam generated melt pool during laser processing through a lateral powder injection nozzle.

APS NANOENCAPSULATED TUNGSTEN-COATED TITANIUM CARBIDE POWDERS

To avoid the loss of carbon that results when carbide powders are laser processed, the starting material was nanoencapsulated Tungsten-coated Titanium Carbide (W-coated TiC) powders produced by Advanced Powder Solutions, Inc. (APS) using a chemical deposition process [23, 24]. The interface of these powders has a melting temperature (~ 2700 ºC) much lower than that of Tungsten (~ 3422 ºC) and Titanium Carbide (~ 3160 ºC). A pictorial description and a SEM view of these particles are shown in Figure 16.

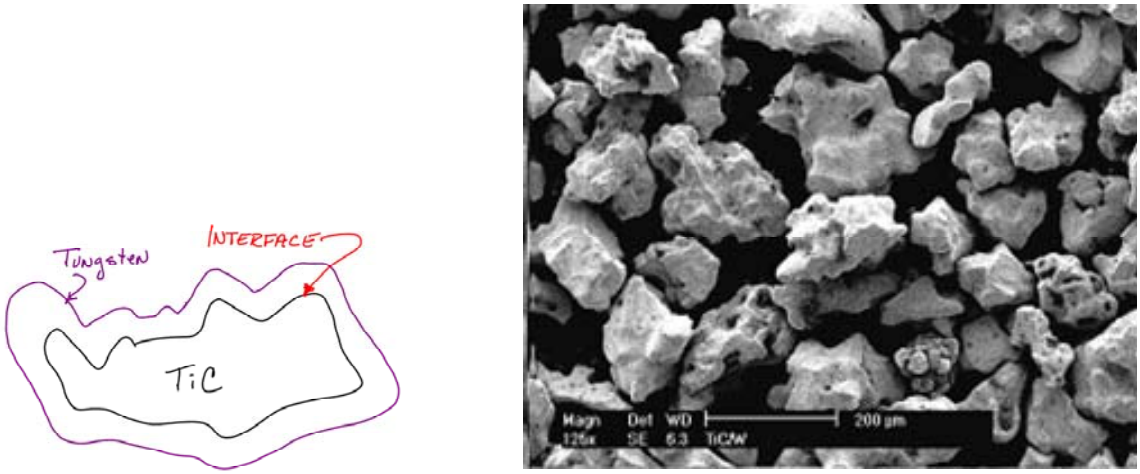

Figure 16 – APS nanoencapsulated W-coated TiC powders by Advanced Powder Solutions, Inc.

EXPERIMENTS WITH APS W-COATED TiC POWDERS

A 30 mm long cylinder produced on Ti coated graphite mandrel using 1200 W laser power and a ¾ (32-38 µm W) + ¼ (75-106 µm APS W-coated TiC) powder mix is shown in Figure 17. The extra Tungsten powder was added to the APS W-coated TiC powder in order to shift the stoichiometry of the feedstock powder closer to the 85.5 wt.% T – 14.5 wt.% TiC eutectic composition.

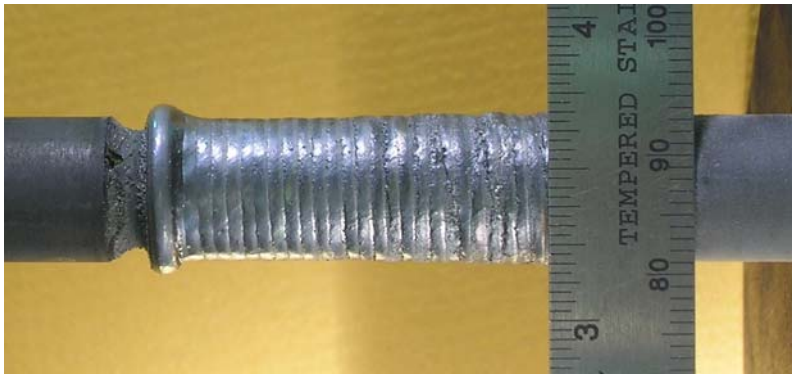

Figure 17 – A 30 mm long cylinder produced using a ¾ (32-38 µm W) + ¼ (75-106 µm APS W-coated TiC) powder mix.

This part presents a sintered type microstructure formed by partial melting of the feedstock powders during laser processing, as seen in Figure 18.

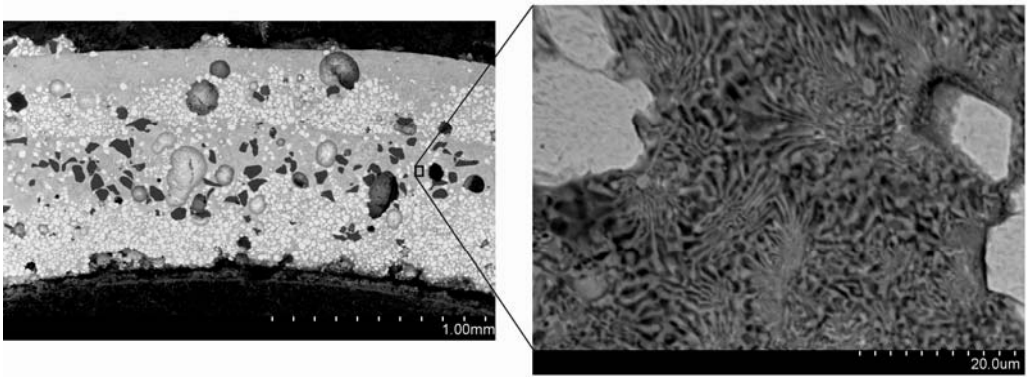

Figure 18 – A SEM view of the microstructure of the laser powder deposited material shown in Figure 17. One the left, one can clearly observe unmelted feedstock particles. On the right, one can observe the fine (W,Ti) – (Ti,W)C eutectic formed between the unmelted particles.

The laser beam power was raised to completely fuse the feedstock powders. At 1400 W, most of the feedstock powders melt under the action of the laser beam, as seen in Figure 19. Here, only the region closest to the graphite mandrel surface presents unmelted feedstock particles. The fully melted region presents a microstructure of fine (Ti,W)C surrounded by the (W,Ti) + (Ti,W)C eutectic, as observed previously in reference [18]. One also notes the presence of cracks within the fully melted material, which do not appear to propagate into the partially melted region. Parts produced at 1400 W were more brittle than those produced at 1200 W.

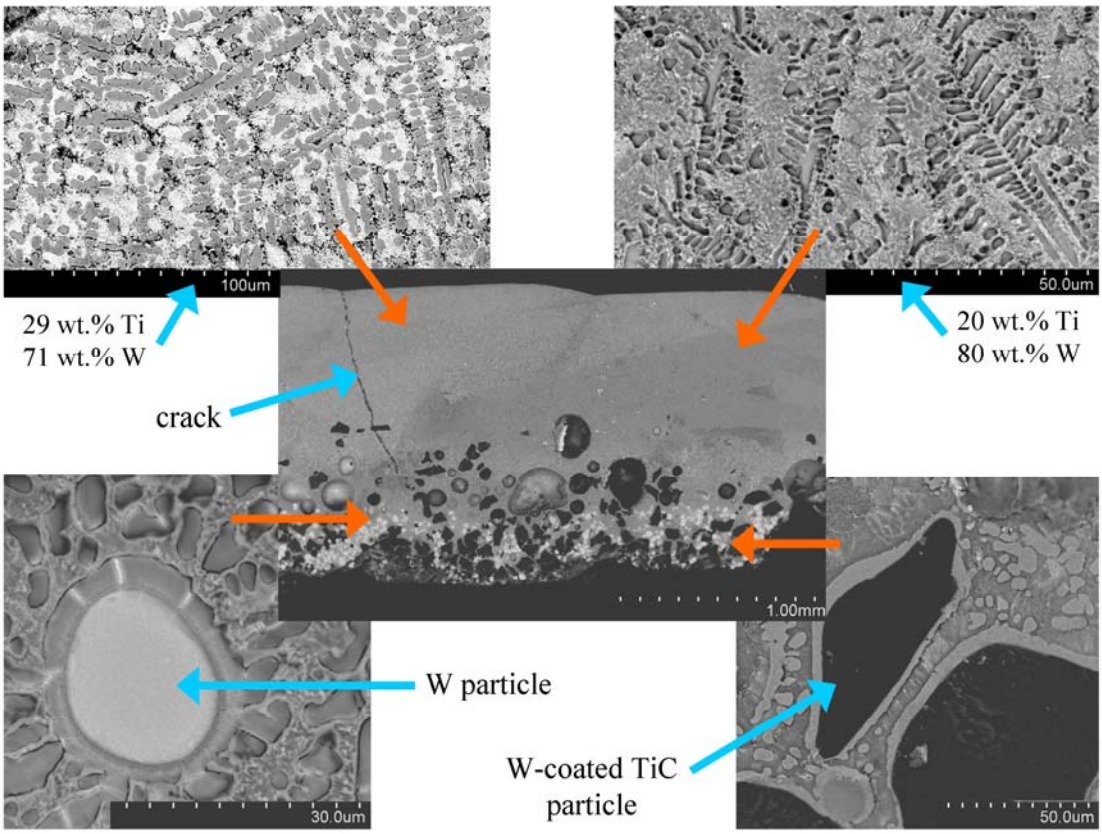

Figure 19 – A SEM view of the microstructure of the material deposited at 1400 W.

A fully melted but brittle microstructure was obtained when the feedstock powders were laser processed at 1600 W (Figure). The obtained microstructure presents various defects at the interface where consecutive laser passes overlap.

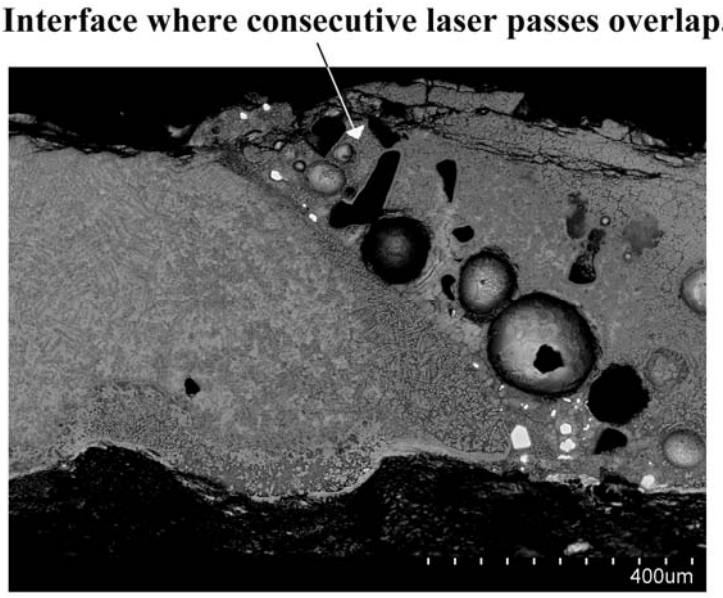

Figure 20 – A SEM view of the microstructure of the material deposited at 1600 W.

EXPERIMENTS WITH TANTALUM

A 30 mm long cylinder produced on Ta coated graphite mandrel using 1200-1400 W laser power and -80/+270 mesh Ta powders is shown in Figure .

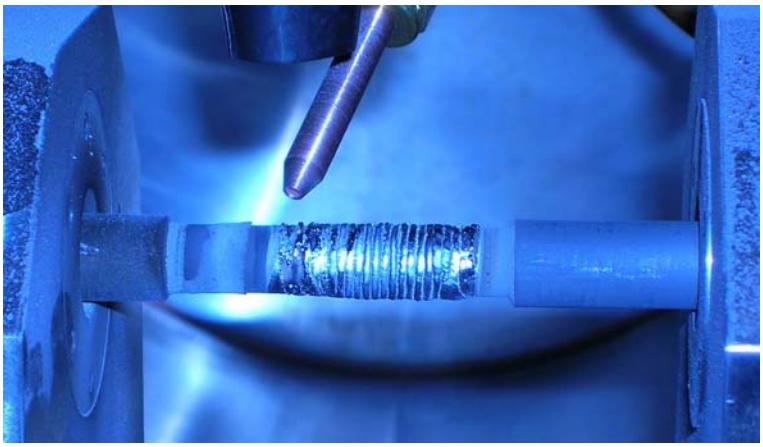

Figure 21 - A 30 mm long cylinder produced using -80/+270 mesh Ta powders.

This part presents a fully melted microstructure except for a narrow region near to the interface with the graphite mandrel (Figure). Unlike the fully melted cermelt samples, this Tantalum sample presents no cracks.

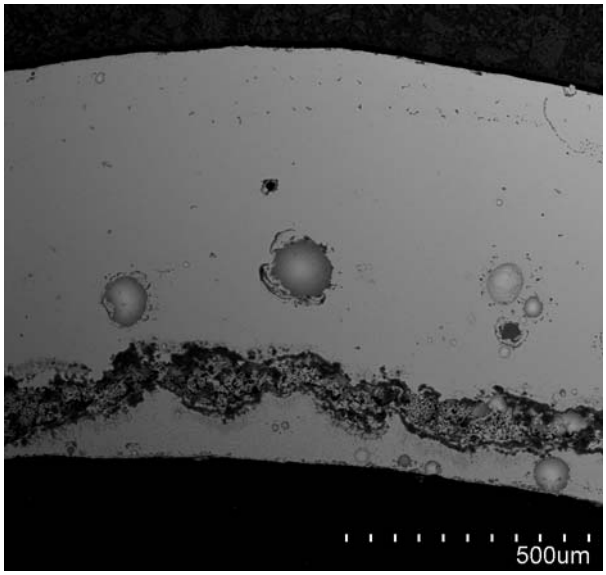

Figure 22 – A SEM cross-sectional view of the microstructure of the laser powder deposited Ta.

SUMMARY

A laser powder deposition technique suitable for near-net shape fabrication of axis-symmetric components on graphite mandrels has been successfully demonstrated. The technique is particularly suited for the deposition of refractory materials and fabrication of rocket nozzles and thrust-combustion chambers. This deposition technique was successfully applied to the deposition of Tantalum. The potential to form cylindrical shape (W,Ti) – (Ti,W)C cermelts by laser powder depositing a mix of Tungsten and APS Tungsten-coated Titanium Carbide powders was also demonstrated. However, the produced materials present poor toughness. The formed cermelts present a microstructure of finely distributed (Ti,W)C dendrites surrounded by a (W,Ti) + (Ti,W)C eutectic. The cermelts also present some inhomogeneities, especially at the interface where consecutive laser passes overlap, and cracks that render the cermelts more brittle than the materials formed at lower laser power levels, which exhibit a sintered type microstructure.

The Titanium and Tantalum powder layers deposited on the graphite mandrels prior to laser powder deposition revealed effective in protecting the graphite mandrels from sublimation during laser processing and provided a suitable base for deposition of the (W,Ti) – (Ti,W)C cermelts and Tantalum. The nanoencapsulated powders from Advanced Powder Solutions were successfully melted by laser processing without excessive carbon loss. Nanoencapsulation of carbide powders and laser freeform fabrication of near net shape parts can be combined to provide a promising route to fabrication of low cost rocket nozzles.

ACKNOWLEDGEMENTS

The authors gratefully acknowledge NASA STTR support by a contract through Advanced Powder Solution, Inc.. The authors extend their gratitude towards Dr. Craig Morton of ATT Stellram for his guidance and useful discussion during the course of this project. This work was also supported by the Tennessee Higher Education Commission through a grant to the Center for Laser Applications, University of Tennessee Space Institute.

REFERENCES

1. J. Blas, "Rare metal prices soar on demand for more fuel-efficient jet engines", *Financial Times*, 2008, June 18, pp. 22-24.
2. M.J. Magyar, "Rhenium Statistics and Information", *2008 U.S. Geological Survey Mineral Commodity Summaries*, 2008, pp. 136-137.
3. K. Harris, G.L. Erickson, S.L. Sikkenga, W.D. Brentnall, J.M. Aurrecoechea and K.G. Kubarych, "Development of two Rhenium-containing superalloys for single-crystal blade and directionally solidified vane applications in advanced turbine engines", *Journal of Materials Engineering and Performance*, 1993, vol. 2, no. 4, pp. 481-487.
4. K.P.L. Fullagar, R.W. Broomfield, M. Hulands, K. Harris, G.L. Erickson and S.L. Sikkenga, "Aero engine test experience with CMSX-4 alloy single-crystal turbine blades", *Journal of Engineering for Gas Turbines and Power*, 1996, vol. 118, pp. 380-388.
5. R.W. Broomfield, D.A. Ford, J.K. Bhangu, M.C. Thomas, D.J. Frasier, P.S. Burkholder, K. Harris, G.L. Erickson and J.B. Wahl, "Development and turbine engine performance of three advanced Rhenium containing superalloys for single crystal and directionally solidified blades and vanes", *Journal of Engineering for Gas Turbines and Power*, 1998, vol. 120, pp. 595-608.
6. A. Akhtar, S. Hegde and R.C. Reed, "The oxidation of single-crystal nickel-based superalloys", *JOM*, 2006, pp. 37-42.
7. K. Kawagishi, H. Harada, A. Sato, A. Sato and T. Kobayashi, "The oxidation properties of fourth generation single-crystal nickel-based superalloys", *JOM*, 2006, pp. 43-46.
8. M.J. Magyar, "Rhenium", *2006 U.S. Geological Survey Minerals Yearbook*, 2008, pp. 62.0-62.5.
9. S.J. Schneider, "High temperature thruster technology for spacecraft propulsion", *Acta Astronautica*, 1992, vol. 28, pp. 115-125.
10. R.C. Stechman, "Advanced thrust chamber materials for earth storable bipropellant rocket engines", *Acta Astronautica*, 1993, vol. 29, no. 2, pp. 109-115.
11. R.H. Tuffias, "Fabrication processes for Iridium/Rhenium combustion chambers", *Materials and Manufacturing Processes*, 1998, vol. 13, no. 5, pp. 773-782.
12. J.O. Milewski, D.J. Thoma, J.C. Fonseca and G.K. Lewis, "Development of a near net shape processing method for Rhenium using Directed Light Fabrication", *Materials and Manufacturing Processes*, 1998, vol. 13, no. 5, pp. 719-730.
13. D. Mittendorf and G.A. West, "New processes to produce Rhenium metal shapes", *Materials and Manufacturing Processes*, 1998, vol. 13, no. 5, pp. 749-755.

14. B.D. Reed, J.A. Biaglow and S.J. Schneider, "Engineering issues of Iridium coated Rhenium rockets", *Materials and Manufacturing Processes*, 1998, vol. 13, no. 5, pp. 757-771.
15. R. Hickman, T. McKechnie and A. Agarwal, "Net shape fabrication of high temperature materials for rocket engine components", *37th AIAA/ASME/SAE/ASEE Joint Propulsion Conference*, American Institute of Aeronautics & Astronautics, 2001.
16. E. Rudy, "Constitution of ternary titanium-tungsten-carbon alloys", *Journal of Less-Common Metals*, 1973, vol. 33, pp. 245-273.
17. E. Rudy, "Method for making castable carbonitride alloys", US Patent No. 3703368, 1972.
18. W. Hofmeister, L. Costa, D. Rajput and K. Lansford, "Cast carbide-metal composite components via laser based solid freeform fabrication", *26th ICALEO*, LIA, 2007.
19. J.W. Sears, "Direct Laser Powder Deposition", *ASTM/TMS Materials Week*, 1999.
20. J.W. Sears, "Solid freeform fabrication technologies: rapid prototyping - rapid manufacturing", *Int J Powder Metall*, 2001, vol. 37, no. 2, pp. 29-30.
21. W. Hofmeister, M. Griffith, M. Ensz and J. Smugeresky, "Solidification in direct metal deposition by LENS processing", *JOM*, 2001, vol. 53, no. 9, pp. 30-34.
22. W. Hofmeister, M. Griffith, M. Ensz and J. Smugeresky, "Melt pool imaging for control of LENS processing", *International Conference on Metal Powder Deposition for Rapid Manufacturing*, Metal Powder Industries Federation, 2002.
23. D. Baker et al., "Net shape processing of encapsulated powders, Phase I SBIR Final Report Contract NNM05AA65C", 2005.
24. A. Biswas, D. Baker, R. Echols, Y. Zhou, B. Zheng, E.J. Lavernia, W. Hofmeister and H. Meeks, "Advanced composites through nano engineering", *2008 World Congress on Powder Metallurgy & Particulate Materials*, MPIF, 2008.

APPENDIX III

MOLYBDENUM-ON-CHROMIUM DUAL COATING ON STEEL

(This paper has been accepted for publication by Surface & Coatings Technology Journal)

Molybdenum-on-Chromium Dual Coating on Steel

Deepak Rajput[*]*, Kathleen Lansford, Lino Costa, William Hofmeister*

Center for Laser Applications
University of Tennessee Space Institute
411 B.H. Goethert Parkway
Tullahoma, TN 37388, USA

Abstract

Molybdenum and chromium coatings were deposited on AISI 4130 steel using the Laser Induced Surface Improvement[2] (LISI^{TM}) process. In this process a mixture of precursor material is pre-placed on the substrate and then laser melted, resulting in the formation of a thin surface layer of alloy on the underlying material. First, a chromium coating was deposited on steel using the Cr-CrB_2 eutectic composition, and subsequently a molybdenum coating using the Mo-MoB eutectic composition was deposited on the chromium layer. Both the coatings have been individually characterized and compared using scanning electron microscope, energy dispersive spectrometry, Vicker's hardness, X-ray diffraction, wear and erosion. The chromium layer exhibited superior erosion resistance (ASTM G76) while the molybdenum-on-chromium coating performed better in sliding wear (ASTM G77).

Keywords: Alloying; Cladding; Laser melting; Wear; Molybdenum; Chromium.

---

1. Introduction

Surface coatings of steel based on molybdenum are known to improve the wear resistance of the substrate, and are therefore used in a variety of engineering industries such as automotive, aerospace, paper and plastics [1-6]. Molybdenum based coatings provide low friction and good resistance to scuffing under sliding contact conditions [1, 3, 5, 6]. However, pure molybdenum has low hardness [5, 7] and forms a volatile oxide [5, 6] which limits its applicability. Early work showed that the carbide dispersion-hardened molybdenum (TZM alloy) appreciably improved high temperature mechanical properties [8], and carbon additions enhanced the hardness of the molybdenum matrix by forming Mo_2C [7].

[*] Corresponding author. Tel.: +1 9313937475; fax: +19314542271.
Email address: drajput@utsi.edu (D. Rajput).
[2] LISI^{TM} is a registered trademark of the University of Tennessee Research Corporation.

Flame spraying and plasma spraying are two methods used to deposit molybdenum coatings on various substrates. Both processes project semi-molten or molten particles on the substrate. Flame sprayed Mo coatings have high hardness due to the formation of MoO_2 which acts as a dispersion strengthener [5, 6]. Plasma sprayed Mo coatings are inherently soft, and alloying or dispersion strengthening is necessary to improve the wear properties at the expense of their friction characteristics [9]. The major problems associated with coatings processed through thermal spraying techniques are porosity and poor adhesion of coatings to the substrate. Although porosity is required for some thermal barrier coatings, it is detrimental to corrosion resistance, thermal conductivity and elastic modulus [10, 11].

Our research focused on the preparation of Mo coatings that have good wear resistance, high hardness, and excellent adhesion to the substrate. In the LISI^{TM} process, a precursor mixture of powder alloying compounds is mixed in a water-based thixotropic binder and sprayed on the substrate with an air spray gun. The water-based binder is added to keep the powder particles in suspension during the spray process and adhere the mixture to the substrate. The precursor layer is dried at 70^{o}C under a heat lamp for several hours prior to laser processing. The dried precursor layer is then laser alloyed into the substrate. This alloying leads to the formation of a coating with strong metallurgical bond, since the coating mixed in the liquid phase with the element(s) present in the substrate. This adulteration of the coating with the substrate element(s) is termed dilution, which may or may not be useful as far as the coating performance is concerned. Deposition of Mo coating on steel through LISI^{TM} route has not been reported so far and we take this opportunity to describe the nature of Mo coating produced through this route.

For systems with molybdenum as the precursor and AISI 4130 steel as the substrate, the melting temperatures of molybdenum and steel are approximately 2610^{o}C and 1435^{o}C, respectively. At temperatures above the melting point of the steel but below that of molybdenum, the steel melts and moves up by capillary action and other stirring forces, and fills up the pores between the molybdenum particles. It leaves behind a composite layer of resolidified steel and unmelted molybdenum particles, very similar to what was explained by Chong et al. [12] for Mo-TiC metal matrix composite (MMC) on AA6061 aluminum alloy. In the present study, such a composite layer is undesirable as it is highly diluted with the elements from the substrate (mostly Fe), which negatively influence the wear properties and hardness of the coating.

The formation of stable intermetallic compound(s) between the precursor and the substrate can also be detrimental to the coating strength because they are generally brittle in nature [13, 14]. Fe-Mo phase diagram indicates the formation of stable high temperature intermetallics like Fe_2Mo (λ), Fe_7Mo_6 (μ) and FeMo (σ) between Fe and Mo [15, 16]. Thus, LISI^{TM} deposition of molybdenum directly onto steel has two problems: (a) dilution caused by melting of low-melting-point steel substrate, and (b) formation of stable brittle intermetallics between Fe and Mo. One of the ways reported in literature to reduce the influence of intermetallics on coating performance is the use of a suitable

intermediate layer [17, 18]. We implemented an intermediate layer based on chromium, as suggested by Sears et al. [19]. Phase diagrams show the existence of continuous solid solution between Fe & Cr and Cr & Mo [15], which suggests chromium is a suitable intermediate layer for deposition of Mo on steel. Although there is a region of sigma phase (σ) formation in Fe-Cr system, the kinetics of its formation are very slow [20] and can be overlooked because of high cooling rates achieved during laser processing. Also, the melting point of chromium (~1857^{o}C) is between those of steel (~1435^{o}C) and molybdenum (~2610^{o}C), which helps in reducing the dilution of Mo coating.

In the present study, the chromium intermediate layer and the molybdenum final coating chemistries are based on their eutectic systems with boron (i.e. Cr-B and Mo-B eutectic systems). This helps in two ways: (i) by reducing the melting point of the alloy, and (ii) by increasing the hardness by solid solution strengthening. As a eutectic mixture melts at a temperature lower than its constituent elements, it further reduces dilution in the coating due to melting of the substrate. Cr-B eutectic (Cr-3.1wt.% B) melts at ~1630^{o}C and Mo-B eutectic (Mo-3wt.% B) melts at ~2180^{o}C [15]. CrB_2 and MoB have been used as sources of boron for the chromium layer and the molybdenum coating, respectively instead of elemental boron. We made use of Cr-CrB_2 eutectic composition to make the intermediate layer and Mo-MoB eutectic composition to make the main coating. To differentiate pure metals and eutectic mixtures, the compositions for chromium intermediate layer and molybdenum main coating are denoted as **Cr*** and **Mo***, respectively from this point onwards, where Cr* is Cr-10.5 wt % CrB_2 and Mo* is Mo-30 wt.% MoB. The coatings formed after laser processing are termed as Cr layer and Mo coating. Table 1 shows the densities and melting temperatures of materials used in the present study.

2. Experimental

Precursor mixture for Cr layer was made by mixing Cr and 10.5 wt.% CrB_2 powders (both manufactured by CERAC Inc.) of mesh size -325 (average 10 microns) with 30 wt.% i-8 LISI^{TM} binder (proprietary formulation by Warren Paint and Color Company, Nashville, TN). The Mo precursor was made by mixing Mo (EM-MM2; manufactured by Climax Engineering Materials) and 30 wt.% MoB (manufactured by CERAC Inc.) powders of mesh size -325 with 80 wt.% i-8 LISI^{TM} binder as shown in Table 2.

Laser processing was done in open atmosphere with a 1kW YLR-1000 (IPG Photonics Corporation) direct diode pumped fiber laser of 1075±5 nm wavelength. The laser beam was scanned along the surface of the processing area by galvanic scan mirrors (ScanLabs HurryScan30). For screening purposes, three process parameters were varied, laser power, scanning speed, track overlap (referred to as ***hatch*** from this point onwards) in order to obtain a continuous and homogenous coating. Hatch is the distance between the centerlines of laser beam of the two successive passes as shown in Figure 1 and can be correlated to the degree of overlapping of the subsequent laser melted tracks; linear

overlap can be calculated as 2r – h, where r is the laser beam radius and h is the hatch. The laser beam profile is shown in Figure 2 and the spot size was maintained nominally at 0.15 mm radius (~ $1/e^2$) for all the experiments. In order to minimize the heat affected zone in laser alloying experiments the cooling rate of the laser treated area must be quite high. Since the cooling is primarily by conduction the rate is kept high by reducing the size of the laser treated area and exposure time by moving a small spot at high velocity [21].

First, the precursor mixture for Cr layer (Cr*) was sprayed on AISI 4130 steel substrates of size 25mm x 50mm x 4mm with an air spray gun (Crescendo®, Model 175 by Badger Air-Brush Co., IL), and then dried under a heat lamp for several hours before laser processing. The chemical composition of AISI 4130 steel is given in Table 3. After laser processing Cr layer, the precursor mixture for Mo coating (Mo*) was sprayed on Cr coated AISI 4130 steel in a similar fashion. The direction for laser processing of Mo coating was perpendicular to Cr layer. Initial processing parameters used for screening purposes for both the coatings are shown in Table 4 and the optimized processing parameters for final coatings are shown in Table 5.

SEM analysis was done on an ISI Super IIIA Scanning Electron Microscope equipped with IXRF Energy Dispersive Spectrometer (version 1.3 RevP) to characterize the Cr layer and Mo coating. Transverse cross-section samples (perpendicular to the coating) of Cr layer and Mo coating were polished and etched with modified Murakami's reagent (1gm KOH + 3 gm $K_3Fe(CN)_6$ + 10ml water), respectively. Microindentation hardness testing was done on a LECO LM 300AT microhardness tester, integrated with LECO AMH32 software, under a load of 100 gf for 15 seconds using Vickers indenter. Microhardness measurements were taken across the coating thickness. X-ray diffraction studies were done on a Philips X'pert system with Cu Kα radiation (λ= 1.5406 Å) to identify the phases present in the Cr layer and Mo coating. Sliding wear tests were done on "as processed" samples using a block-on-ring wear testing apparatus. Wear rate was determined as volume loss with respect to time. Tests were conducted at 1000 revolutions per minute speed and 4 lb load in accordance with ASTM designation G77 [22]. Solid particle impingement erosion tests were done on "as processed" samples on a PLINT TE68 Gas Jet Erosion Rig, which complies with the ASTM G76 standard test method for conducting erosion tests by solid particle impingement using gas jets [23]. The tests were done at 90 degrees glancing angle with silica (50-70 μm) feed-rate of 2 grams/minute at a speed of 52 m/s on as processed samples. The distance between the jet and the substrate was 15 mm.

3. Results & Discussion

3.1 Optical/SEM/EDS analysis

The surface appearance macrophotographs of as processed Cr layer and Mo coating were taken under an optical microscope at 10X and are shown in Figures 3 and 4,

respectively. SEM micrograph of the transverse cross-section of Cr layer, taken at 300x (Figure 5), shows that the layer thickness is around 125-150 microns. It also shows the presence of a narrow heat affected zone (white cloudy region) which stretches about 100 microns underneath the Cr layer. The EDS analysis shows that the amount of Fe (dilution) in the Cr layer is around 10-20 wt.%. It was noticed that the Cr layers with Fe content less than 10 wt.% chipped off from some locations whereas those with Fe content more than 10 wt.% were very continuous and homogenous all through the coating. This indicates that the Cr layer requires a minimum of 10 wt.% Fe to keep the coating intact. A homogenous and continuous Cr layer is of paramount importance even if it contains 10-20 wt.% Fe dilution content because of the subsequent processing of Mo* on Cr coated steel.

While laser processing Mo coating on Cr coated steel, heat travels through the Mo* precursor layer and affects the Cr layer, the previous HAZ, and the steel substrate. Thus, the thickness and composition of Cr layer alter after processing Mo* on Cr coated steel. This affected Cr layer is termed as reprocessed-Cr layer from this point onwards. SEM micrograph (Figure 6) shows that the Mo coating is around 100-125 microns thick whereas the reprocessed-Cr layer underneath is 100-125 microns thick as well. Mo* precursor alloys with the Cr layer and forms the Mo coating. The microstructure of Cr layer is shown in Figure 7 and the microstructures of Mo coating and reprocessed-Cr layer are shown in Figures 8 and 9. EDS analysis showed that the Mo coating is a solid solution of Mo, Cr, Fe, and B, which contains 20-25 wt.% Cr and 6-8 wt.% Fe. The quantitative analysis of boron could not be done with the EDS because of relatively poor peak-to-background ratio of boron peak. Figure 10 is the EDS linescan of Mo coating and it shows the variation of Mo, Cr, and Fe with respect to the coating thickness. The Mo coating showed the presence of very few vertical cracks mostly originating from the middle of the Mo coating and running towards the surface as shown in Figure 11.

3.2 Microhardness

Microhardness test results show that the Cr layer (Figure 12) has hardness in the range 1050±50 $HV_{0.1}$. The hardness of Cr layer obtained in the present study is higher than that of the pure chromium coatings processed by other techniques (700-1000 HV) [24, 25] which is actually due to the presence of boron in the coating that was confirmed by the XRD analysis. Also, the steel laser alloyed with pure CrB_2 is reported to have the coating hardness around 1250 HV [26]. The hardness graph also shows the presence of a narrow heat affected zone (~100 μm) in the substrate whose hardness is around 400 $HV_{0.1}$ can be seen in the SEM micrograph as well (Figure 5).

The hardness of Mo coating is in the range 1100±50 $HV_{0.1}$ (Figure 13), which is more than that deposited by other techniques (729-982 VHN) [2, 4, 27-29]. This high hardness of Mo coating can be attributed to the fact that it is an alloy of Mo, Cr, Fe, and B, as explained earlier. The substrate does not have a marked heat affected zone and its hardness is around 250 $HV_{0.1}$ and it cannot be clearly seen in the SEM micrograph

(Figure 6). The drop in hardness of HAZ in the substrate from 400 $HV_{0.1}$ to 250 $HV_{0.1}$ is probably due to tempering induced by Mo* processing on Cr coated steel.

3.3 X-Ray Diffraction

X-ray diffractogram of Cr layer (Figure 14) shows the presence of Cr_2B, CrB, Fe-Cr solid solution and CrB_2 phases. During laser processing the Cr* mixture melts and undergoes a non-equilibrium eutectic solidification where some supersaturation in the chromium phase lead to the formation of chromium rich borides. The diffractogram shows the peaks of Fe-Cr solid solution which corroborates with the results obtained earlier [26, 30]. Shafirstien et al. studied the laser surface alloying of 1045 steel with CrB_2 [31] and reported the formation of Fe_3B, Cr_3C_2, retained austenite, and some martensite in the coating. In their work, the carbon content of the steel substrate was found to be responsible for the formation of chromium carbides because of the high affinity of chromium towards carbon. In contrast to the studies done on laser alloying of steel with CrB_2 [26, 30, 32], present study does not show the presence of iron borides and chromium carbides in X-ray analysis, which may be attributed to the very high content of Cr (89.5 wt.%) in the precursor mixture. The high hardness of Cr layer can thus be attributed to the presence of boride phases in the coating. Mo coating XRD analysis was done in the 2-theta range 30^o-110^o and is shown in Figure 15. The diffractogram shows the prominent peaks of molybdenum (2-theta degree values of 40.5^o, 58.6^o, 73.7^o, 87.6^o and 101.46^o) and a peak of Mo_2B (2-theta degree value of 70.6^o). The diffractogram does not show any peak of Cr or Fe or their borides, which indicates that they form a solid solution with Mo, which contains 20-25 wt.% Cr and 6-8 wt.% Fe according to the EDS analysis. This alloying did not result in any significant shift in the peaks of molybdenum.

3.4 Wear & Erosion

Cumulative volume loss was determined at intervals of 2 minutes for 20 minutes on two samples of each type, and then their average was plotted against time (Figure 16). As the coatings are solid solutions and not pure elements, the densities of the coatings were estimated by the rule of mixtures for the solid solutions. The results show that the wear performance of Mo coating is much better than that of the Cr layer and the base substrate, and the wear performance of Cr layer is also better than that of the steel substrate. The results also show that the Cr layer increases the wear resistance of the steel substrate by almost 3 times whereas the Mo coating increases it by almost 10 times.

Analogous to the wear rate, the erosion rate was also determined as cumulative volume loss with respect to time for 90 minutes, measured at 15 minutes interval on two samples of each type. Erosion graph in Figure 17 shows that the performance of Cr layer is much better than that of the Mo coating and the base substrate, whereas the performance of the base substrate is better than that of the Mo coating. Result shows that the chromium layer improves the erosion resistance of base substrate by a factor of 2.5, whereas the erosion resistance of base substrate is better than that of the molybdenum coating by a factor of 4. Even though the Mo coating improves the sliding wear resistance

of the steel substrate by a factor of 10 due to its self-lubricating behavior and high hardness, it deteriorates the erosion resistance by a factor of 4. In fact, in dirty and abrasive environments, molybdenum coatings are reported to wear appreciably faster than chromium plating [33, 34]. Shivpuri et al. [35] also reported a higher mass loss of molybdenum coating than the substrate H13 steel in erosive wear tests though the reason for this behavior was not explained. The various factors reported in literature that may influence the erosion resistance of a coating are its surface roughness, microstructure, morphology, hardness, presence of cracks, and porosity. Higher volume loss of molybdenum coating in the present study (approximately 2.65 mm^3 at the end of 90 minutes) despite its high hardness indicates that there is a weak correlation between erosion behavior and coating hardness, which corroborates with the studies done earlier by Lathabai et al. on metallic coatings [36].

4. Conclusions

1) Molybdenum coating has been deposited on steel using chromium as the intermediate layer and LISI^{TM} as the coating process. Both the coatings, chromium layer and molybdenum coating were continuous in nature and their thicknesses were 125-150 microns and 100-125 microns, respectively.

2) The optimized laser processing parameters for chromium coating were found to be laser power 155-165 W, scanning speed 25-30 mm/s, and hatch 0.1-0.15 mm for 200-225 microns precursor thickness whereas that for molybdenum coating were found to be laser power 175-185 W, scanning speed 22-25 mm/s, and hatch 0.1 mm for 125-150 microns precursor thickness. Both the coatings were processed at 0.15 mm radius laser beam spot size.

3) A minimum of 10 wt.% Fe is required in the chromium layer for good metallurgical bond. Molybdenum coating was found to be an alloy of molybdenum, 20-25 wt.% chromium, 6-8 wt.% iron and boron. SEM/EDS analysis did not show the presence of any intermetallic phases in both the intermediate and main coatings.

4) The hardness of chromium layer was in the range 1050±50 VHN, whereas that for molybdenum coating was in the range 1100±50 VHN. The high hardness of chromium layer was due to the presence of boride phases, whereas that for molybdenum coating was due to its solid-solution strengthening with chromium, iron and boron.

5) Chromium layer improved both the sliding-wear resistance and erosion resistance of the steel substrate by 2.5 and 3 times, respectively. Molybdenum main coating improved the sliding-wear resistance of the steel substrate by almost 10 times but deteriorated the erosion resistance by 4 times. In the case of molybdenum coating, it was found that there is a weak correlation between the coating hardness and erosion behavior.

5. Acknowledgements

The authors gratefully acknowledge the financial support given by the Tennessee Higher Education Commission to the Center for Laser Applications, University of Tennessee Space Institute, Tullahoma. The authors also extend their gratitude towards the summer intern Ms. Larissa Wenren for her help in conducting various laboratory tests.

6. References

[1] B.J. Taylor, T.S. Eyre, Tribology International 12 (1979) 79-89.
[2] G. Jin, B. Xu, H. Wang, Q. Li, S. Wei, Surface & Coatings Technology 201 (2007) 6678-6680.
[3] J.A. Horwath, Thin Solid Films 73 (1980) 79.
[4] J. Khedkar, A.S. Khanna, K.M. Gupt, Wear 205 (1997) 220-227.
[5] S. Sampath, S.F. Wayne, Journal of Thermal Spray Technology 3 (3) (1994) 282-288.
[6] S.F. Wayne, S. Sampath, V. Anand, Tribology Transactions 37 (3) (1994) 636-640.
[7] J.J. Liao, R.C. Wilcox, R.H. Zee, Scripta Metallurgica et Materialia 24 (1990) 1647-1652.
[8] R.W. Burwan, Journal of Metals 29 (11) (1977) 12-17.
[9] S. Sampath, V. Anand, S.F. Wayne. *On the Properties of Mo-based Thermal Spray Coatings at Temperatures Up to 300°C* in *2nd Plasma Technik Symposium.* 1991. Lucerne, Switzerland.
[10] G.Q. Toshio Nakamura, and Christopher C. Berndt, Journal of American Ceramic Society 83 (3) (2000) 578-584.
[11] Z. Wang, A. Kulkarni, S. Deshpande, T. Nakamura, H. Herman, Acta Materialia 51 (2003) 5319-5334.
[12] P.H. Chong, H.C. Man, T.M. Yue, Surface & Coatings Technology 154 (2002) 268-275.
[13] A.E. Martinelli, R.A.L. Drew, Journal of the European Ceramic Society 19 (12) (1999) 2173-2181.
[14] R. Borrisutthekul, T. Yachi, Y. Miyashita, Y. Mutohc, Materials Science and Engineering A 467 (2007) 108-113.
[15] *Alloy Phase Diagrams*. ASM Handbook. Vol. 3: ASM International.
[16] V. Raghavan, Journal of Phase Equilibria 23 (6) (2002) 515-516.
[17] B.V. Krishna, P. Venugopal, K.P. Rao, Science and Technology of Welding and Joining 10 (3) (2005) 259-267.
[18] S. Kundu, S. Chatterjee, D. Olson, B. Mishra, Metallurgical & Materials Transactions A 38A (2007) 2053-2060.
[19] A.C. James W. Sears, Sudip Bhattacharya, Jerrod Roalstad and Stanley M Howard. *Improving the high temperature wear characteristics of industrial tools and dies using functionally graded refractory metals*. in *International Conference on Tungsten, Refractory & Hardmetals VI*. 2006. Orlando, FL.
[20] X. Tang, Microsc. Microanal. 11 (Suppl 2) (2005) 78-79.

[21] William Hofmeister, et al. *Solidification in Direct Metal Deposition by LENS Processing*. Journal of Metals, September 2001.
[22] G77, *Annual Book of ASTM Standards*. Wear and Erosion; Metal Corrosion. Vol. 03.02. 1996: ASTM International. 303-314.
[23] *Annual Book of ASTM Standards*. Metals Test Methods and Analytical Procedures: Wear and Erosion; Metal Corrosion. Vol. 03.02. 2002: ASTM International.
[24] Y. Zhang, Q. Chen, Z. Wang, G. Zhang, Y. Ge, Surface & Coatings Technology 201 (2007) 5190-5193.
[25] Z. Zheng, L. Wang, L. Chen, J. Zhang, Surface & Coatings Technology 201 (2006) 2282-2288.
[26] P. Schaaf, V. Biehl, U. Gonser, M. Bamberger, M. Langohr, F. Maisenhalder, Hyperfine Interactions 57 (1990) 2095-2100.
[27] G. Akdogana, T.A. Stolarski, S. Tobe, Wear 253 (2002) 319-330.
[28] S.C. Modi, E. Calla, Journal of Thermal Spray Technology 10 (3) (2001) 480-486.
[29] T.A. Stolarski, S. Tobe, Wear 249 (2001) 1096-1102.
[30] B. Medres, L. Shepeleva, G. Ryk, G. Dehm, M. Bamberger, W.D. Kaplan. *The Peculiarities of Steels Laser Treatment with CrB2 and Ni2B Powders*. in *ICALEO* 1998. Orlando: Laser Institute of America.
[31] G. Shafirstien, M. Bamberger, M. Langohr, F. Maisenhalder, Surface & Coatings Technology 45 (1991) 417-423.
[32] L. Bourithis, G. Papadimitriou, Materials Letters 57 (2003) 1835-1839.
[33] J. AR, Transactions of the Institute of Metal Finishing 70 (1) (1992) 8-13.
[34] Z. Liu, M. Hua, Tribology International 32 (1999) 499-506.
[35] R. Shivpuri, Y.L. Chu, K. Venkatesan, J.R. Conrad, K. Sridharan, M. Shamim, R.P. Fetherston, Wear 192 (1996) 49-55.
[36] S. Lathabai, M. Ottmuller, I. Fernandez, Wear 221 (1998) 93-108.

7. Figure Captions

Figure 1 - The “hatch” is defined as the distance between the centerlines of laser beam in subsequent passes as shown in this sketch. The “overlap” is a function of hatch and beam size.
Figure 2 - Beam intensity profile of the fiber laser taken at 175W. The beam radius is measured at 13.5% of peak intensity as 0.15 mm as shown in this figure.
Figure 3 - Optical macrograph of Cr coating showing its surface appearance.
Figure 4 - Optical macrograph of Mo coating showing its surface appearance.
Figure 5 - SEM micrograph of Cr coating.
Figure 6 - SEM micrograph of Mo coating.
Figure 7 - SEM micrograph showing the microstructure of Cr coating.
Figure 8 - SEM micrograph showing the microstructure of Mo coating.
Figure 9 - SEM micrograph showing the microstructure of reprocessed-Cr layer.
Figure 10 - EDS linescan of Mo coating showing variation of Mo, Cr and Fe in the top 175 microns. Note that the intensity is not normalized.
Figure 11 - SEM micrograph showing cracks in Mo coating.

Figure 12 - Hardness variation across the thickness for Cr coating.
Figure 13 - Hardness variation across the thickness for Mo coating.
Figure 14 - XRD diffractogram of Cr coating showing the presence of various chromium borides and Fe-Cr solid solution.
Figure 15 - XRD diffractogram of Mo coating showing the presence of Mo and Mo_2B.
Figure 16 - Sliding wear volume loss of Mo, Cr coatings and 4130 steel with respect to time for first 20 minutes showing their wear resistance.
Figure 17 - Erosion volume loss of Mo, Cr coatings and 4130 steel with respect to time for first 90 minutes showing their erosion resistance.

8. Tables

Table 1
Physical properties of materials used in the experiments.

Material	Density (g/cc)	Melting point (^oC)
Cr	7.2	1857
CrB_2	5.15	~2200
Mo	10.2	2610
MoB	8.65	2180
AISI 4130 steel	7.8	~1435

Table 2
Precursor mixture composition for Cr layer and Mo coating.

Cr*	=	89.5 grams Cr + 10.5 grams CrB_2 + 30 grams i-8 LISI^{TM} binder
Mo*	=	70.0 grams Mo + 30.0 grams MoB + 80 grams i-8 LISI^{TM} binder

Table 3
Chemical composition of AISI 4130 steel (weight %).

C	Mn	Cr	Si	Mo	P	S	Fe
0.3	0.85	0.83	0.18	0.24	<0.035	<0.04	Balance

Table 4
Screening parameters used initially for laser processing of Cr layer and Mo coating.

Coating	Precursor thickness (μm)	Laser Power (W)	Hatch (mm)	Scanning Speed (mm/s)
Cr*	200 – 225	150 – 220	0.1 – 0.25	20 – 30
Mo*	125 – 150	150 – 250	0.1 – 0.25	15 – 30

Table 5
Optimized parameters found for laser processing of Cr layer and Mo coating.

Coating	Precursor thickness (μm)	Laser Power (W)	Hatch (mm)	Scanning Speed (mm/s)	Coating thickness (μm)
Cr*	200 – 225	155 – 165	0.1 – 0.15	25 – 30	125 – 150
Mo*	125 – 150	175 – 185	0.1	22 – 25	100 – 125

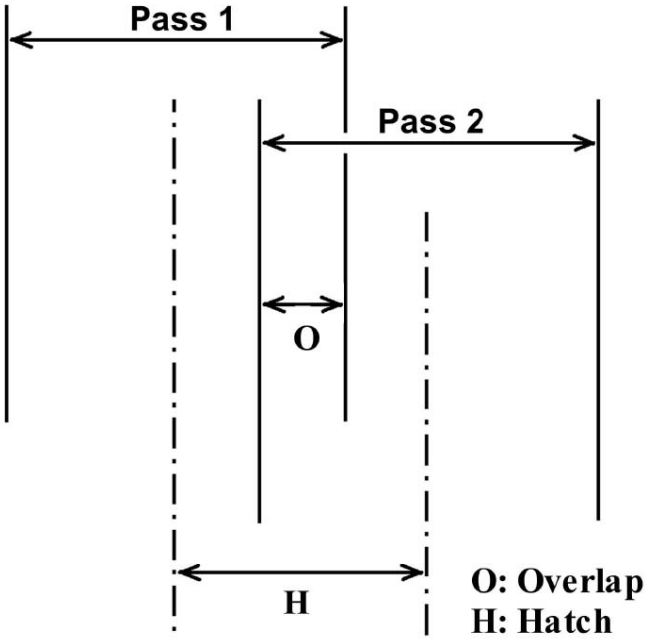

Figure 1

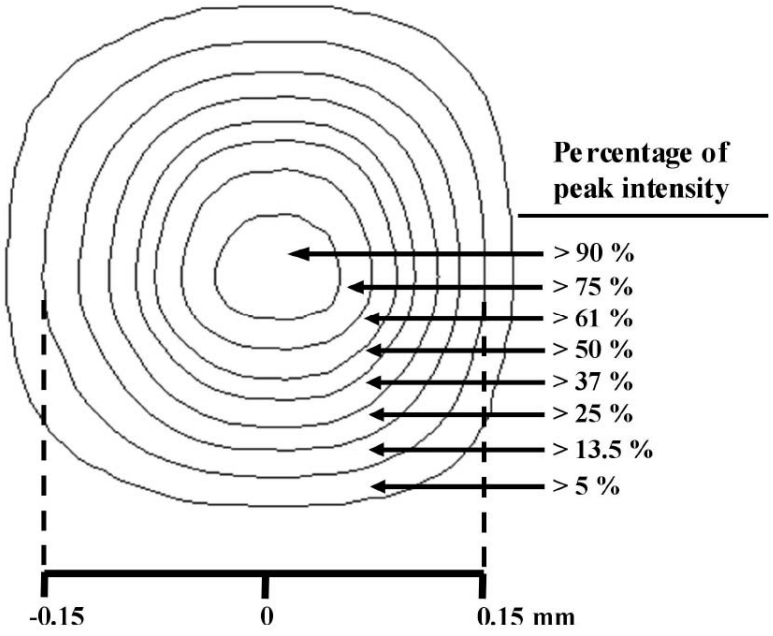

Figure 2

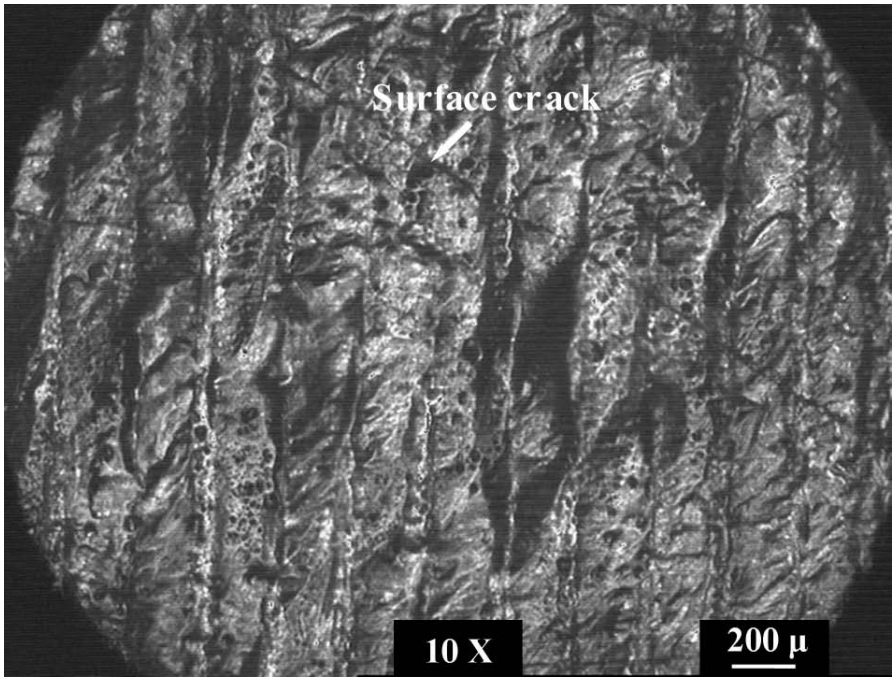

Figure 3

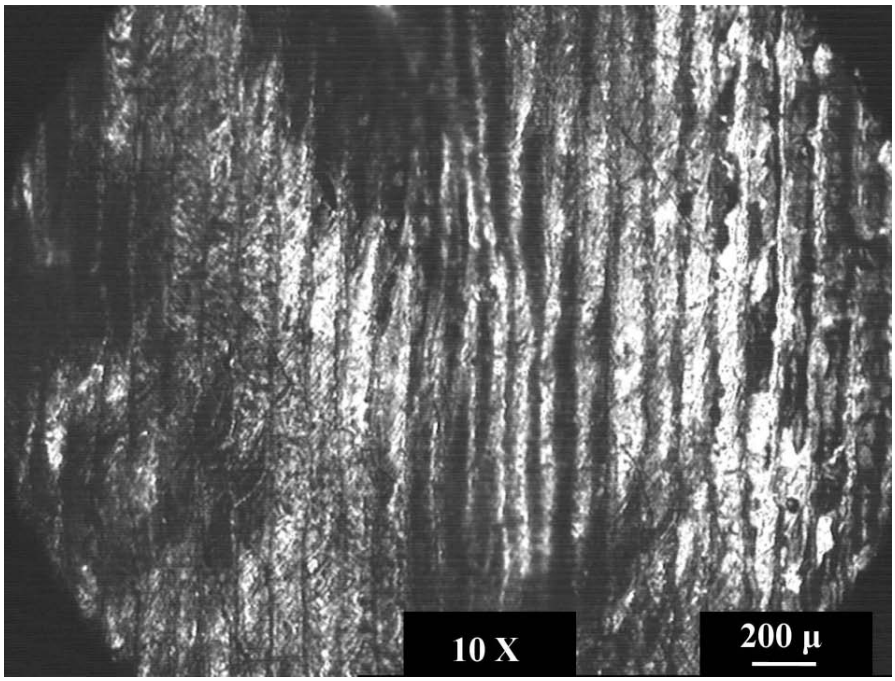

Figure 4

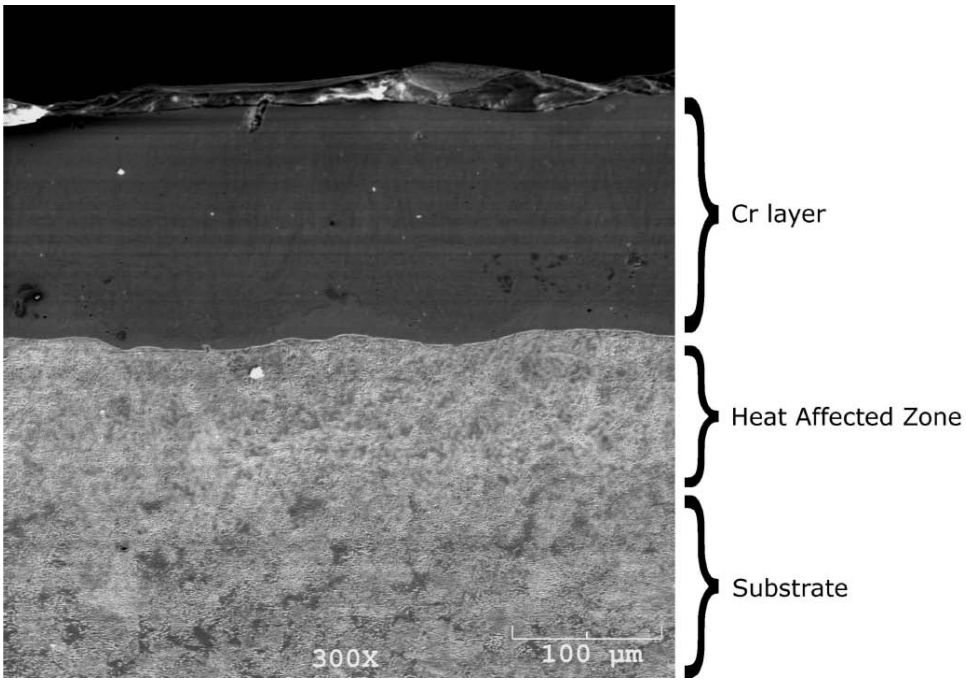

Figure 5

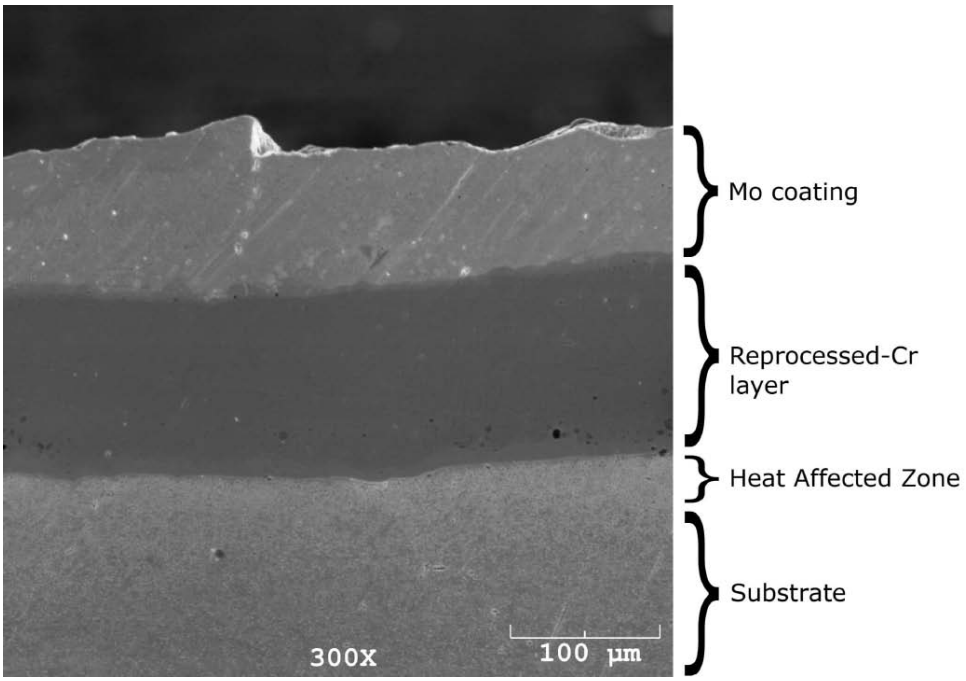

Figure 6

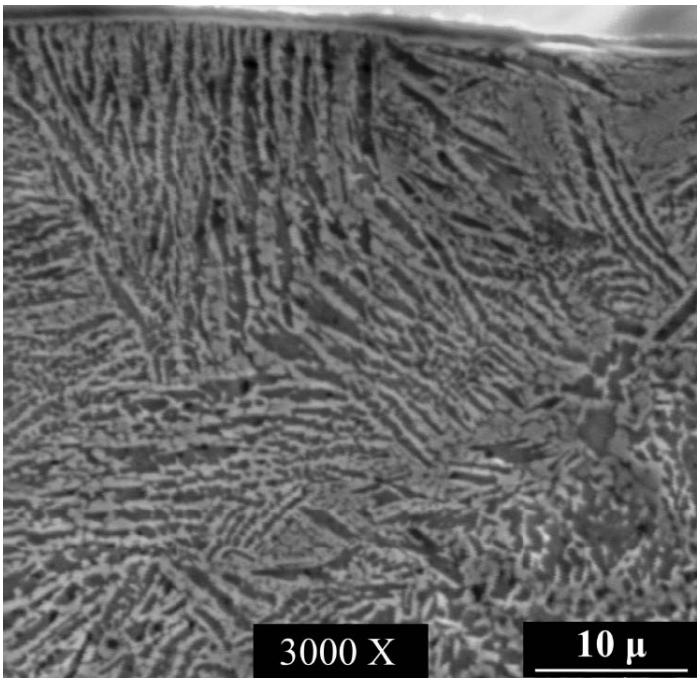

Figure 7

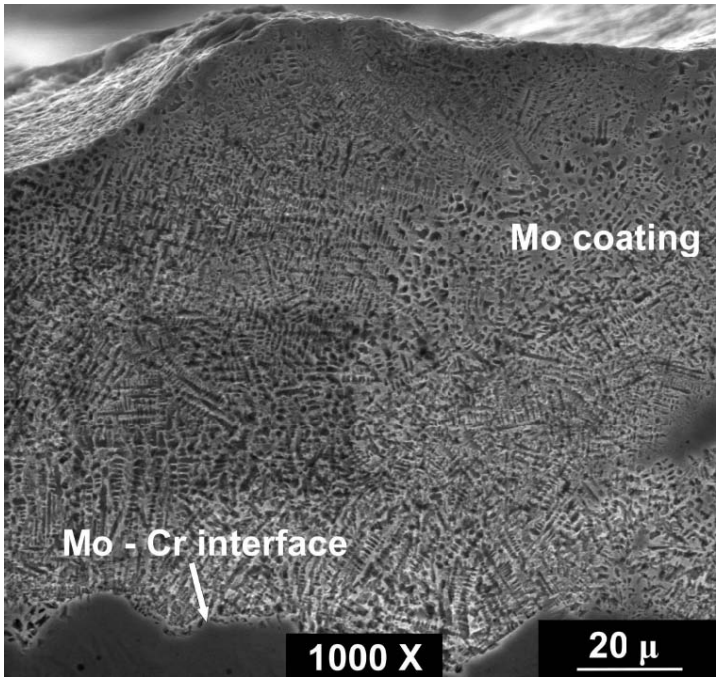

Figure 8

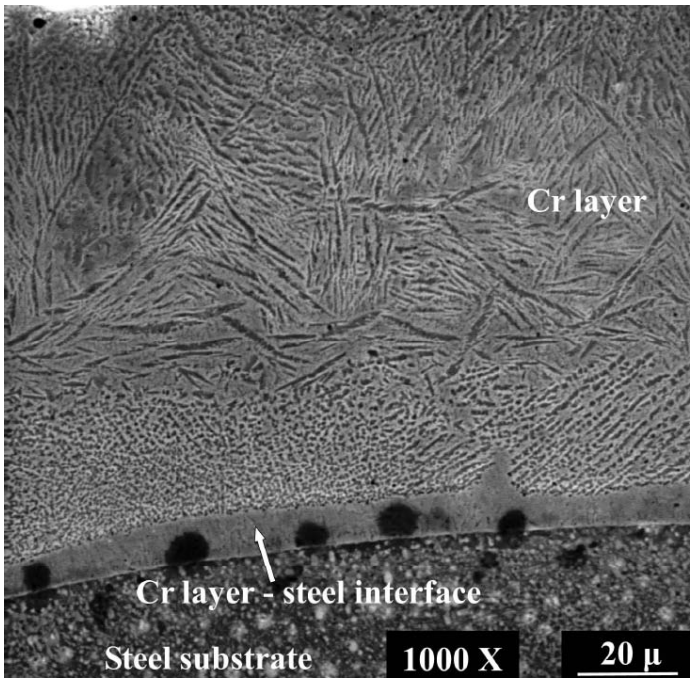

Figure 9

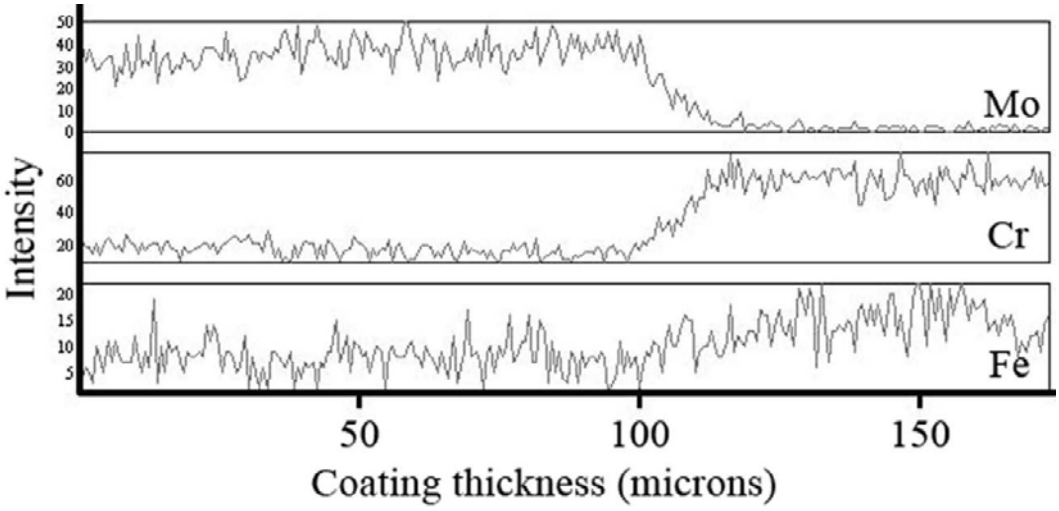

Figure 10

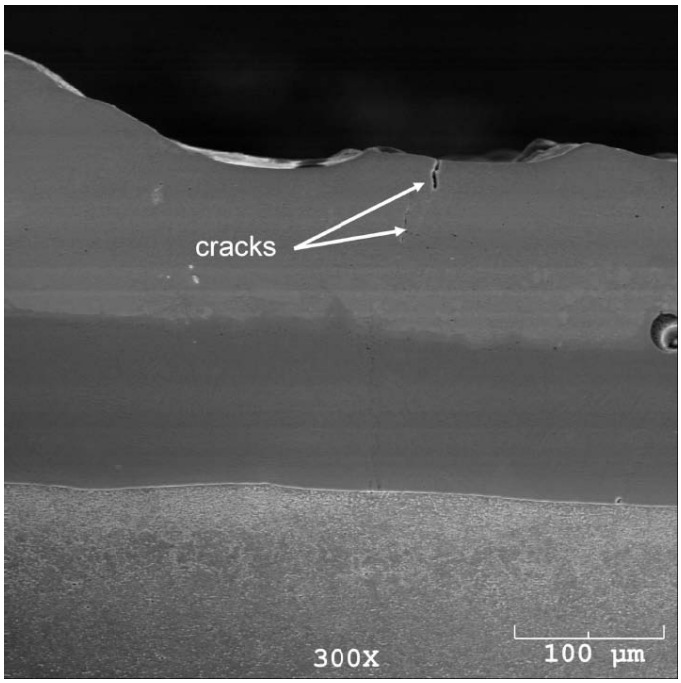

Figure 11

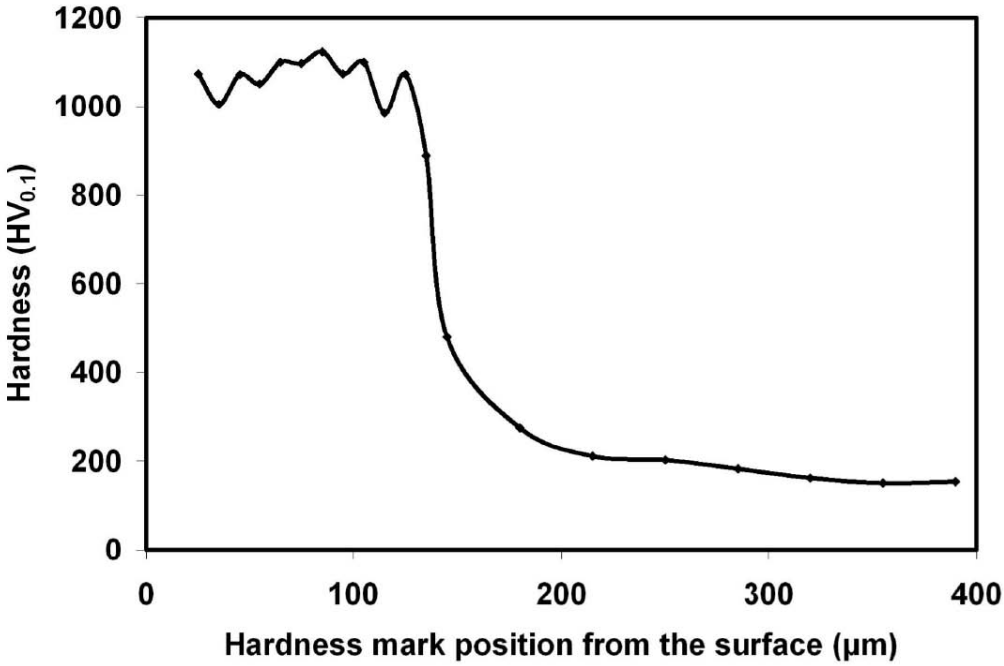

Figure 12

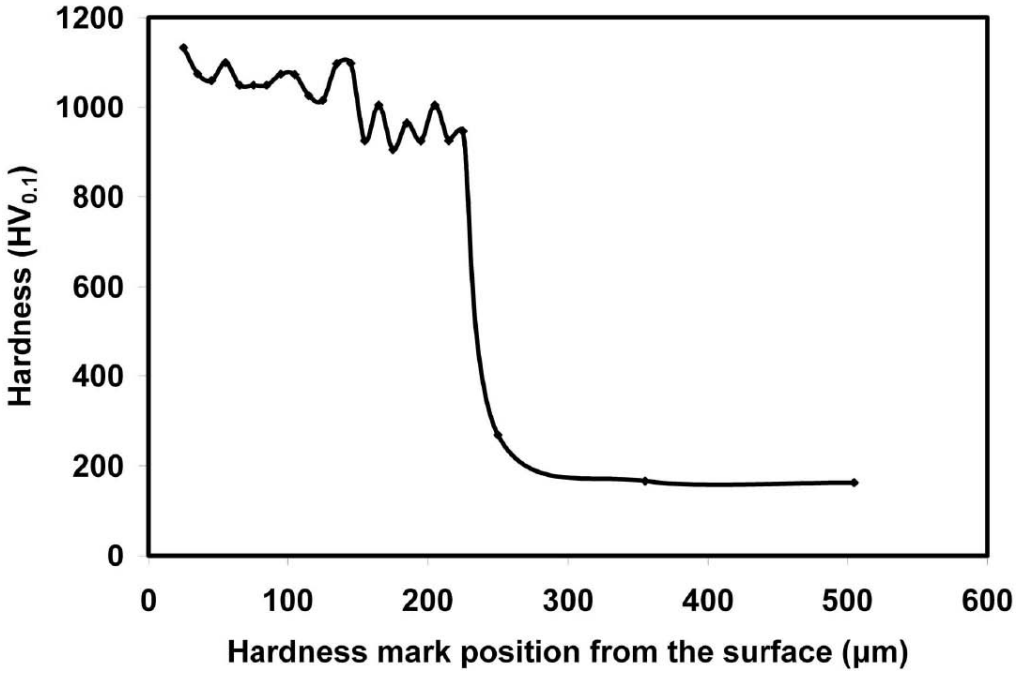

Figure 13

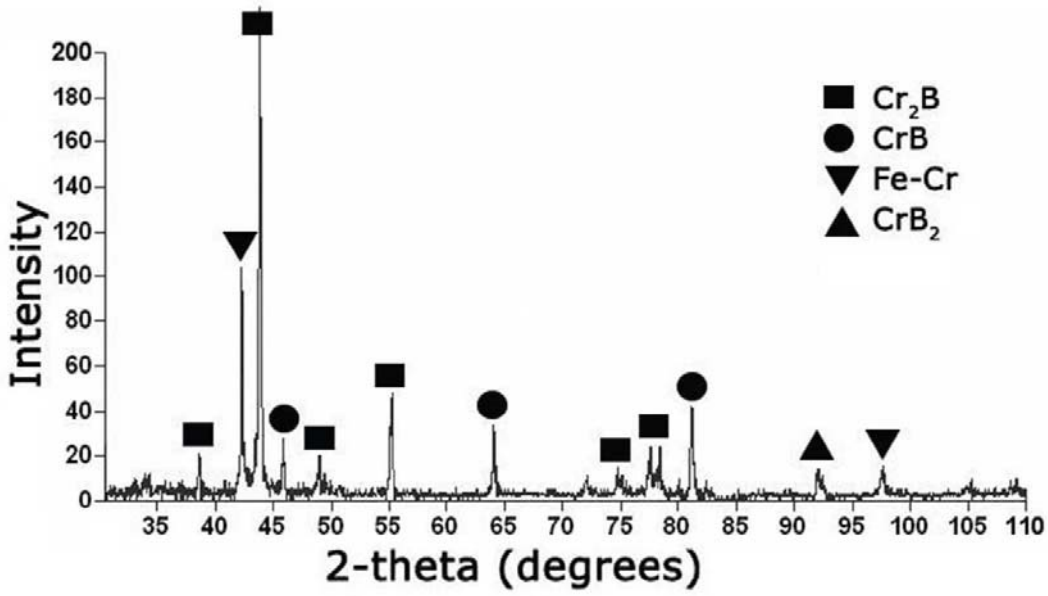

Figure 14

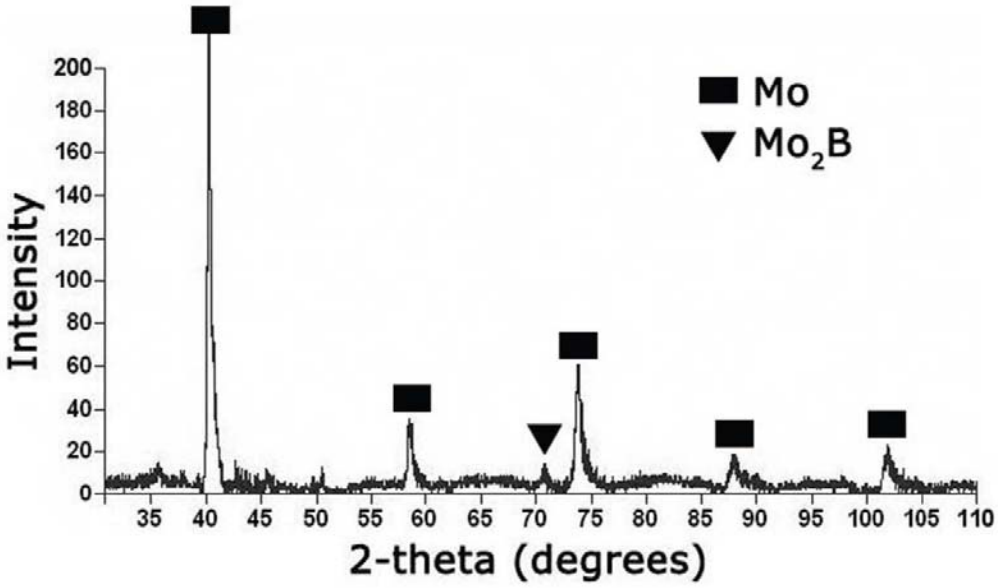

Figure 15

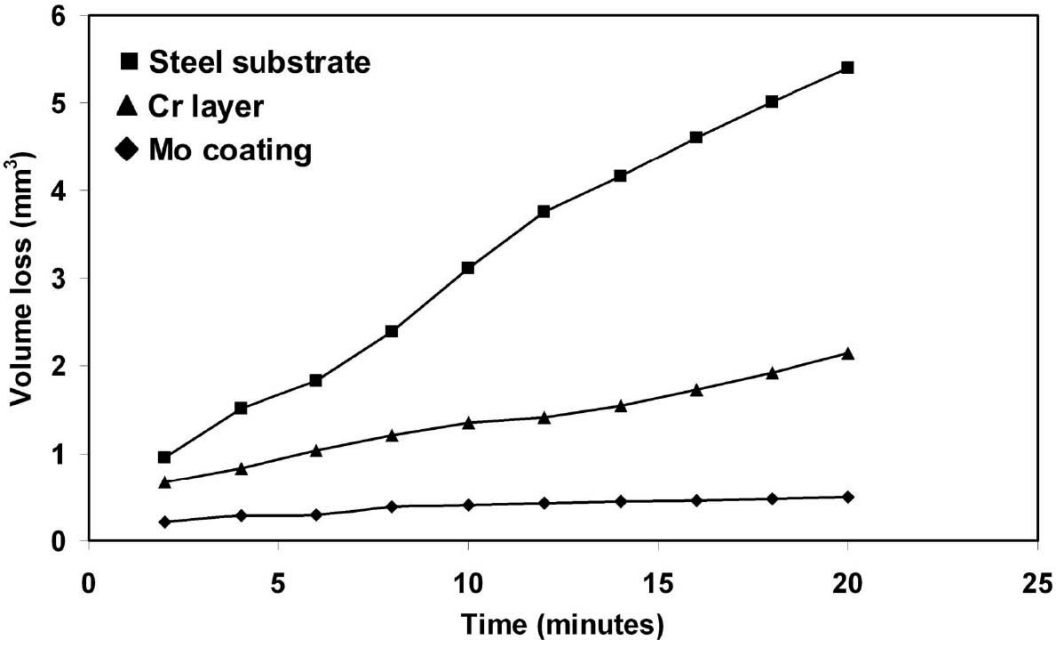

Figure 16

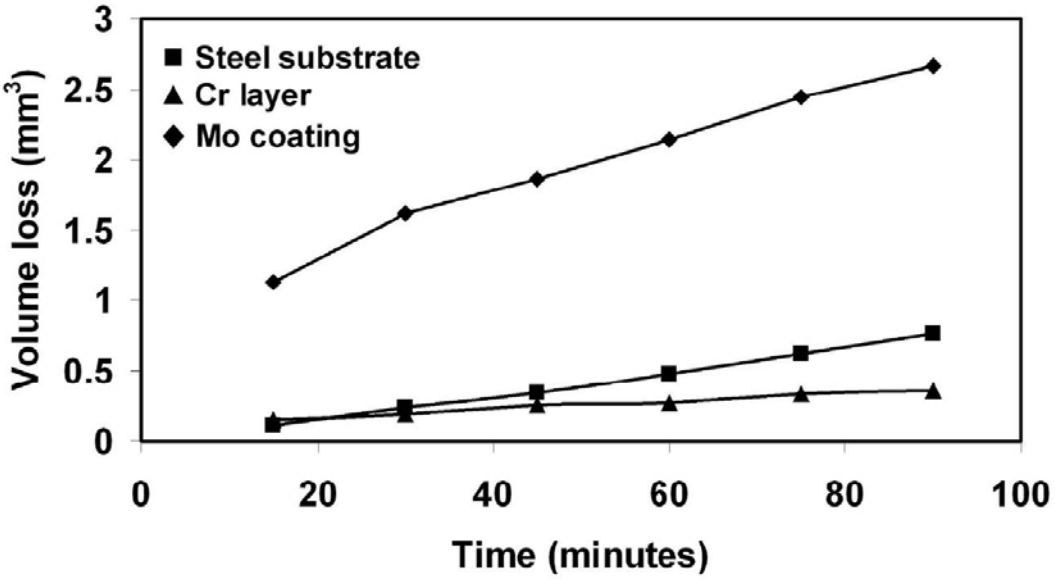
Steel substrate
Cr layer
Mo coating
Volume loss (mm3)
Time (minutes)
0
0.5
1
1.5
2
2.5
3
0
20
40
60
80
100

Figure 17

VITA

Deepak Rajput was born January 03rd 1982 in Bhilai, Chhattisgarh, India. He received his B.Tech. (Bachelor of Technology) degree in Metallurgical Engineering from the National Institute of Technology (erstwhile Regional Engineering College) at Tiruchirappalli, Tamil Nadu, India, in May 2004. He worked in the Research & Development Center of Essar Steel Limited, Hazira, India, as a research engineer from June 2004 to August 2006. He was in charge of the Materials Characterization Laboratory at Essar Steel Limited. He also worked on new products development in hot rolling, galvanizing, and cold rolled closed annealing sectors of steel. He joined the University of Tennessee Space Institute in Fall 2006 to pursue his master's in Materials Science & Engineering. He worked as a graduate research assistant to Dr. William Hofmeister at the Center for Laser Applications, UTSI.

Deepak Rajput has published three conference papers and five journal articles. He is a student member of the Materials Research Society (MRS) and Materials Advantage (AIST, ACerS, TMS, ASM International). He is a member of the Sigma Xi Honor Society affiliated to the Vanderbilt University chapter.